Upconversion Processes in Er^{3+}-doped K_2YF_5 crystals

A THESIS
SUBMITTED IN PARTIAL FULFILMENT
OF THE REQUIREMENTS FOR THE DEGREE
OF
MASTER OF SCIENCE IN PHYSICS
IN THE
UNIVERSITY OF CANTERBURY

BY

TIMOTHY DEAN

University of Canterbury

1998

Abstract

Visible upconversion fluorescence has been observed for laser excitation into the $^4I_{11/2}$, $^4I_{9/2}$ and $^4F_{9/2}$ multiplets of Er^{3+} ions in K_2YF_5 crystals. The predominant emission was from the $^4S_{3/2}$ multiplet of Er^{3+} . For excitation into each multiplet the mechanism responsible for the visible upconversion emission has been shown to be two-step Sequential Absorption Upconversion (SAU). Significant blue and ultra-violet upconverted emission was also observed in each case. Various energy-transfer mechanisms are proposed to explain these higher energy emissions, which are thought to be subsequent to the initial SAU process.

Optical absorption spectroscopy was performed in the region 1μm- 330nm on K_2YF_5:Er^{3+}. Absorption features were unambiguously assigned for transitions to the $^4I_{11/2}$, $^4I_{9/2}$, $^4F_9/2$, $^4S_{3/2}$, $^2H_{11/2}$, $^4F_{7/2}$, $^4F_{5/2}$, $^2H_{9/2}$, $^4G_{11/2}$, and $^2K_{15/2}$ multiplets of the Er^{3+} ion. The assignments for the $^4I_{11/2}$ to $^4F_{7/2}$ multiplets confirmed the results of previous workers.

Laser Selective Excitation (LSE) techniques have revealed evidence of a second crystal-field centre. The electronic transition energies of this centre differ only slightly from the primary centre indicating it represents a slight perturbation of the environment surrounding the Er^{3+} ion, perhaps due to clustering.

Various dynamical effects resulting from excitation into the $^4I_{11/2}$ multiplet have also been observed. After inital excitation, fluorescence from the sample is seen to sharply rise, then slowly (τ ~0.6s) attenuate to a steady level. A simultaneous reduction in both laser beam transmittance and ground-state population have also been observed.

A trigonal C_{3V} symmetry Hamiltonian was fitted to the experimental crystal-field energy levels from the optical spectroscopy work. The standard deviation of the fitted energy-level scheme (with respect to those experimentally observed) improved significantly on previous work.

Acknowledgements

I would like to thank my supervisor Dr. Roger J. Reeves for his encouragement and guidance throughout this project, and for the occasional complete re-alignment of the titanium-sapphire laser. Thanks also for the advice and experience provided by my fellow research student Steven Jamison.

Thanks to Professor N. Khaidukov, of the Institute of General and Inorganic Chemistry, Moscow, for providing the $K_2YF_5:Er^{3+}$ crystals used in this thesis.

This research was made considerably easier with the help of department's excellent technical staff. Ross Ritchie and Geoff Graham helped countless times with all aspects of the laboratory systems. Ron Culley and Wayne Smith in the workshop helped with the design and implementation of various new items of equipment. Liquid nitrogen for the FTIR cold-trap and various photomultipliers was created in the cryogenics workshop by Tom Walker and Bob Flygenring. Software used in crystal-field fitting section was provided by Dr. Mike Reid.

This work was partially supported by a B. G. Wybourne M.Sc. scholarship. This department also provided several opportunities for teaching employment in various tutoring and lab demonstrating positions.

Finally, thanks to Kerry and my family for supporting me in many ways through my studies.

Contents

Figures

Tables

Chapter 1

Introduction

This thesis presents the results of the study of upconversion processes in $K_2YF_5:Er^{3+}$ by optical and laser spectroscopy methods. This chapter is designed to familiarise the reader with the subject of this thesis, the material $K_2YF_5:Er^{3+}$. A summary of work done by previous workers on this system, and the motivation for this study are also considered.

1.1 Rare-earth ions and their properties

Two groups of elements, the lanthanides and the actinides, make up the group known as the rare-earth elements. A neutral atom of the lanthanide series consists of a xenon structure, $1s^2\ 2s^2\ 2p^6\ 3s^2\ 3p^6\ 3d^{10}\ 4s^2\ 4p^6\ 4d^{10}\ 5s^2\ 5p^6$, the partially filled $4f^N$ shell, and two or three electrons in the outer $6s^2$ or $5d6s^2$ shells. In their trivalent ionization state the lanthanide ions lose their outer 5d6s electrons leaving the xenon core and partially filled $4f^N$ shell, where N rises from 1 (cerium III) to 13 (ytterbium III) through the series. The spatial extent of the eigenfunctions of the 4f-electrons, however, is well within the $5s^2\ 5p^6$ closed shells of the xenon core. This effect is known as the *lanthanide contraction.*

The shielding of the 4f-electrons by the $5s^2\ 5p^6$ shell results in a reduced effect of the local environment on the energy levels of the $4f^N$ states of the rare-earth ions. The sharp transition lines and long excited-state lifetimes that characterise many rare-earth ion spectra, are a direct result of the reduced crystal field interaction between the lanthanide ions and the surrounding ions.

The rare-earth ions have considerable use in the fabrication of phosphors, due to their well-defined electronic energy-level structure, and hence chromatic properties. Another current use for these elements is in the production of solid-state laser sources. Lasers utilising such compounds as $YAG:Nd^{3+}$ have already found considerable industrial application. Most of the lanthanide series of elements have been shown to exhibit lasing action in various hosts.

Recently, cheap infrared and red wavelength semiconductor laser sources have become

widely available. These sources have widespread application in data storage and telecommunications. There is much interest, however, in developing a similar diode source functioning in blue wavelengths. Upconversion processes in rare-earth activated compounds could provide a means of achieving this. Upconversion is a mechanism whereby a high wavelength excitation produces low wavelength emission (for a more detailed description see the beginning of Chapter 5). Upconversion is commonly found in the ions of the lanthanide series, where long-lived 'metastable' states allow processes such as excited-state absorption.

The erbium ion Er^{3+} , with configuration $4f^{11}$, has an electronic energy level-structure as shown in Figure 1.1 [1]. Several important lasing channels have already been discovered for this ion. For the telecommunications industry, the $^4I_{13/2} \rightarrow ^4I_{15/2}$ lasing transition (1.5μm) holds considerable importance by operating in the important 1.55μm window for low signal attenuation ('quiet') signal transmission in optical fibers. Other well known lasing channels include $^4S_{3/2} \rightarrow ^4I_{15/2}$ (540nm), $^4F_{9/2} \rightarrow ^4I_{15/2}$ (650nm), and $^4I_{11/2} \rightarrow ^4I_{13/2}$ (2.8μm), which has application in laser surgery techniques.

1.2 The K_2YF_5 crystal host

The crystal K_2YF_5 is an optical material that, although first studied in structure in the 1980's, has only recently been examined in the optical regime. This resurgence is partly due to the ongoing program of searching for new and better laser and optical materials, and partly due to the availability of high-powered tunable laser sources. These sources have allowed the development of powerful selective excitation techniques. Obviously the two factors above, are somewhat circular.

The original X-ray diffraction studies [2] have shown this material to have a linear chain structure, with orthorhombic symmetry $D_{2h}{}^{16}$. Figure 1.2 shows a representation of this structure. In these 'chains', fluorine ions (F^-) form yttrium-fluorine radicals $[YF_5]^{2-}$, the fluorine ions arranged cage-like about the yttrium ion. Two of these yttrium-fluorine radicals share two fluorine ions along an edge to link in an infinite chain along the c-axis. The remaining potassium ions separate the individual chains in a hexagonal near-complete close packing arrangement.

The rare-earth ion Er^{3+} is of a very similar ionic radius to the host Y^{3+} ions. Further, it has been demonstrated that the doping process does not significantly affect the lattice constants of the crystal [3]. The rare-earth ion, therefore, replaces a yttrium ion in the host with little significant distortion to the lattice. As both Y^{3+} and Er^{3+} have identical

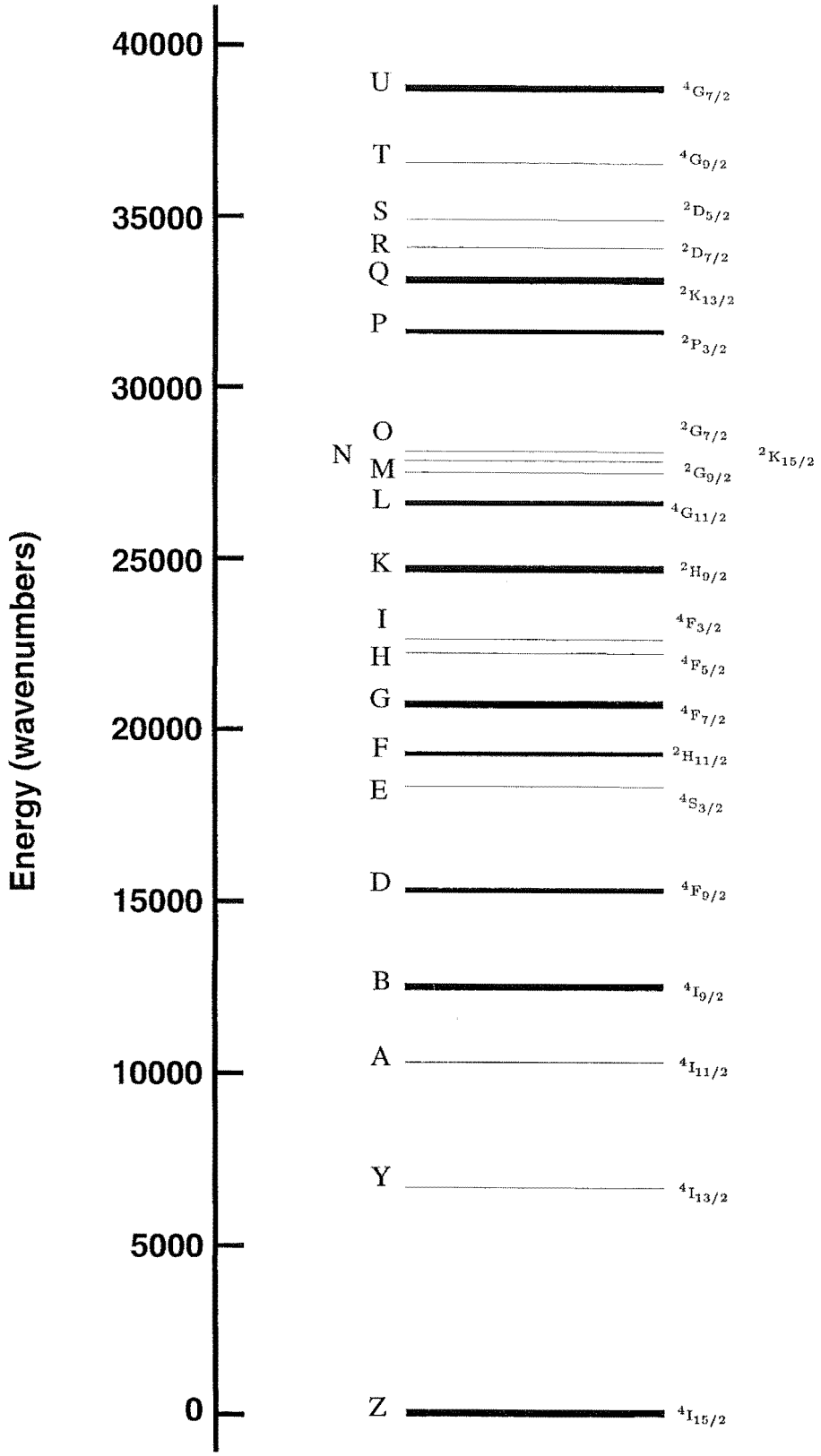

Figure 1.1: Approximate crystal-field energy levels for the Er^{3+} ion [1]. Multiplets are labelled by both the formal (LSJ) notation, and the spectroscopic labels (Z,Y,..) The thickness of a multiplet is an indicator of the spread of the individual crystal-field levels.

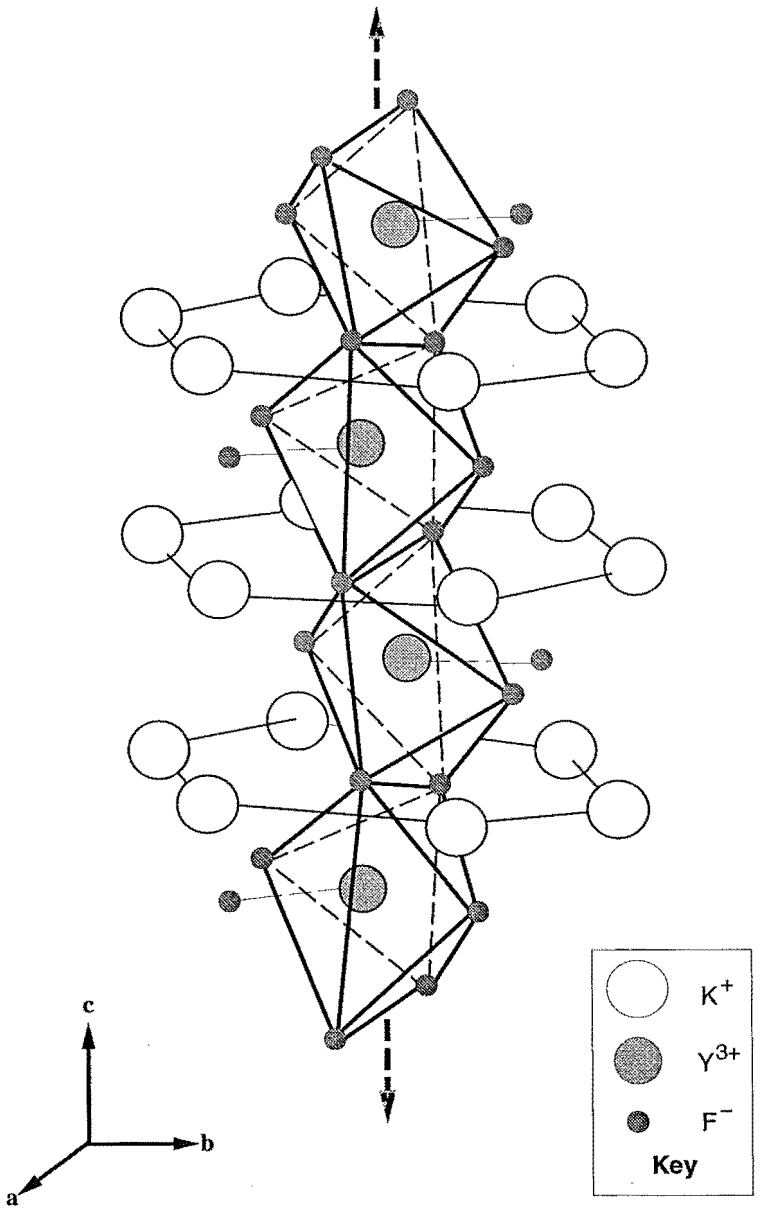

Figure 1.2: Crystal structure of K_2YF_5 showing the chain structure formed by the yttrium-fluorine $[YF_5]^{2-}$ complexes [2].

charge, compensation (as in the case for rare-earth dopants into alkaline-earth fluorides) is not required. Results for K_2GdF_5 [4] have shown the shortest distance between doping sites to be ~3.7Å. This result should be equally applicable to the K_2YF_5:Er^{3+} system, as the ionic radius difference between the two rare-earth ions is only 0.06Å[5].

The smallest inter-chain distance is larger at ~5Å. Thus, energy-transfer processes would be expected to be dominantly intra-chain effects. One-dimensional energy transfer has already been demonstrated for this material with Gd^{3+} and Tb^{3+} dopants [4, 6].

1.3 Previous work

Kharitanov *et al* [2] have grown samples of K_2YF_5 by the method of hydrothermal crystallisation. A structural investigation was performed on these samples using X-ray diffraction techniques. This study yielded the information on the structure of K_2YF_5 presented previously in Section 1.2.

Similar work had been done by Bochkova *et al* [7] on the samarium salt K_2SmF_5, some 9 years earlier. In that study, the X-ray diffraction results gave precisely the same crystal structure as has been stated for K_2YF_5 .

Peale *et al* [3] have provided results of a general spectroscopy study of highly- and fully- doped K_2YF_5:Er^{3+} . The purpose of that study was to investigate the potential of the K_2YF_5:Er^{3+} system as a possible laser material. Using Fourier-Transform Infra-Red absorption spectroscopy (FTIR), and laser fluorescence systems, a crystal-field energy-level scheme for the multiplets $^4I_{15/2}$ to $^4F_{7/2}$ was derived. These workers also carried out a crystal-field fit to their data using a trigonal symmetry Hamiltonian to their data. The assumption of a near trigonal C_{3V} symmetry for the rare-earth site was based on X-ray diffraction results of the previous works of Kharitanov, and Bochkova. The results of this fit were inconclusive at confirming this site symmetry for the rare-earth ionsite, as the standard deviation from experimental values was quite large at 25cm^{-1} . One reason proposed to explain this was that differences exist in the structures of the material grown by different methods.

A method of time-resolved FTIR spectroscopy yielded fluorescence lifetime measurements for the $^4I_{13/2}$,$^4I_{11/2}$,$^4F_{9/2}$ and $^4S_{3/2}$ multiplets at 80K and room temperature. These lifetimes proved unfavourably low for several common lasing channels.

Mahius *et al* [4] studied the gadolinium salt K_2GdF_5, which also possesses the orthorhombic linear-chain structure. The energy diffusion and transfer processes were studied,

along with the effect of double-doping Eu^{3+} ions into the lattice. Energy-transfer was shown to be predominantly one-dimensional, along the chain structure.

Boutinard *et al* [6] have studied the effect of one-dimensional structure on cross-relaxation rates in Tb^{3+}-doped K_2YF_5 . These workers observed that the decay rates for the $^5D_3$-$^5D_4$ cross-relaxation in Tb^{3+} showed very little concentration dependence. The concentrations used in this study ranged from 0.1 to 1 mol% Tb. Their results indicate that the Tb^{3+} ions are not homogeneously distributed through the lattice. The dopant instead forms clusters, probably ion-ion pairs along the K_2YF_5 chain.

1.4 Overview of this thesis

The purpose of this thesis was to study the observed upconversion emissions in K_2YF_5:Er^{3+}. To assist in describing the observed emission, detailed knowledge of the crystal-field energy levels was gained through optical absorption studies, laser spectroscopy and time-resolved spectroscopy.

The first three chapters of this thesis are designed to provide an overview of the subject matter of this study, and the methods used to collect the results. This chapter presents a background of both the host material, and the dopant rare-earth ion, erbium. Motivations are provided for both this study, and those of previous workers. Chapter 2 gives a brief summary of those parts of the theory of rare-earth spectroscopy that are relevant to this study. In Chapter 3, I give details of the experimental procedures used to obtain the data in this thesis.

The experimental work is naturally divided into two sections. In the first section (Chapter 4) the initial spectroscopy of the system is presented.

- Optical absorption studies give data for the energies of crystal-field levels between 10000 and 30000cm^{-1} .
- Fluorescence lifetimes were recorded at various temperatures for several multiplets.
- Selective laser excitation experiments provide evidence of a secondary crystallographic centre.
- A preliminary fit was made to the observed crystal-field energy levels using a trigonal C_{3V} symmetry Hamiltonian.

The second section (Chapter 5) details a study of the upconversion processes observed for Er^{3+} ions in the material.

- Sequential two-photon absorption processes leading to infrared-to-visible upconversion from excitation into each of the $^4I_{11/2}$ and $^4I_{9/2}$ multiplets.
- Simultaneous higher-order processes leading to emissions in the blue and ultraviolet in both cases.
- Red-to-green upconversion resulting from excitation into the $^4F_{9/2}$ multiplet.
- A study of the bleaching of fluorescence from laser excitation into the $^4I_{11/2}$ multiplet.

Finally, Chapter 6 presents the conclusions of this study, and gives suggestions for further work. A bibliography of work cited in this thesis is also included.

Chapter 2

Theoretical considerations

This chapter outlines those parts of the theory of rare-earth ion spectra that have been used in this thesis. Several authors have reviewed this material in depth, notably Wybourne [8], whose work this chapter most closely follows.

2.1 A summary of crystal field theory

The free ion

The properties of rare-earth ions are characterised by the $4f^N$ electron configuration. It is useful therefore to start with the non-relativistic expression of the Hamiltonian for such an N-electron system. This leads naturally to the development of the central-field approximation, and of solutions for the free-ion wavefunctions. The free-ion Hamiltonian is written as

$$H = \left[-\frac{\hbar^2}{2m}\sum_{i=1}^{N}\nabla_i^2 - \sum_{i=1}^{N}\frac{Ze^2}{r_i} + \sum_{i<j}^{N}\frac{e^2}{r_{ij}}\right] + \sum_{i=1}^{N}\zeta(r_i)l_i\cdot s_i.$$

In the above expression, the first term represents the kinetic energy of each of the N electrons while the second is the potential energy of each in the electrostatic field of the nucleus. The last two terms represent the electrostatic repulsion between individual electrons, and the spin-orbit interaction respectively. The weaker of the magnetic interactions, the *spin-spin* ($s_i \cdot s_j$), *orbit-orbit* ($l_i \cdot l_j$) and *spin-other-orbit* ($l_i \cdot s_j$), are omitted for brevity, although they can also have a significant effect on the free-ion Hamiltonian. An exact solution of this Hamiltonian is not possible for any system of more than one electron.

The central-field approximation

To find a solution of the N-electron Hamiltonian, the *Central-Field Approximation* is employed. In this model, each electron is considered to be moving independently in a central-field consisting of the field of the nucleus, and an averaged field of the other 4f electrons. The central-field Hamiltonian, H_{cf} can then be written

$$H_{cf} = \sum_{i=1}^{N} \left[-\frac{\hbar^2}{2m}\nabla_i^2 + U(r_i) \right].$$

The difference between the free-ion Hamiltonian, and that for the central field, $H - H_{cf}$ is now treated as a perturbation, V, to H where

$$\begin{aligned} V &= H - H_{cf} \\ &= \sum_{i=1}^{N} \left[-\frac{Ze^2}{r_i} - U(r_i) \right] + \sum_{i<j}^{N} \frac{e^2}{r_{ij}}. \end{aligned}$$

The Schrödinger equation for the above central-field Hamiltonian is solvable in terms of N single-ion hydrogen-like wavefunctions, $\psi_i(nlm_l)$. Each of the one-electron wavefunctions can be further separated into its radial and angular parts:

$$\psi_i(nlm_l) = r_i^{-1} R_{nl}(r_i) Y_{lm_l}(\theta_i, \phi_i)$$

where the radial part R_{nl} is related directly to $U(r_i)$. The angular spherical harmonics Y_{lm_l} are defined as

$$.Y_{lm_l}(\theta, \phi) = (-1)^m \left[\frac{(2l+1)(l-|m|)!}{4\pi(l+|m|)!} \right]^{1/2} P_l^m(cos\theta) e^{im\phi}$$

where P_l^m(w) are the Legendre polynomials. This expression allows for an exact numerical solution for the angular part only, the radial function R_{nl} is dependent upon the form of the central-field and can be approximated only.

The inclusion of the spin quantum number m_s into the above hydrogenic solutions introduces the spin coordinate σ, with values $\pm\frac{1}{2}$ and the associated spin function $\delta(m_s, \sigma)$. In order to satisfy the Pauli exclusion principle, a linear combination of the solutions $\psi_i(nlm_lm_s)$ must be found such that the wavefunctions of each are antisymmetric. The resulting solution has the form

$$\Psi = \frac{1}{\sqrt{N!}} \sum_{p}^{N} (-1)^p P\psi_1\psi_2...\psi_N$$

where the permutation of the electrons is represented by P, and the parity of the permutation by p.

Coupling schemes

Calculation of the matrix elements of the perturbation operator V is made easier by first defining the states of the electronic configuration in a well-defined coupling scheme. In general, one is interested only in the states of a single configuration. In the case of the spectroscopy of Er^{3+} ions, the configuration under study is $4f^{11}$. The separation between the energy states of different configurations is large enough that we can consider the $4f^{11}$ states in relative isolation.

The *Russell-Saunders* coupling scheme (LS coupling) involves combining the orbital angular-momenta of the electrons vectorially to give a total orbital angular momentum L. Similarly, the various electronic spins are combined to give a total spin angular momentum S. The two quantities L and S can be shown each to commute with the electrostatic repulsion term from the free-ion Hamiltonian already given, and with their sum, J, the total angular momentum. It follows that the electrostatic repulsion interaction is independent of J, and diagonal in S and L. The electronic configuration is split by this interaction into *LS terms* that are characterised by the total spin, and total orbital angular momentum of the electrons. The notation commonly used for the LS terms is the form ^{2S+1}L where L is represented by the standard spectroscopic notation (S=0, P=1, D=2, F=3, and so on).

The spin-orbit interaction term in the free-ion Hamiltonian is diagonal in the total angular momentum, J, but not in the total orbital angular momentum L or the total spin angular momentum S. The spin-orbit interaction splits the LS terms of the electrostatic interaction into *multiplets* with different J values. The notation for the LSJ multiplets is identical to that for the LS terms, with a subscript denoting the J value, ie. $^{2S+1}L_J$

The spin-orbit interaction has off-diagonal elements that mix multiplets with the same J value. When this interaction is significant the LS coupling of the electrons is said to be broken. Now a single multiplet will be a combination of mixed LS terms with the same J value. For example, the calculated free-ion wavefunction of the $^4S_{3/2}$ multiplet of Er^{3+} is of the form,

$$\begin{aligned}\left|{}^4S_{3/2}\right\rangle &= 0.8278\left|{}^4S_{3/2}\right\rangle + 0.0436\left|{}^4D_{3/2}\right\rangle + 0.2224\left|{}^4F_{3/2}\right\rangle \\ &- 0.4324\left|{}^2P_{3/2}\right\rangle - 0.2207\left|{}^2D^{(1)}_{3/2}\right\rangle - 0.0241\left|{}^2D^{(2)}_{3/2}\right\rangle .\end{aligned}$$

To avoid confusion in the labelling of the multiplets, the common convention is adopted in this thesis, that is, the label of the multiplet is the same as the largest component of the linear combination.

This coupling scheme that combines both the electrostatic and the spin-orbit interactions together into the same calculation is known as intermediate coupling, or sometimes J-mixing. Whilst this method can involve very large matrix calculations, the modern computer has more than enough computing power.

The form of the free-ion Hamiltonian that is ultimately used in the electronic level analysis is [9]

$$\begin{aligned} H &= \sum_{k=2,4,6} F^k f_k + \sum_i \zeta \, \boldsymbol{l}_i \cdot \boldsymbol{s}_i + \alpha L(L+1) + \beta G(G_2) + \gamma G(R_7) \\ &\quad + \sum_{k=0,2,4} M^k m_k + \sum_{k=2,4,6} P^k p_k + \sum_i T^k t_k. \end{aligned}$$

The electrostatic term has here been separated into an angular (F^k) and radial part (f_k). Also separated into angular and radial parts in the same way are the two- and three-body electrostatically correlated magnetic interactions ($P^k p_k$ and $M^k m_k$ respectively), and the various other magnetic effects. The α, β and γ parametrised components represent a correction to the Hamiltonian for the inter-configurational interactions. [8, 9]

The crystal field

The spherically-symmetric Hamiltonian given for the free-ion is necessarily invariant under the operations of the three-dimensional rotation group, R_3. Each LSJ-multiplet in the free-ion represents a $(2J+1)$-fold degeneracy, corresponding to the projection J_z of the total angular momentum with values from J to $-J$ in integer steps.

When the rare-earth ion is placed in the crystal environment, its symmetry is reduced to the point group corresponding to the symmetry about the ion. The lowering of the free-ion symmetry to that of the ion site lifts the degeneracy of the LSJ multiplet. The result is to split each multiplet into crystal-field levels that can be characterised by the irreducible representations of the subgroup of R_3 that is associated with the point-group symmetry. The number of non-degenerate energy levels can be determined using the transformation properties and character of the point-group. These properties can be found tabulated in the literature [10].

For a configuration with an odd number of electrons, such as Er^{3+} , any symmetry lower than cubic will split a given LSJ multiplet into $(2J+1)$ crystal-field levels. However,

only half this number of the $LSJJ_z$ levels will be distinct. The Hamiltonian interactions described previously all have the property of time-reversal symmetry. Further, Kramers theorem gives the result that such an Hamiltonian with the property of time-reversal symmetry will leave an N-odd system of electrons with at least a two-fold degeneracy. For these ions, known as 'Kramers ions' (e.g. Er^{3+}), a two-fold degeneracy exists for the $LSJJ_z$ levels that cannot be removed by an electric field. Hence each distinct J_z level in a system with an odd number of electrons will be two-fold degenerate.

As for the interactions previously described, the Hamiltonian corresponding to the crystal-field interaction can be separated into radial and angular parts. It is usual to write it of the form

$$H_{crystal field} = \sum_{k,q} B_q^k C_q^{(k)}.$$

The radial factors B_q^k are difficult to calculate theoretically, and are treated as parameters to be fitted experimentally, while the angular parts are expressed in terms of the Racah spherical tensors. The Racah tensors are themselves related to the spherical harmonics by

$$C_q^{(k)} = \sqrt{\frac{4\pi}{2k+1}} Y_{kq}.$$

The values of the parameters k and q are limited by the symmetry of the rare-earth ion site. The value of k is also constrained to be even by parity considerations, and by the angular-momentum triangle rule to be no greater than 6. As the crystal-field at the position of the rare-earth ion must display the same symmetry as the crystallographic site, the Hamiltonian must therefore be invariant under the actions of that symmetry. In the case of trigonal C_{3V} symmetry appropriate here, this restricts the parameter q to the values 0, ± 3 and ± 6.

The relative magnitudes of each of the various interactions of the rare-earth ion in the crystal environment are shown in Figure 2.1.

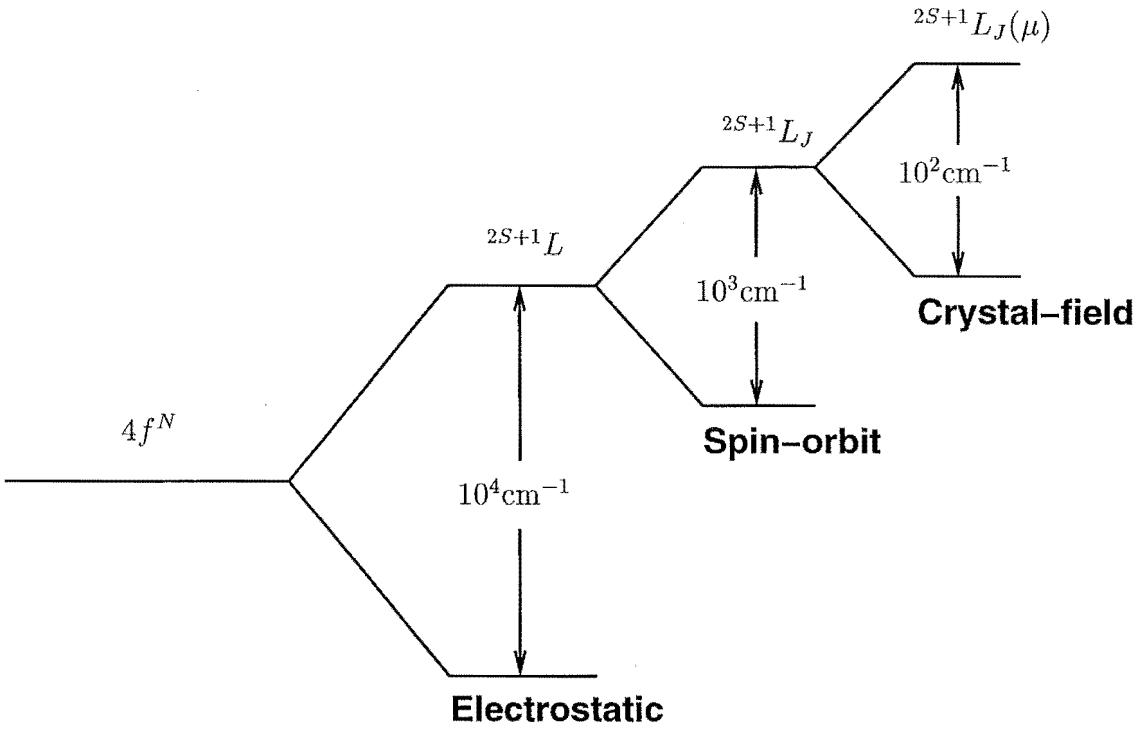

Figure 2.1: The approximate relative splittings of the various interactions of a rare-earth ion in the crystalline environment.

Transition selection rules and polarisation

The symmetry of the rare-earth ion site plays a vital part in deciding whether or not an electronic transition between two crystal-field levels is possible. The most significant terms in the matter-radiation interaction are those of the magnetic and electric dipole. In order for the transition probability to be non-zero, one or both of these interactions must have non-zero matrix-elements.

The Hamiltonian of the crystal-field interaction is invariant under the operations of the point-group symmetry of the crystal. Each $LSJJ_z$ state can therefore be associated with an irreducible representation of that point-group, as tabulated in Koster *et al* [10].

The matrix element $\langle\psi_i|H_{op}|\psi_f\rangle$ of an operator between an initial state ψ_i and final state ψ_f is non-zero only if

$$\Gamma_{op} \times \Gamma_i \supset \Gamma_f,$$

where Γ_{op} is the appropriate irreducible representation ('irreps' hereafter) of the interaction operator in the point-group in question. The $\Gamma_{i,f}$ represent the irreps of the initial and final $LSJJ_z$ crystal-field levels respectively.

The irreps for magnetic and electric dipole operators can be found in Koster *et al* [10], and are for C_{3V} symmetry,

$$\begin{aligned} \text{Electric Dipole} : \Gamma_{\text{ED}} &= \Gamma_1 + \Gamma_3 \\ \text{Magnetic Dipole} : \Gamma_{\text{MD}} &= \Gamma_2 + \Gamma_3 \end{aligned}$$

Tabulated multiplication tables for the various point-group symmetries allow one to determine selection rules governing either type of transition. The basis states of the operator irreps also gives information as to the direction of the exciting or emissive radiation relative to the principal axis of the site.

In general the notation σ, π is adopted for the polarisations of the incident and emitted radiation with respect to the symmetry axis of the site. In this notation, σ represents an absorption or emission of radiation with the **E** vector polarised perpendicular to the symmetry axis of the site, and π the parallel case. For the magnetic dipole interaction, these polarisations refer to the **B** vector of the radiation and are labelled σ' and π'

The ion Er^{3+} is a Kramers ion with crystal-field wavefunctions having irreps Γ_4, Γ_5 and Γ_6. in C_{3V} symmetry, however, the Γ_5 and Γ_6 irreps always appear as a degenerate

pair. The electric dipole and magnetic dipole selection rules are given for this ion in the C_{3V} symmetry in Tables 2.1 and 2.2.

Symmetry considerations strictly forbid electric dipole transitions between pure states of the $4f^N$ configuration. However, for rare-earth ions the majority of transitions are of this nature as the admixture from higher configurations introduces small components of opposite parity states. Magnetic dipole transitions are allowed between $4f^N$ states and are often seen with weak intensities in rare-earth ion spectra.

ED	Γ_4	$\Gamma_{5,6}$
Γ_4	$\pi\sigma$	σ
$\Gamma_{5,6}$	σ	π

Table 2.1: Electric dipole selection rules for C_{3V} symmetry

MD	Γ_4	$\Gamma_{5,6}$
Γ_4	$\pi'\sigma'$	σ'
$\Gamma_{5,6}$	σ'	π'

Table 2.2: Magnetic dipole selection rules for C_{3V} symmetry

Chapter 3

Experimental equipment and procedures

3.1 Sample materials and preparation

The samples of $K_2YF_5:Er^{3+}$ used in this thesis were grown by Professor N. Khaidukov, at the Institute of General and Inorganic Chemistry in Moscow, Russia. The crystallisation of the LiF - KF - LnF_3 - H_2O systems (here Ln denotes a rare-earth ion) under high temperatures and pressures (hydrothermal conditions) has produced several complex rare-earth fluorides, including those used in this study. The single crystals had an average size of 5mm in length, and roughly 1mm in diameter. The material was a colourless, brittle crystal, with a roughly hexagonal cross-section.

Given the small average size of the $K_2YF_5:Er^{3+}$ crystals supplied, extra preparation was avoided as far as possible, to reduce the risk of damage. For the most part the samples performed well as supplied, however, in the case where a 'clean' entry/exit path was required for the laser beam, some small polishing on the end face(s) was needed.

3.2 Cryogenics techniques

For the majority of experiments performed it was necessary to cool the sample to cryogenic temperatures. Low temperatures decrease the probability that higher ground-state energy levels will be thermally populated, and the resulting spectra are simpler, and easier to interpret. Low temperatures also reduce the thermal broadening of the observed transitions. The techniques described below attained a temperature of roughly 12K.

The samples were mounted in custom-built copper holders with a 'copper-putty' mixture of ground copper and vacuum grease to aid thermal contact. Due to their delicate nature, no attempt was made to hold the samples in place using screw-held plates.

The sample holder was screwed onto the cold head with indium foil at the contact point to provide better thermal conductivity. For all optical experiments, including laser-

selective excitation, upconversion excitation and optical absorption, the cold-head unit was attached to a CTI Cryogenics model 21C closed-cycle helium cryostat, which allowed cooling to a base temperature of 10K. Intermediate temperatures could be obtained by passing current through a series of heater resistors attached to the cold-head, under control by a department-built temperature controller/thermostat unit. A diffusion/rotary pump system evacuated the cold-head housing to increase the cryogenic system to a workable efficiency. A similar, although newer CTI model 8200 compressor unit was used for the infrared absorption work, although evacuation in that case was provided by a liquid nitrogen cold-trapped rotary pump.

3.3 Optical absorption

The source for optical absorption spectra was a tungsten-halogen lamp. Two bulbs of either 100W or 20W, powered by 12V power supplies were used. The hotter 100W bulb, gave considerably more intensity in the near ultraviolet, although suffered from a noisier signal. Where possible the quieter 20W bulb was used.

The light from the lamp was focused onto the sample, then the transmitted light refocused onto the slits of a Spex 1701 0.75 single-grating monochromator. The light was detected using either a red-sensitive EMI 9558 photomultiplier tube (approximate spectral range 450-850nm), a blue-sensitive EMI 6255 photomultiplier tube (approximate spectral range 200-600), or an infrared-sensitive RCA 7102 photomultiplier tubes (spectral range 0.5-1.1μm) . The red and blue photomultiplier tubes were housed in thermoelectric cooling units at temperatures of -25°C, while the infrared tube was liquid nitrogen cooled. The photomultiplier tube current was measured using a Keithley 610B electrometer, the output from which was then digitised on a department-built voltage-to-frequency converter, for recording by the laboratory computer.

To avoid a spectral response defect at roughly 590nm in the first order of the grating of the Spex 1701 monochromator, second order was predominantly used, in conjunction with appropriate Corning Glass filters to remove effects of different orders.

Crystal temperature could be varied with the closed-cycle helium compressor discussed earlier.

3.4 IR spectroscopy

For absorption measurements in the mid-infrared a Bio-Rad FTS-40 Fourier-transform infrared spectrometer was used. Two beam-splitter and source set-ups were available to cover the range from 700cm^{-1} to 11000cm^{-1} . The near-infrared set-up consisted of a tungsten-halogen lamp, a quartz beam-splitter, and an indium-antimide detector, this gave a useful range of 3000-11000cm^{-1} . Absorption to the $^4I_{13/2}$ and $^4I_{11/2}$ multiplets of Er^{3+} lie well within this range at around 6500cm^{-1} and 10300cm^{-1} respectively. Further into the infrared, a combination of a thermal glow-bar, a KBr beam-splitter, and a mercury-cadmium-telluride detector was used, for the 700-4500cm^{-1} region.

The Fourier-transform spectrometer system works on a principle of recording an interferogram between the transmitted light from the sample, and the original source. To reduce noise quantities in this method, it is advantageous to collect more than one interferogram, the average having a higher signal-to-noise ratio. In this study, a maximum of 256 scans were taken over a scanning time of roughly 40mins, though little considerable increase in the signal:noise ratio was observed between averaging 64 and 256 scans.

In these experiments the samples were cooled using the cryogenic techniques given in Section 3.2 above.

3.5 Laser spectroscopy and LSE techniques

The majority of this study of $K_2YF_5:Er^{3+}$ involved laser spectroscopy. These powerful techniques involve tunable laser sources resonantly exciting optical absorption transitions in the sample, whilst spectrometers record either single-frequency, or broad-band emissions.

Laser selective excitation (LSE) techniques were first developed by Tallant and Wright [11] in the study of $CaF_2:Er^{3+}$. This method allows different symmetry sites in the same sample to be distinguished, and classified. Where several centers exist in a crystal, their spectral lines will often overlap, increasing the difficulty of interpreting the results of, for example, an absorption study. If a laser is tuned over this region, then the emissions observed will characterise only the site(s) involved. Specifically, if a particular (preferably strong and isolated) fluorescence line of a site is monitored, then only the excitation lines of the same site should produce the emission. In this manner, the various distinct spectroscopic sites and their energy level structures can be classified.

A variety of laser sources were used in this study. The principal work was carried out

with excitation in the infrared with a Coherent model 899 tunable titanium-sapphire ring laser, pumped by a Spectra-Physics Beamlok 2040 argon-ion laser. The Ti:S laser source is equipped with three full sets of optics, covering a considerable range of infrared emission. The 'short-wave' optics set has a tunable range in the near-IR, 11800-14200cm^{-1}. This range allows for excitation of the $^4I_{9/2}$ multiplet of Er^{3+} , which has energies of around 12400cm^{-1} . The 'long-wave' optics set gives a frequency range of 9400-11100cm^{-1}, ideal for the excitation of the $^4I_{11/2}$ multiplet of Er^{3+} . The third 'medium-wave' optics set was not used.

Besides the solid-state Ti:S laser, a Spectra-Physics dye-laser system was also used. Coumarin 540 dye was appropriate for excitation of the $^4S_{3/2}$ multiplet of the Er^{3+} ion. This dye was mixed to a concentration of 1.25x10^{-3} mol/l in ethylene glycol, with not more than 50ml/l of benzyl alcohol added to improve solubility. The dye was pumped by the 488nm line of the argon-ion laser, at about 4W of input power and gave a tunable spectral range of 521-551nm, with a peak output power of 40mW at 538nm.

Another dye, Rhodamine 640 (Rhodamine 101) was used to excite the $^4F_{9/2}$ multiplet of the Er^{3+} ion. This dye was mixed to a concentration of 2x10^{-3} mol/l in ethylene glycol, with 1x10^{-3} mol/l of another dye, Rhodamine 590. This gave output powers of up to 200mW in a lasing range of 620-690nm.

The beams from both types of laser systems were directed and focused onto the samples using mirrors and a lens. The emission from the samples could be recorded in two opposite directions and analysed by two different spectrometers. The laboratory geometry used is shown in Figure 3.1.

The polarisation of the beams from both types of laser source, initially in the Y direction, could be rotated to an arbitrary angle with the use of a Spectra-Physics 310 polarisation rotator. The analyser shown in Figure 3.1 could be used to detect emissions polarised in either the X or Y direction.

The laser spectroscopy work done in this study involved three basic types of measurement: broad-band excitation, narrow band excitation, and fluorescence (both up- and down-converted).

Broad-band excitation involves continuosly scanning the laser wavelength through the energy levels of a specific multiplet while monitoring the total emission from the sample over a wide band-pass. As all emissions in the band-pass are recorded, the resulting spectrum is not site-selective, and can be expected to show the excitation lines of each site, in proportion to their relative strengths.

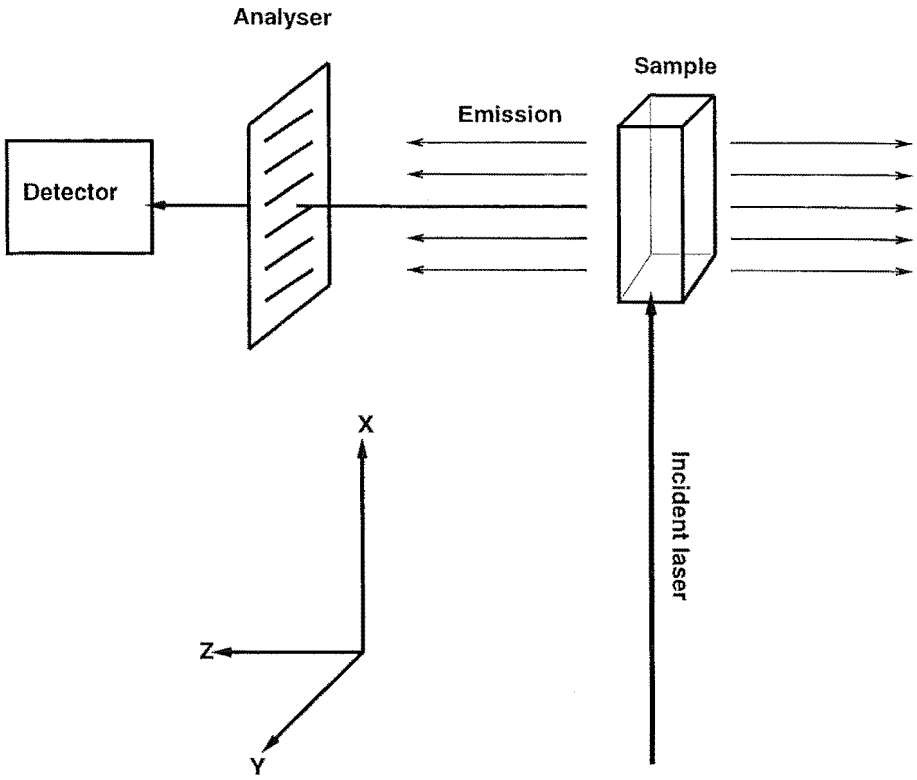

Figure 3.1: Experimental geometry for laser work.

The emission recorded was either the normal down-converted fluorescence from lower energy levels or, in the case of upconversion studies, higher-energy emitting multiplets. The emission was recorded on a high band-pass spectrometer, either a 0.25m Bausch and Lomb single monochromator, or the SPEX 1701 with open slits, and set in zero order. Appropriate filters from the Corning Glass range were used to remove radiations from outside the region of interest. Several photomultiplier tubes were used for various regions of interest. The Bausch and Lomb spectrometer had two grating set-ups, one covered the visible region (350-800nm) the other the ultraviolet (180-400nm). Either a blue-sensitive EMI 6255, or a red-sensitive EMI 9558 photomultiplier were used with this device. A liquid nitrogen cooled RCA 7102 infrared photomultiplier tube was with the SPEX 1701 spectrometer to obtain broad-band infrared measurements.

With fully open slits, the Bausch and Lomb device has a band pass of about 50nm, larger in general than the crystal-field splittings of the rare-earth ion multiplets, while that of the SPEX 1701 spectrometer varied depending upon the particular filter or filters in use.

Narrow-band excitation. When a single emission line from a crystal-field site is monitored using a narrow band-pass spectrometer, signal is detected only when other

transitions of that site are excited. Thus, a narrow-band excitation spectra consists of the excitation lines of a single site.

Combined with the non-site-selective information from broad-band spectra, one can determine which of the excitation features are, or are not associated with a specific symmetry site.

The spectrometers used to record these narrow-band excitation spectra were a SPEX 1403 double-monochromator and a SPEX 1701 monochromator, this time with small slits. For the SPEX 1403, a resolution of better than $0.1cm^{-1}$ is obtainable with slits of $10\mu m$, although for the most part this accuracy was not required. Usually more generous 50-250μm slits gave optimum signal and resolution conditions. An RCA C31034 photomultiplier is in use with this spectrometer. The usable scanning range of the SPEX 1403 / RCA C31034 combination is 11000-33000cm^{-1} .

The SPEX 1700 0.75m single-grating spectrometer has the advantage of more signal throughput, but also consequently higher noise due to scattering off the grating. Slit settings of $5\mu m$ gave a resolution of roughly 0.1Å. The SPEX 1701 was used primarily for regions where the SPEX 1403 / RCA C31034 combination could not attain useful signals/noise ratios. Weak ultraviolet signals were recorded using the blue-sensitive EMI 6255 photomultiplier tube described above, in conjunction with appropriate filters. Similarly infrared emission from the $^4I_{11/2}$ multiplet of Er^{3+} was detected with the SPEX 1701 spectrometer and RCA 7102 IR photomultiplier.

Fluorescence measurements involved a similar narrow-band setup to the above. The laser was tuned onto a specific excitation line, and either the SPEX 1403, or the SPEX 1701 spectrometers (described above) were scanned across a set range, recording an emission spectrum. If the position of the laser is that of an excitation transition for a specific site, then only that site will emit. If however, the laser position has several overlapping excitation transitions from several symmetry sites, then the fluorescence spectrum will be a combination of emission lines from each site, weighted according to each site's excitation strength at that position.

3.6 Time-resolved spectroscopy

Fluorescence lifetimes were recorded using a Photochemical Research Associates (PRA) LN107 dye laser system. The pulsed excitation for this dye laser were provided by a complementary PRA model LN1000 nitrogen laser. The nitrogen laser emits in the ultraviolet, at 337nm. This excites two dye cells, the first to establish laser action off a tuning

grating, and the second to provide amplification to useable powers.

Running at optimum levels the nitrogen laser yielded 600ps duration pulses, with energies of 1mJ. The ultraviolet radiation is split into two beams, one into each of the lasing (40%) and amplification (60%) stages. After amplification, the dye laser output is of the order of 100μJ. Coumarin 500 dye was used, at the edge of its lasing range to excite directly into the $^2H_{11/2}$ multiplet of Er^{3+} .

Lenses and other standard optics focussed the pulsed beam into the sample, and collected the resulting emissions. An EMI 9659 QA photomultiplier tube was used in conjunction with a SPEX 1701 monochromator for detection. The signal from the photomultiplier was input into an Hitachi model VC 6275 digital storage oscilloscope, on which the transients were recorded. Various resistors were used to match the impedance of the cable into the oscilloscope, to provide the most accurate lifetimes. Due to the digital nature of the scope, up to 256 transients could be recorded and averaged, significantly improving the signal-to-noise ratio.

Chapter 4

Spectroscopy of Er^{3+} -doped K_2YF_5

4.1 Absorption spectroscopy of K_2YF_5:Er^{3+}

Optical absorption spectroscopy was performed on samples of K_2YF_5:Er^{3+} , with a nominal concentration of 0.6% and 0.06% of the rare-earth dopant. The spectra were first taken at a temperature of 12K, and again after warming to 50K to examine extra transitions present due to the increased population of the higher ground-state energy levels. Due to the small size of the samples, care was taken that only the light transmitted through the sample was recorded. The samples used were masked to approximately the same width (1mm), and had roughly the same thickness in the optical path (also 1mm).

Absorption spectra of K_2YF_5:Er^{3+} (0.6%)

Table 4.1 lists the various K_2YF_5:Er^{3+} multiplets for which spectra were obtained, their approximate energies, and the number of distinct crystal-field levels of each. The notation adopted hereafter follows the spectroscopic convention wherein each multiplet is labelled individually by letters, as well as the more formal $^{2S+1}L_J$ notation. This labelling system has considerable precedent in the study of Er^{3+} energy levels.

Peale *et. al.* [3] have supplied results from their study of highly doped samples of K_2YF_5:Er^{3+} , the approximate energies for the multiplets A, B, D, E, F, and G above being drawn from that source. For the remaining multiplets, the approximate barycentres given by Carnall *et. al.* [1] on Er^{3+} in LaF_3 were used as a starting point in locating the multiplets. The absorption spectra obtained for the multiplets labelled A to G are displayed in Figures 4.1-4.6.

The absorption energies and transition assignments are given, with the results by Peale *et. al.* for comparison in Tables 4.2, 4.3 and 4.4

Er^{3+} multiplet		Approx. energy (cm^{-1})	No. of distinct levels
$^4I_{11/2}$	A	10100	6
$^4I_{9/2}$	B	12500	5
$^4F_{9/2}$	D	15300	5
$^4S_{3/2}$	E	18400	2
$^2H_{11/2}$	F	19200	6
$^4F_{7/2}$	G	20500	4
$^4F_{5/2}$	H	22300	3
$^4F_{3/2}$	I	22700	2
$^2H_{9/2}$	K	24800	5
$^4G_{11/2}$	L	26600	6
$^2G_{9/2}$	M	27600	5
$^2K_{15/2}$	N	27900	8
$^2G_{7/2}$	O	28200	4

Table 4.1: Er^{3+} multiplets studied by optical absorption

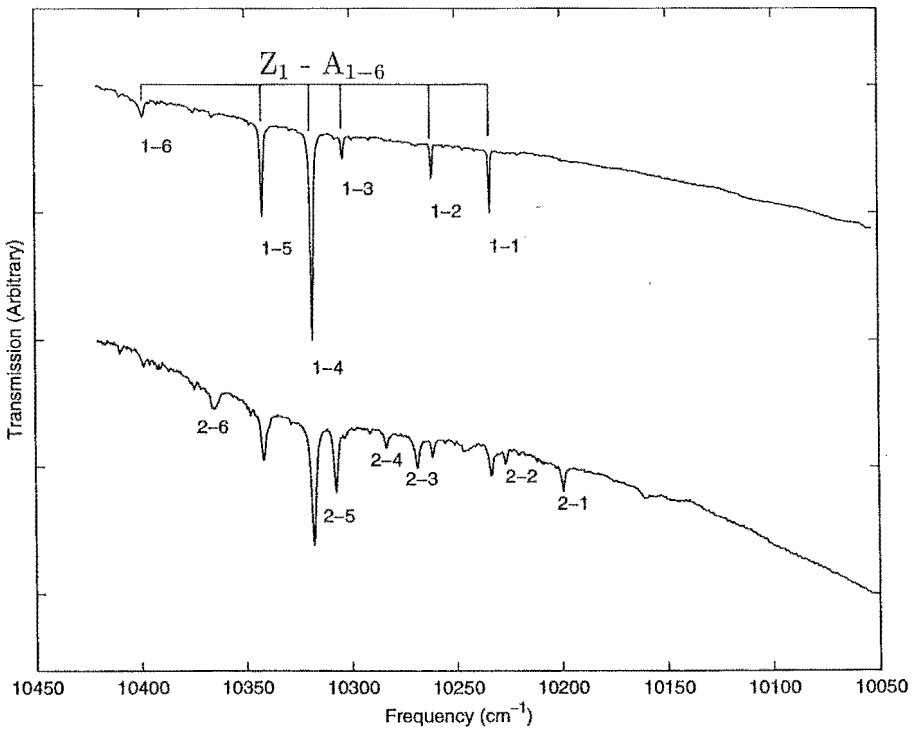

Figure 4.1: Optical absorption spectra of the $^4I_{11/2}$ (A) multiplet of K_2YF_5:(0.6%)Er^{3+} at 12K (top), and 100K (bottom). Transition assignments $Z_m \rightarrow A_n$ are labelled by m - n for brevity

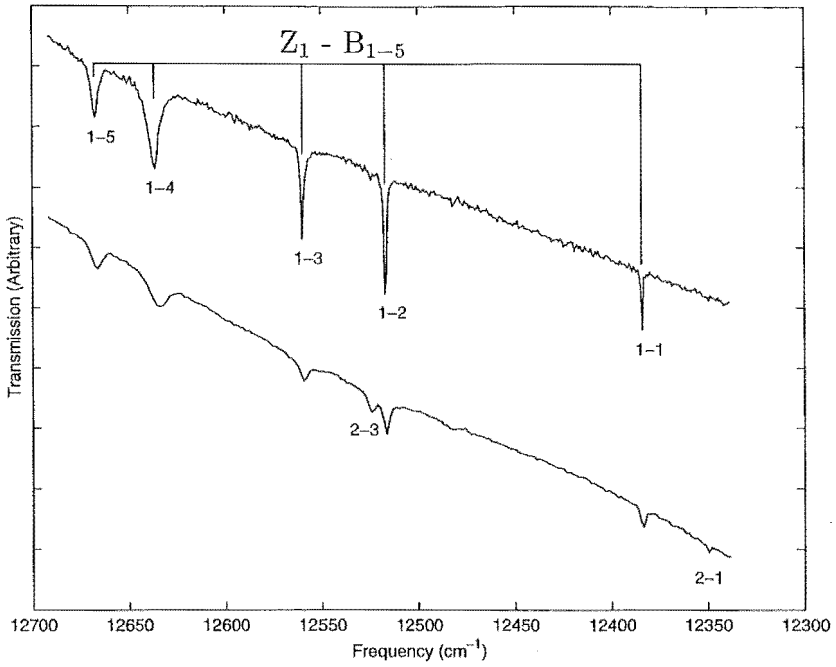

Figure 4.2: Optical absorption spectra of the $^4I_{9/2}$ (B) multiplet of K_2YF_5:(0.6%)Er^{3+} at 12K (top), and 100K (bottom). Transition assignments $Z_m \rightarrow B_n$ are labelled by m - n for brevity

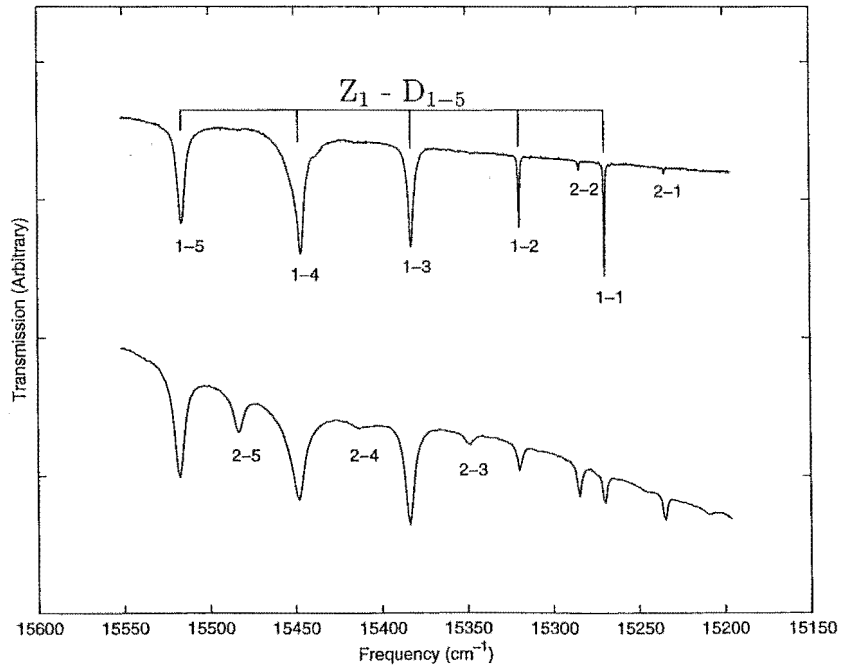

Figure 4.3: Optical absorption spectra of the $^4F_{9/2}$ (D) multiplet of K_2YF_5:(0.6%)Er^{3+} at 12K (top), and 100K (bottom). Transition assignments $Z_m \rightarrow D_n$ are labelled by m - n for brevity

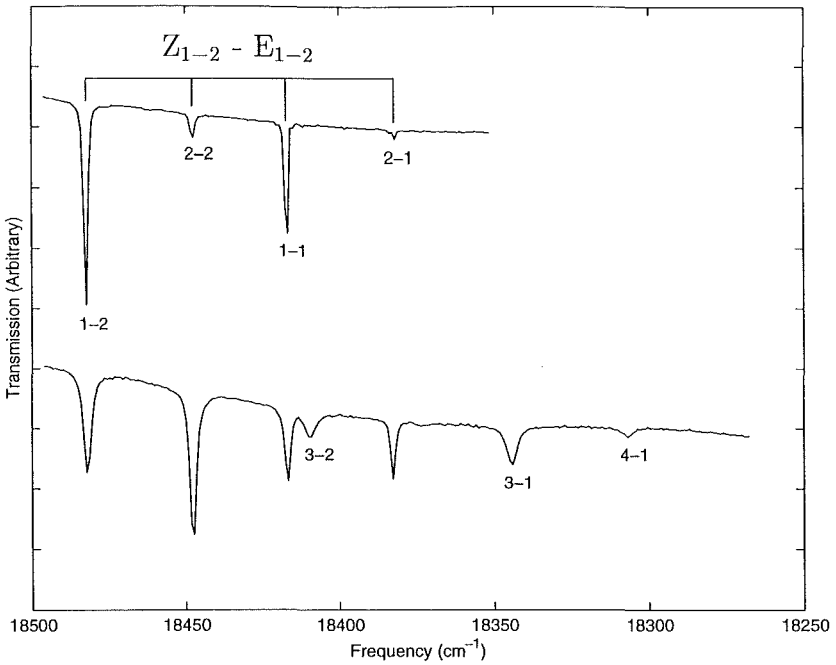

Figure 4.4: Optical absorption spectra of the $^4S_{3/2}$ (E) multiplet of K_2YF_5:(0.6%)Er^{3+} at 12K (top), and 100K (bottom). Transition assignments $Z_m \rightarrow E_n$ are labelled by m - n for brevity

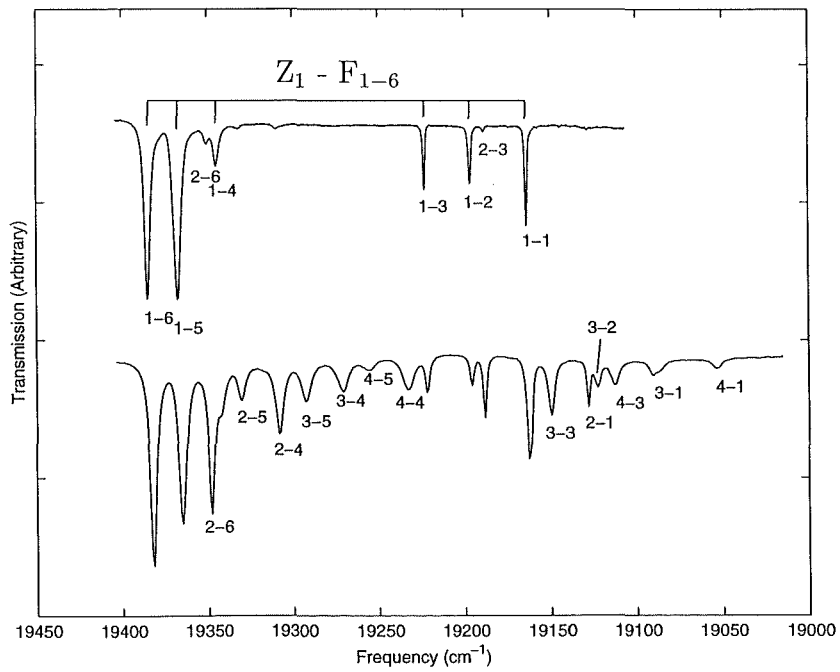

Figure 4.5: Optical absorption spectra of the $^2H_{11/2}$ (F) multiplet of K_2YF_5:(0.6%)Er^{3+} at 12K (top), and 100K (bottom). Transition assignments $Z_m \rightarrow F_n$ are labelled by m - n for brevity

Multiplet	Absorption transition	Absorption energies (cm^{-1})	
		This work	Peale *et. al.*
A ($^4I_{11/2}$)	Z_1-A_6	10397	10397
	Z_2-A_6	10364	-
	Z_1-A_5	10341	10340
	Z_1-A_4	10317	10317
	Z_2-A_5	10307	-
	Z_1-A_3	10303	10302
	Z_2-A_3	10282	-
	Z_3-A_5	10268	-
	Z_1-A_2	10260	10260
	Z_3-A_4	10245	-
	Z_1-A_1	10233	10233
	Z_2-A_2	10226	-
	Z_2-A_1	10199	-
B ($^4I_{9/2}$)	Z_1-B_5	12664	12664
	Z_1-B_4	12631	12632
	Z_1-B_3	12556	12556
	Z_2-B_3	12521	-
	Z_1-B_2	12514	12514
	Z_2-B_2	12479	-
	Z_1-B_1	12381	12382
	Z_2-B_1	12346	-
D ($^4F_{9/2}$)	Z_1-D_5	15514	15515
	Z_2-D_5	15478	-
	Z_1-D_4	15444	15446
	-	15432	-
	Z_2-D_4	15409	-
	Z_1-D_3	15379	15381
	Z_2-D_3	15344	-
	Z_1-D_2	15316	15318
	Z_2-D_2	15281	-
	Z_1-D_1	15266	15268
	Z_3-D_2	15241	-
	Z_2-D_1	15231	-
	Z_4-D_2	15205	-

Table 4.2: Optical absorption energies and transition assignments for the A, B, D and E multiplets of $K_2YF_5:Er^{3+}$. Results by Peale *et. al.* [3] are given for comparison. Energies are given to $\pm 1 cm^{-1}$.

Multiplet	Absorption transition	Absorption energies (cm^{-1})	
		This work	Peale *et. al.*
E ($^4S_{3/2}$)	Z_1-E_2	18476	18476
	Z_2-E_2	18442	-
	Z_1-E_1	18411	18411
	Z_3-E_2	18404	-
	Z_2-E_1	18377	-
	Z_4-E_2	18368	-
	Z_3-E_1	18338	-
	Z_4-E_1	18301	-
F ($^2H_{11/2}$)	Z_1-F_6	19377	19378
	Z_1-F_5	19360	19360
	Z_2-F_6	19343	-
	Z_1-F_4	19339	19338
	Z_2-F_5	19326	-
	Z_2-F_4	19303	-
	Z_3-F_5	19287	-
	Z_3-F_4	19266	-
	Z_4-F_5	19251	-
	Z_4-F_4	19228	-
	Z_1-F_3	19217	19217
	Z_1-F_2	19191	19190
	Z_2-F_3	19183	-
	Z_1-F_1	19157	19157
	Z_3-F_3	19145	-
	Z_2-F_1	19123	-
	Z_3-F_2	19118	-
	Z_4-F_3	19108	-
	Z_3-F_1	19086	-
	Z_4-F_1	19049	-

Table 4.3: Optical absorption energies and transition assignments for the $^4S_{3/2}$ and $^2H_{11/2}$ multiplets of $K_2YF_5:Er^{3+}$. Results by Peale *et. al.* [3] are given for comparison. Energies are given to $\pm 1 cm^{-1}$.

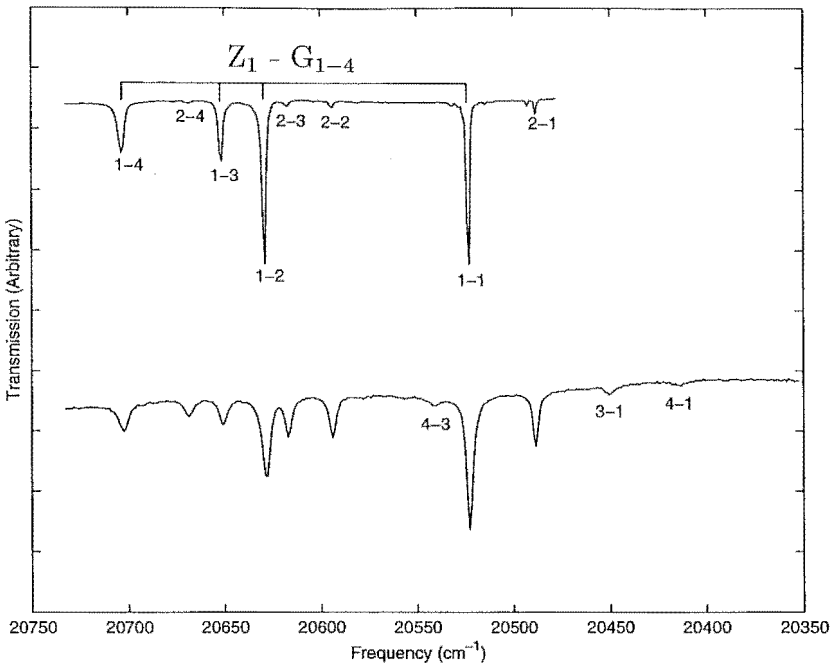

Figure 4.6: Optical absorption spectra of the $^4F_{7/2}$ (G) multiplet of K_2YF_5:(0.6%)Er^{3+} at 12K (top), and 100K (bottom). Transition assignments $Z_m \rightarrow G_n$ are labelled by m - n for brevity

Multiplet	Absorption transition	Absorption energies (cm^{-1})	
		This work	Peale *et. al.*
G ($^4F_{7/2}$)	Z_1-G_4	20698	20701
	Z_2-G_4	20663	-
	Z_1-G_3	20646	20649
	Z_1-G_2	20623	20627
	Z_2-G_3	20612	-
	Z_2-G_2	20589	-
	Z_4-G_3	20537	-
	Z_1-G_1	20518	20521
	-	20486	-
	Z_2-G_1	20483	-
	Z_3-G_1	20445	-
	Z_4-G_1	20408	-

Table 4.4: Optical absorption energies and transition assignments for the $^4F_{7/2}$ multiplet of $K_2YF_5:Er^{3+}$. Results by Peale *et. al.* [3] are given for comparison. Energies are given to $\pm 1 cm^{-1}$.

Obviously, the two sets of results (those of Peale *et. al.* [3], and those obtained in this study) are in good agreement. A small discrepancy exists however in the values of the energy levels of the ground state. The ground state ($^4I_{15/2}$ /Z) splitting values from Peale are as shown in Table 4.5.

Crystal-field level	Energy (cm^{-1})
Z_1	0
Z_2	34
Z_3	35
Z_4	37
Z_5	74
Z_6	111
Z_7	280
Z_8	502

Table 4.5: Ground state ($^4I_{15/2}$) splitting as given in Peale *et. al.* [3]. Stated accuracy is $\pm 1cm^{-1}$.

For the optical absorption spectra taken at 100K, transitions were visible between thermally populated levels of the ground state, and the crystal-field levels of the various multiplets studied. These thermal transitions were evident for the 35, 74 and $111cm^{-1}$ splittings, yet the structure given by Peale *et al* of only $3cm^{-1}$ between the Z_2,Z_3 and Z_4 crystal-field levels could not be resolved at resolutions of less than $0.5cm^{-1}$. As the temperature was raised further, thermal broadening reduced the usefulness of the technique in finding further information on the ground-state splittings. Later evidence from laser selective excitation and upconversion spectroscopy also fail to resolve this previously reported splitting.

The optical absorption spectra were extended into the 22000-$30000cm^{-1}$ range to cover the multiplets involved in upconversion emission processes. The absorption spectra obtained for the multiplets $^4F_{5/2}$ to $^2G_{7/2}$ (H-O) are shown in Figures 4.7 to 4.12.

The $^4F_{5/2}$ and $^4F_{3/2}$ multiplets lie in close proximity having barycentre energies approximately $400cm^{-1}$ apart. The lower multiplet will have sharper absorption features and thus the spectra shown in Figure 4.7 is associated with the $^4F_{5/2}$ multiplet consistent with Carnall *et al* [1] for Er^{3+} in LaF_3. Transitions that were consistent with later results were obtained for all 3 crystal-field levels of this multiplet.

The $^4F_{3/2}$ multiplet exhibited broad-spectral features consistent with its dominant relaxation mechanism being non-radiative phonon decay to the close-lying $^4F_{5/2}$ multiplet. Two extremely weak features were observed, and these have been assigned to the I_1 and

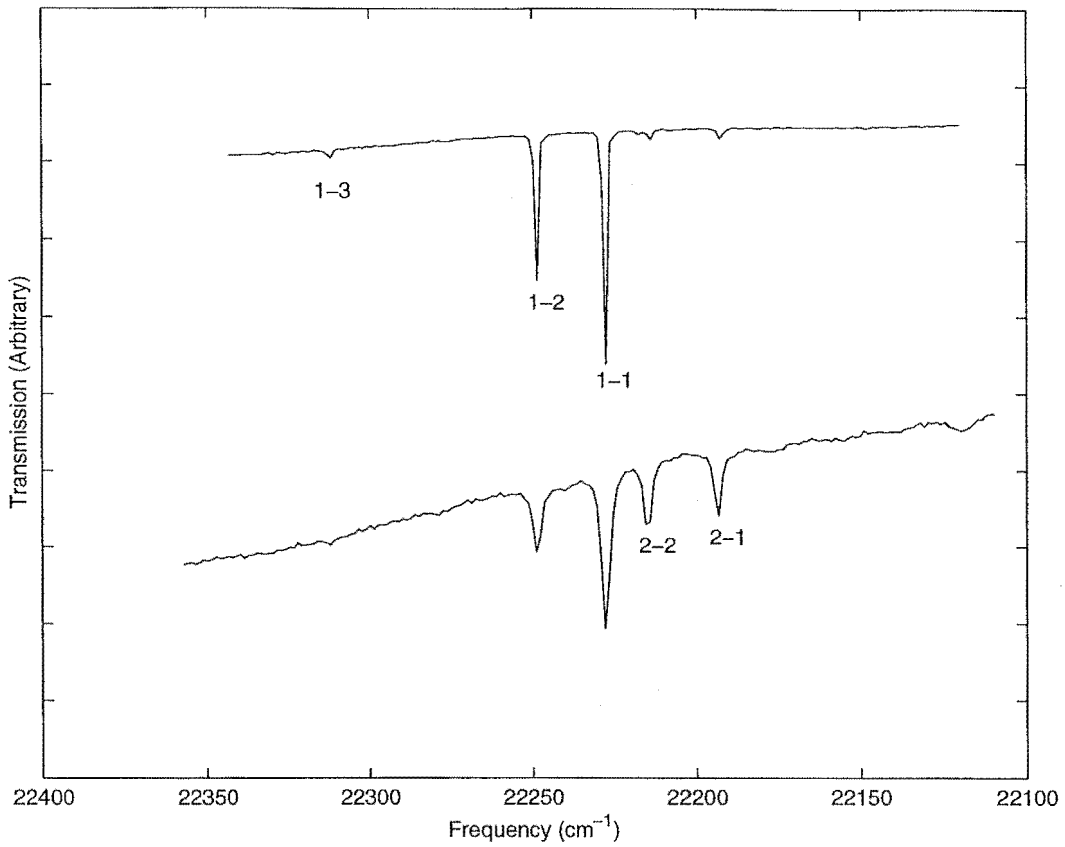

Figure 4.7: Optical absorption spectra of the $^4F_{5/2}$ (H) multiplet of K_2YF_5:(0.6%)Er^{3+} at 12K (top), and 100K (bottom). Transition assignments $Z_m \rightarrow H_n$ are labelled by m - n for brevity

I_2 crystal-field levels of the $^4F_{3/2}$ multiplet. At 100K, no absorption was visible for this multiplet due to thermal broadening.

The $^2H_{9/2}$ and $^4G_{11/2}$ multiplets were assigned again from approximate barycentre energies in Carnall *et al* , this time with little ambiguity, the transition assignments are given based on the identification of electronic transitions from thermally populated $^4I_{15/2}$ levels.

Absorption results for the region containing the $^2G_{9/2}$,$^2K_{15/2}$ and $^2G_{7/2}$ multiplets showed only one strongly absorbing multiplet, and one other set of weakly absorbing features. As no upconversion emissions have been observed from these energy levels to help correlate transitions, an assignment of the features was made based on the number of expected transitions from the known levels of the $^4I_{15/2}$ ground-state. The number of energy levels into which each LSJ-multiplet is split by the crystal field $(2J+1)$, was given in Table 4.1. The strongly absorbing multiplet clearly has features in excess of those expected for the $^2G_{9/2}$ and $^2G_{7/2}$ multiplets, so an assignment of $^2K_{15/2}$ is made for those features. It is proposed that the $^2G_{9/2}$ multiplet absorbs very weakly, and that the second

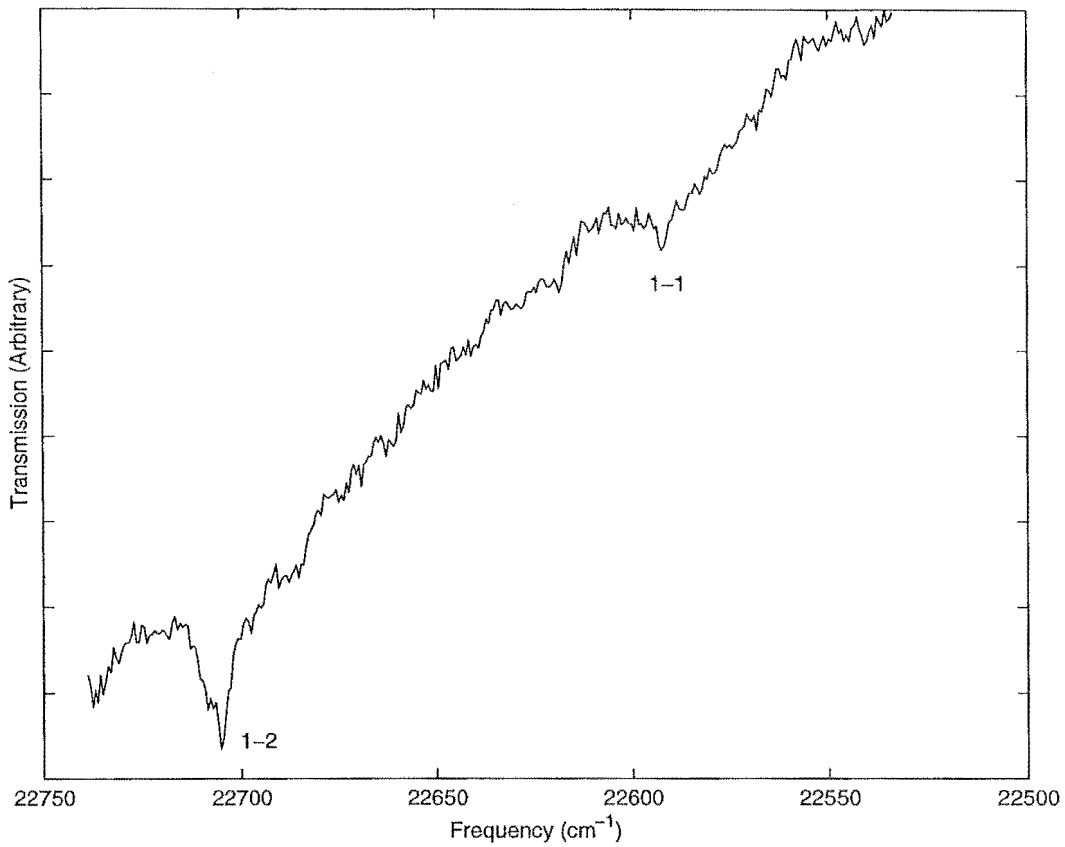

Figure 4.8: Optical absorption spectra of the $^4F_{3/2}$ (I) multiplet of K_2YF_5:(0.6%)Er^{3+} at 12K. Transition assignments $Z_m \rightarrow I_n$ are labelled by m - n for brevity

weak feature (at higher energy) is the absorption to the $^2G_{7/2}$ multiplet.

The absorption transition assignments are listed in Tables 4.6 and 4.7, along with the transition energies.

Multiplet	Absorption transition	Absorption energies (cm^{-1})
H ($^4F_{5/2}$)	Z_1-H_3	22320
	Z_1-H_2	22257
	Z_1-H_1	22235
		22225
	Z_2-H_2	22222
	Z_2-H_2	22201
		22127
I ($^4F_{3/2}$)	Z_1-I_2	22705
	Z_1-I_1	22692
K ($^2H_{9/2}$)	Z_1-K_5	24739
	Z_1-K_4	24714
	Z_2-K_4	24681
	Z_1-K_3	24648
	Z_1-K_2	24613
	Z_2-K_2	24578
	Z_3-K_2	24540
	Z_1-K_1	24522
	Z_4-K_2	24504
L ($^4G_{11/2}$)	Z_1-L_6	26656
	Z_1-L_5	26630
	Z_2-L_6	26622
	Z_1-L_4	26601
	Z_2-L_5	26596
	Z_2-L_4	26567
	Z_3-L_5	26558
	Z_3-L_4	26527
	Z_4-L_5	26520
	Z_4-L_4	26491
	Z_1-L_3	26426
	Z_2-L_3	26391

Table 4.6: Optical absorption energies and transition assignments for the $^4F_{5/2}$ to $^4G_{11/2}$ multiplets of $K_2YF_5:Er^{3+}$. Energies are given to $\pm 1 cm^{-1}$.

Multiplet	Absorption transition	Absorption energies (cm^{-1})
L ($^4G_{11/2}$)	Z_2-L_3	26391
	Z_1-L_2	26371
	Z_3-L_3	26353
	Z_2-L_2	26337
	Z_1-L_1	26332
	Z_4-L_3	26317
	Z_2-L_1	26298
	Z_3-L_1	26261
	Z_4-L_1	26223
N ($^2K_{15/2}$)	Z_1-N_8	27651
	Z_1-N_7	27628
	Z_1-N_6	27580
	Z_1-N_5	27561
	Z_1-N_4	27553
	Z_2-N_5	27526
	Z_2-N_4	27518
		27509
	Z_1-N_3	27498
	Z_2-N_3	27464
	Z_1-N_2	27457
	Z_1-N_1	27441
	Z_2-N_2	27422
	Z_2-N_1	27406
	Z_3-N_2	27384
	Z_3-N_1	27368
	Z_4-N_2	27346
O ($^2G_{7/2}$)	O(1)	28211
	O(2)	28149
	O(3)	28170
	O(4)	28144

Table 4.7: Optical absorption energies and transition assignments for the $^4G_{11/2}$, $^2K_{15/2}$ and $^2G_{7/2}$ multiplets of $K_2YF_5:Er^{3+}$. The assignments for the $^2G_{7/2}$ absorption features is arbitrary. Energies are given to $\pm 1 cm^{-1}$.

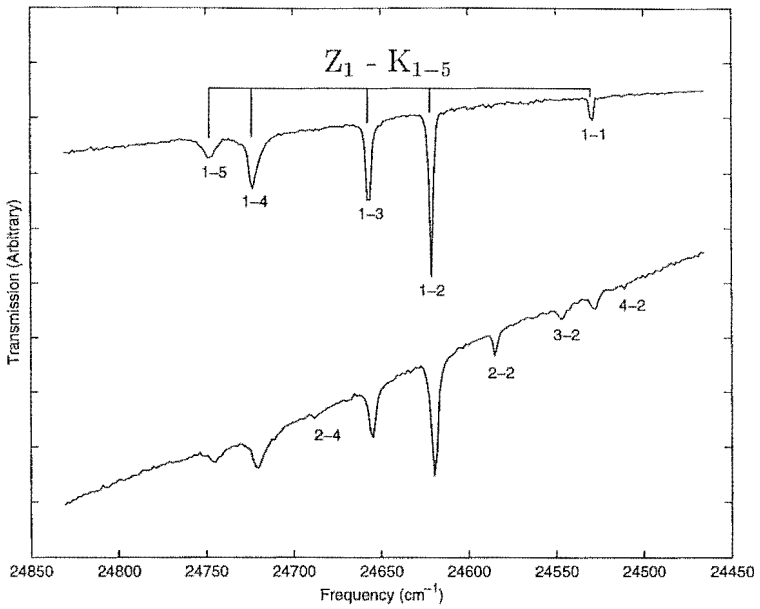

Figure 4.9: Optical absorption spectra of the $^2H_{9/2}$ (K) multiplet of K_2YF_5:(0.6%)Er^{3+} at 12K (top), and 100K (bottom). Transition assignments $Z_m \rightarrow K_n$ are labelled by m - n for brevity

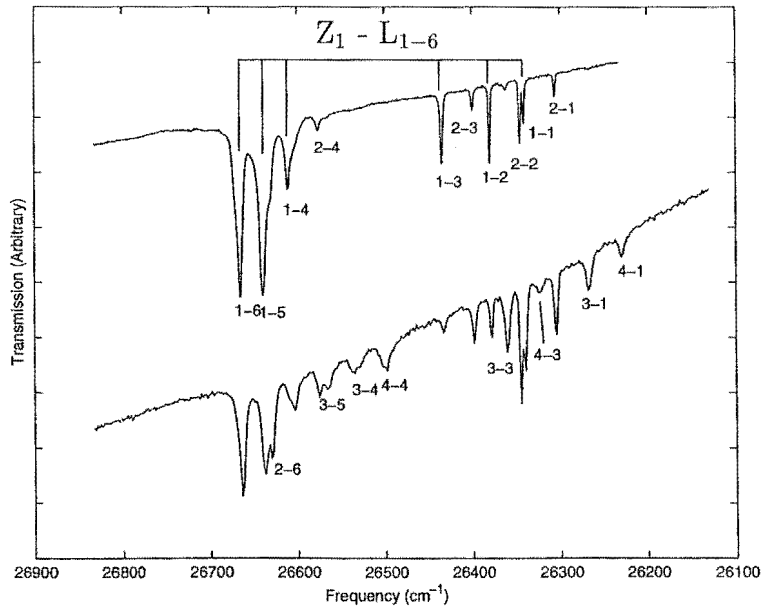

Figure 4.10: Optical absorption spectra of the $^4G_{11/2}$ (L) multiplet of K_2YF_5:(0.6%)Er^{3+} at 12K (top), and 100K (bottom). Transition assignments $Z_m \rightarrow L_n$ are labelled by m - n for brevity

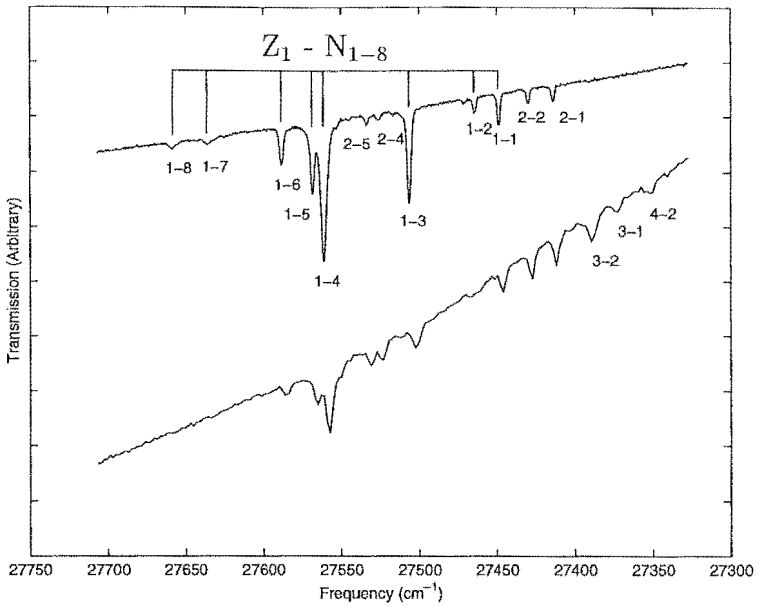

Figure 4.11: Optical absorption spectra of the $^2K_{15/2}$ (N) multiplet of K_2YF_5:(0.6%)Er^{3+} at 12K (top), and 100K (bottom). Transition assignments $Z_m \rightarrow N_n$ are labelled by m - n for brevity

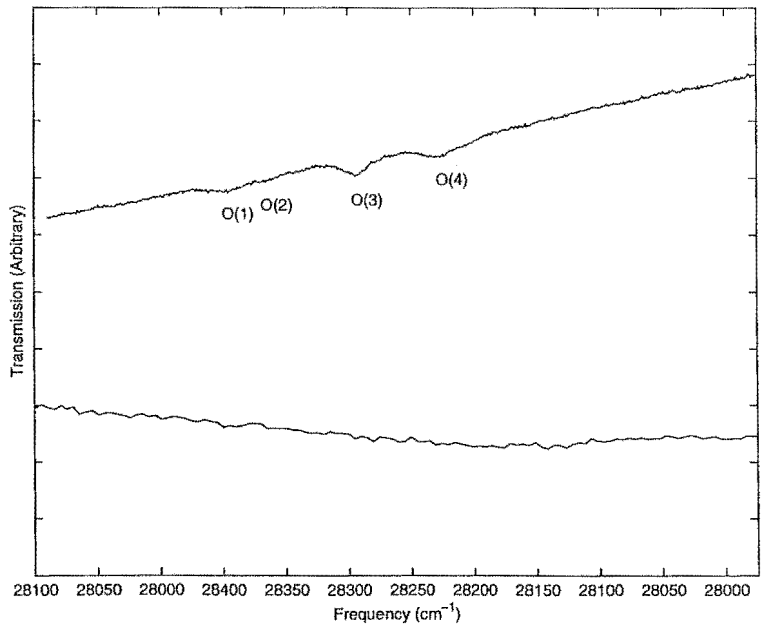

Figure 4.12: Optical absorption spectra of the $^2G_{7/2}$ (O) multiplet of K_2YF_5:(0.6%)Er^{3+} at 12K (top), and 100K (bottom).

4.2 Laser selective excitation of the $^4S_{3/2}$ multiplet

Single frequency laser excitation of K_2YF_5:Er^{3+} with the departments tunable dye laser source has yielded considerable spectroscopic information.

The $^4S_{3/2}$ multiplet of K_2YF_5:Er^{3+} (0.06%) was excited using a Coumarin 540 dye laser. The broad-band excitation spectrum of this multiplet, monitoring red emissions from the $^4F_{9/2}$ multiplet, is shown in Figure 4.13. The calibrated excitation energies have been corrected to vacuum energies and are given in Table 4.8 below.

Excitation energy (cm^{-1})	Transition assignment
18476	$Z_1 \rightarrow E_2$
18441	$Z_2 \rightarrow E_2$
18410	$Z_1 \rightarrow E_1$
18407	Site B
18402	$Z_3 \rightarrow E_2$
18374	$Z_2 \rightarrow E_1$
18336	$Z_3 \rightarrow E_1$

Table 4.8: Excitation energies for broad-band excitation of the $^4S_{3/2}$ multiplet. Transition assignments are based on absorption data. Energies are given to $\pm 1 cm^{-1}$

The strongest features of this are easily identified as resonant with the transition between the ground (Z_1) and first-excited states (Z_{2-3}) to the two energy levels of the $^4S_{3/2}$ multiplet (E_1, E_2).

The fluorescence resulting from excitation into the strong Z_2-E_2 transition at $18441 cm^{-1}$ are dominated by visible red and green emissions, from $^4F_{9/2} \rightarrow ^4I_{15/2}$ and $^4S_{3/2} \rightarrow ^4I_{15/2}$ transitions respectively. The red $^4F_{9/2}$ emissions were chosen for study, to avoid detecting the green laser radiation itself. The emission spectrum of the $^4F_{9/2} \rightarrow ^4I_{15/2}$ transition is shown in Figure 4.14. The fluorescence features characterise electronic transitions between the various crystal-field energy-levels of the $^4F_{9/2}$ multiplet, and the $^4I_{15/2}$ ground-state. At the cryogenic temperatures used, only the first two crystal-field energy levels (at $15266 cm^{-1}$ and $15316 cm^{-1}$ respectively) of the $^4F_{9/2}$ multiplet were populated. The two sets of radiative transitions D_1-Z_{1-8} and D_2-Z_{1-8} are clearly visible.

As mentioned in Section 4.1, assignment of the above fluorescence transitions implies a different ground state splitting pattern than that given in Peale *et. al.* [3]. Those workers give the Z_2, Z_3 and Z_4 levels as having very similar energies at 34, 35 and 37 cm^{-1} respectively. The results obtained in this study failed to resolve this splitting, despite

the high resolution of the SPEX 1403 monochromator used. The spacing between those transitions originating from the D_1 and D_2 levels is for the most part constant among the various terminating levels, except for the D_2-Z_7 transition which is not obvious, but is perhaps visible on the shoulder of the D_1-Z_5 peak. It is possible that previous workers have confused emissions from the secondary site examined later in this section with a multiple peak in the region of Z_2. The energies of the ground-state crystal-field levels determined in this study are given in Table 4.9.

Crystal-Field level	Energy (cm^{-1})
Z_1	0
Z_2	35
Z_3	74
Z_4	111
Z_5	283
Z_6	314
Z_7	349
Z_8	502

Table 4.9: Ground state ($^4I_{15/2}$) splitting as obtained experimentally in this study. All energies are $\pm 1 cm^{-1}$

A small feature, visible on the low-energy side of the shoulder of the Z_1-E_1 excitation line at $18410cm^{-1}$ could not be associated with the stronger lines. This feature, labelled 'B' in Figure 4.13, is suspected to belong to a second crystallographic centre. Because of the overlap with the main Z_1-E_1 transition, fluorescence resulting from excitation of the weak feature will be a combination of the emission from both sites. Figure 4.15 shows the fluorescence from laser excitation into this feature at $18402cm^{-1}$.

The two sets of $^4F_{9/2}$ emission resulting from the excitation of two different crystallographic sites can be clearly seen. The second site, labelled in Figure 4.15 as B, has spectral lines displaced slightly from those of the original site, labelled A. A narrow-band excitation spectrum monitoring the B centre feature at $14749cm^{-1}$ was recorded to distinguish the excitation energies of this second site. The spectrum obtained is shown in Figure 4.16. Because the narrow-band detection was not completely selective there is a breakthrough of A centre excitation lines, but some new excitation features due to the B centre are apparent.

The excitation transition at $18402cm^{-1}$ is clearly stronger, verifying the earlier assignment of this feature to the second site. Another smaller feature that was not evident in Figure 4.13 is at $18437cm^{-1}$ on the high energy shoulder of the Z_2-E_2 excitation. Another

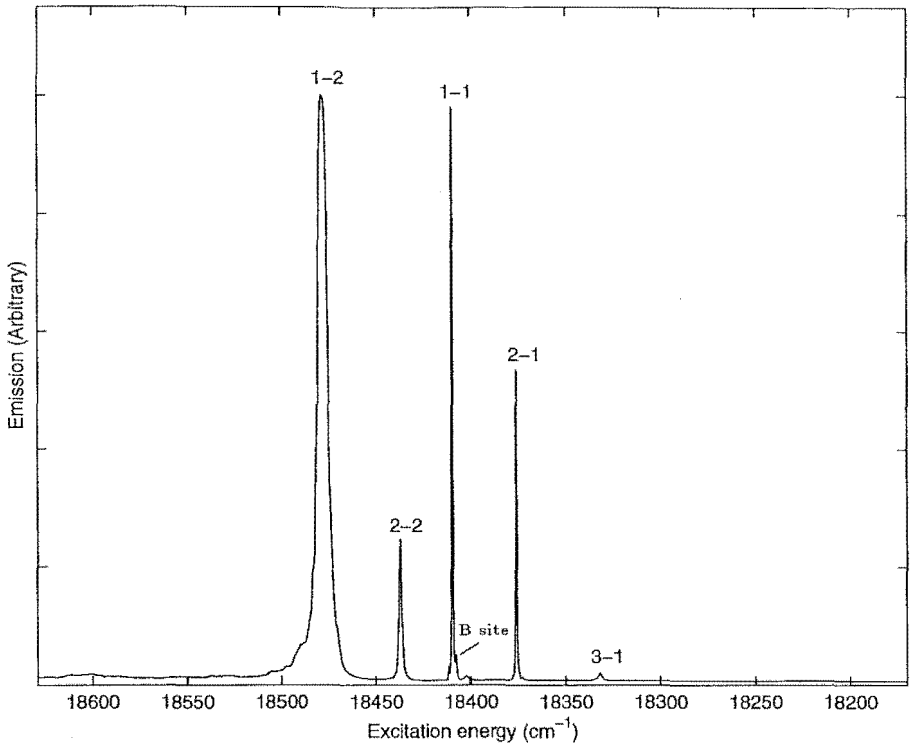

Figure 4.13: 12K Broad-band excitation spectrum of the $^4S_{3/2}$ multiplet, monitoring red (660nm) fluorescence. Resonant transitions Z_m - Y_n are labelled m-n for brevity.

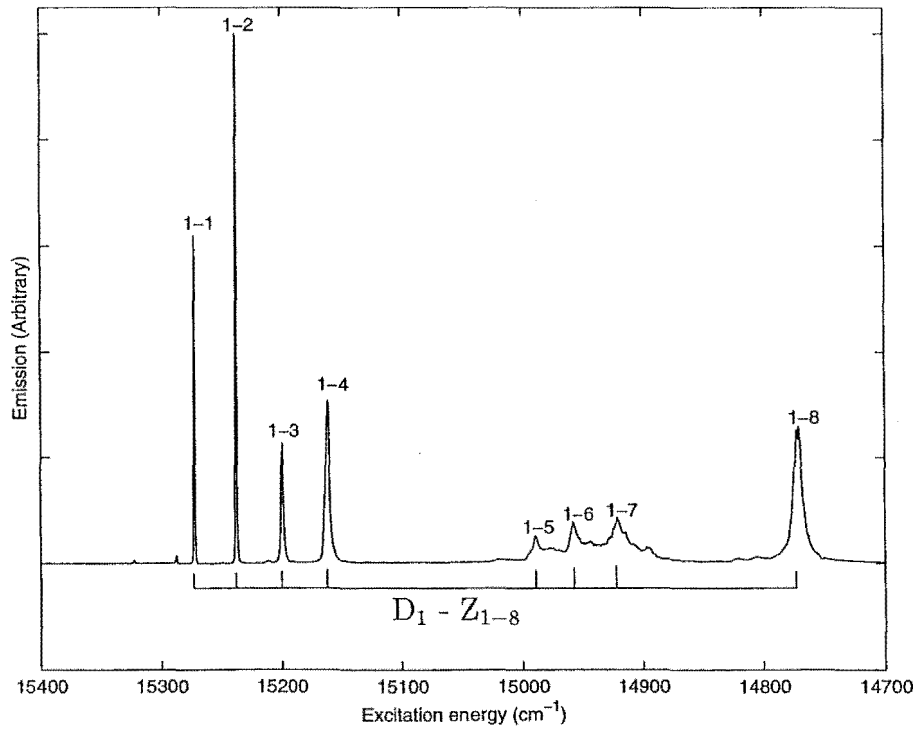

Figure 4.14: 12K $^4F_{9/2}$ $\rightarrow$$^4I_{15/2}$ fluorescence emission from excitation into the Z_1 - E_1 excitation transition. Resonant transitions D_m - Z_n are labelled m-n for brevity.

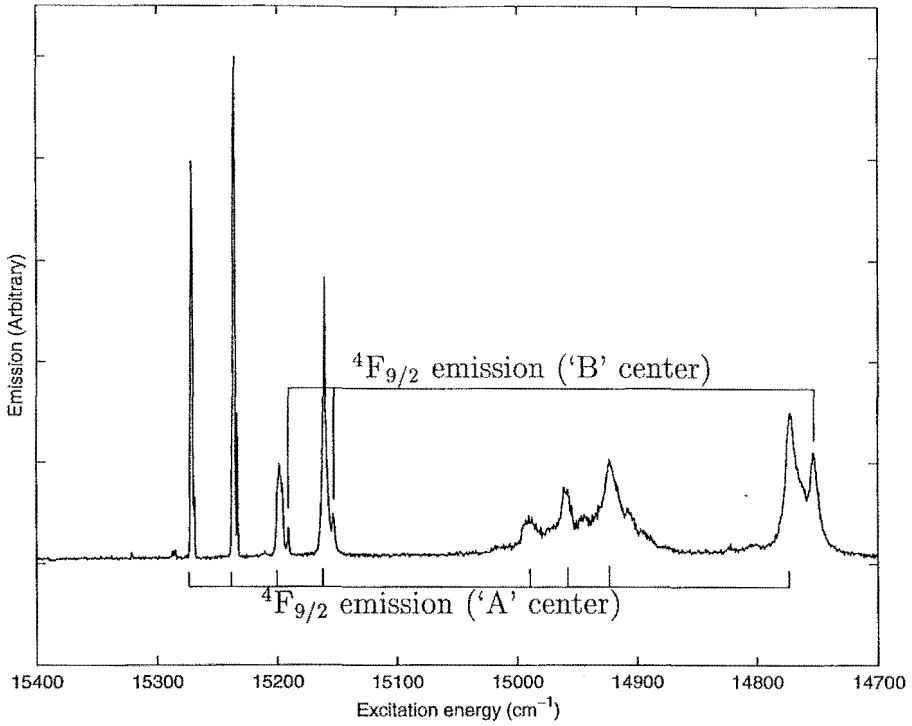

Figure 4.15: 12K Fluorescence from excitation at 18407cm^{-1} . Transitions are given where possible based on absorption data. Crystallographic centers are labelled.

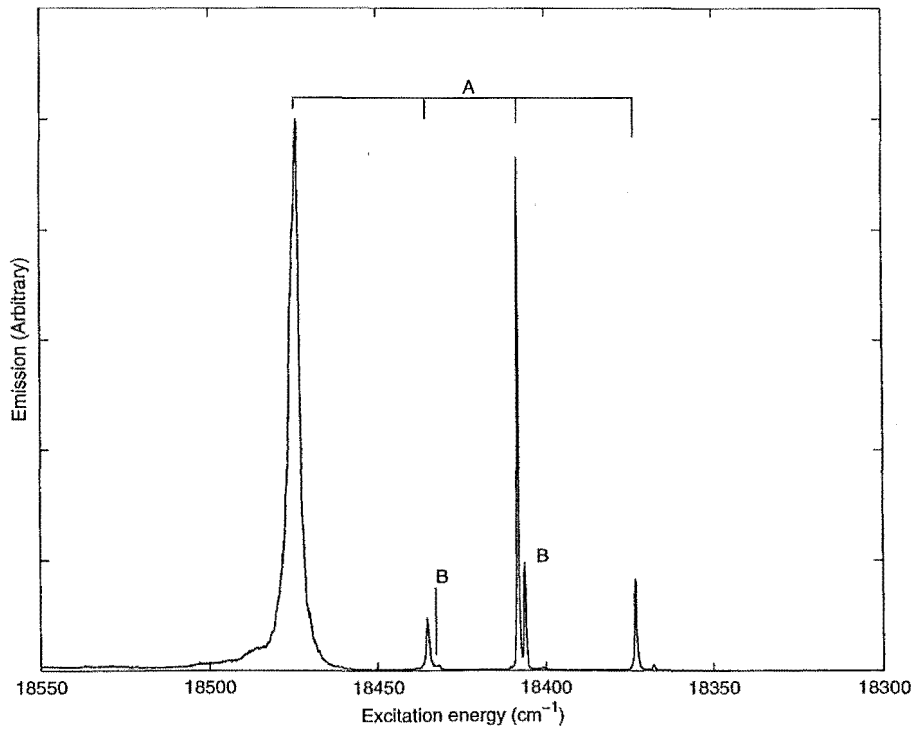

Figure 4.16: 12K Narrow-band excitation of the $^4S_{3/2}$ multiplet monitoring the 14749cm^{-1} B center transition. Excitation features are labelled by center assignment.

weak line appears alongside the Z_2-E_1 transition at 18368cm^{-1} . It is also possible that a similar 'B' feature is obscured by the broad Z_1-E_2 excitation. Table 4.10 lists the emission and excitation energies observed for the site B.

$^4F_{9/2} \rightarrow ^4I_{15/2}$ emission	Transition	Emission energy (cm^{-1})
	D_1-Z_1	15264
	D_1-Z_2	15229
	D_1-Z_3	15186
	D_1-Z_4	15149
	D_1-Z_8	14749
$^4I_{15/2} \rightarrow ^4S_{3/2}$ excitation	Transition	Excitation energy (cm^{-1})
	Z_2-E_2	18402
	Z_1-E_1	18437
	Z_2-E_1	18368

Table 4.10: Emission and excitation energies for the B site of K_2YF_5:Er^{3+} . All energies are $\pm$1cm^{-1}

The spectral lines of the second site described above differ from those of the primary site by only a few wave-numbers in most places. The transitions are labelled therefore, by the transitions of the primary site from which they are offset. The closely correlated energy levels must indicate a very similar crystal-field in the two cases. The two ions Y^{3+} and Er^{3+} are of similar ionic radii [5], and equal electrostatic charge. In this situation a dopant ion in a pairing with another in the linear chain host would experience only a subtly different crystal field distortion to an ion in an isolated position. This would produce two crystallographic sites with relatively similar crystal-field energy levels.

4.3 Fluorescence lifetime measurements for $K_2YF_5:Er^{3+}$

Fluorescence transients were recorded for various multiplets using the nitrogen-pumped dye laser system. Initial difficulties with Coumarin 540A dye, resulted in the use of a Coumarin 500 dye, to excite the $^2H_{11/2}$ multiplet. This multiplet does not display emission, instead decaying via multiphonon processes to the $^4S_{3/2}$ multiplet. The time-resolved emissions were recorded for the $^4S_{3/2}$, $^4F_{9/2}$, and $^4I_{9/2}$ multiplets. The pumping scheme used is shown in Figure 4.17

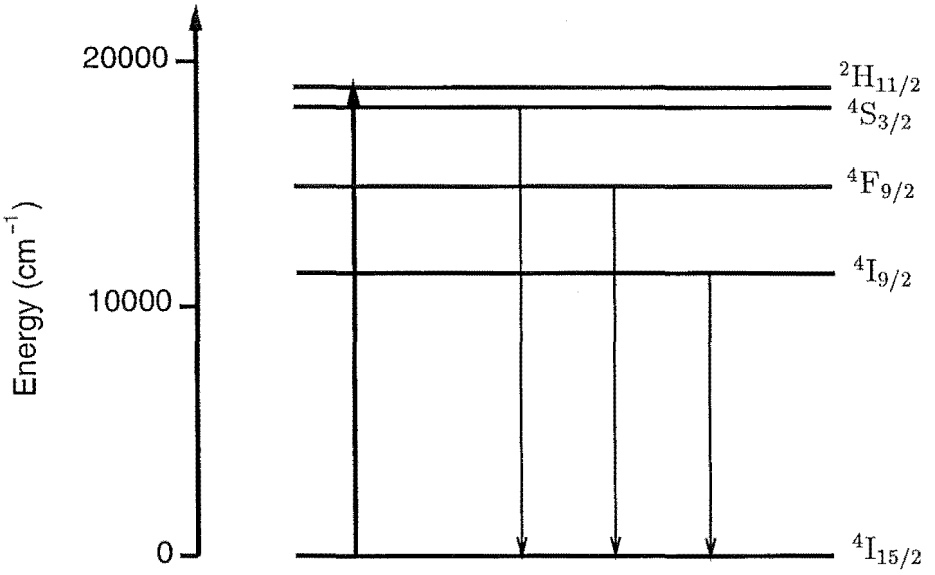

Figure 4.17: Pulsed excitation scheme for the measurement of multiplet lifetimes of $K_2YF_5:Er^{3+}$

Due to the low signal obtained from the infrared photomultiplier used in the detection of the emission transients, the results for the $^4I_{9/2}$ multiplet are somewhat less precise than the others.

The resulting emission transients for each multiplet were fitted by computer routine to a single or in the case of a distinct risetime, to a double exponential. The lifetimes for the $^4S_{3/2}$ and $^4F_{9/2}$ multiplets were also recorded at an increased temperature of 100K, and the $^4S_{3/2}$ multiplet at 300K. As the entire intensity scale of the transient was digitised into one byte of stored information, the fits were weighted towards the short-time/high-signal end to avoid significant digitisation error.

Figures 4.18 and 4.19 show the recorded emission transients for the $^4S_{3/2} \rightarrow ^4I_{15/2}$ and $^4F_{9/2} \rightarrow ^4I_{15/2}$ fluorescence transitions. The figures are plotted with a natural-logarithm scale to more easily show the exponential nature of the decay.

The emission transient from the $^4S_{3/2}$ multiplet shows no rise time, confirming the

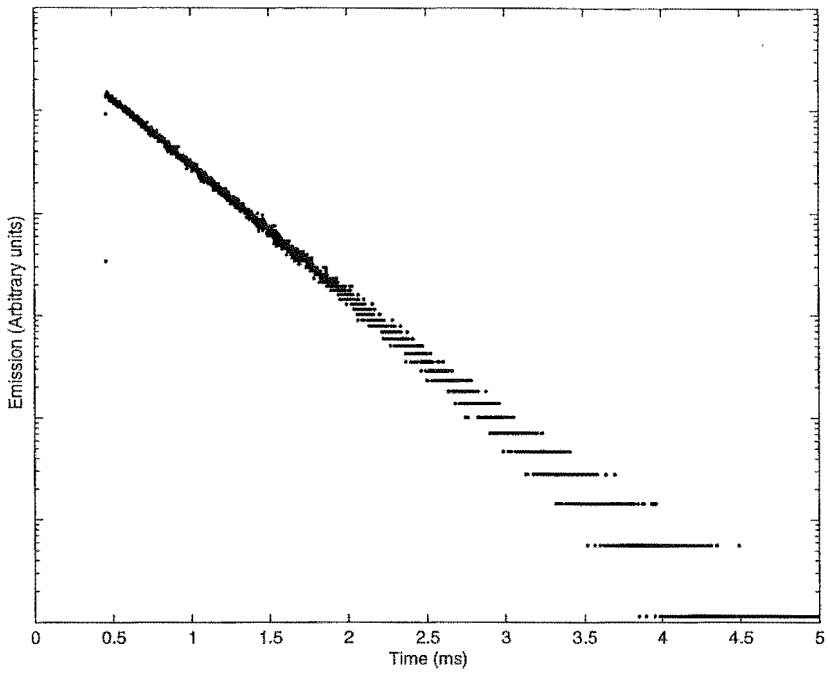

Figure 4.18: Transient recorded for $^4S_{3/2}$ emission after pulsed excitation into the $^2H_{11/2}$ multiplet. The temperature of the sample was 12K.

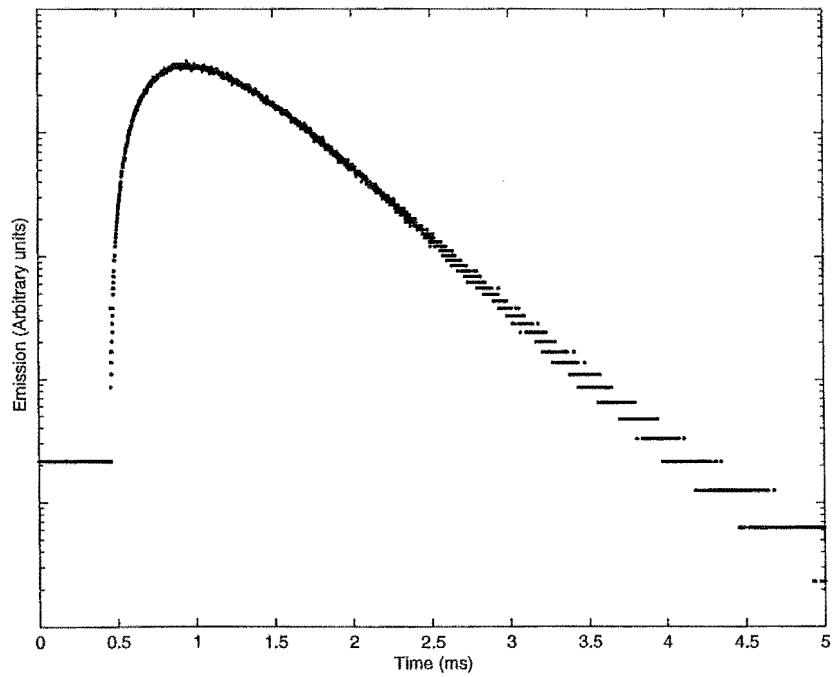

Figure 4.19: Transient recorded for $^4F_{9/2}$ emission after pulsed excitation into the $^2H_{11/2}$ multiplet. The temperature of the sample was 12K.

rapid non-radiative decay from the excited $^2H_{11/2}$ multiplet. The rate-equation for the population of the emitting level is given by a simple source-less differential equation of the form

$$\frac{dN}{dt} = -\frac{1}{\tau}N,$$

which is easily solved, giving the exponential decay

$$N(t) = N(0)e^{-\frac{t}{\tau}}$$

The $^4S_{3/2} \rightarrow ^4I_{15/2}$ emissions are therefore fitted to an exponential of this form, yielding the fluorescence lifetimes τ.

For the $^4F_{9/2}$ multiplet, a significant risetime to the fluorescence transient is observed as population feeds down from the higher multiplets. Non-radiative decays, such as those due to multiphonon decay, are in general considerably more rapid than those due to radiative processes. In a system where a rise-time is evident, it is usually assumed that the rise-time is due to a radiative transition originating from a higher energy multiplet. The time-constant of such a rise should correspond to that for the decay of the higher 'feeding' multiplet.

The differential rate-equations for the population of such a system should take into account the branching rule from the upper 'feeding' state (u). Specifically, the decay rate from the upper state ($\frac{1}{\tau_u}$) is not necessarily equal to the increase in population of the emitting level (e) due to upper-to-emitting decay ($\frac{1}{\tau_{u-e}}$). The rate equations are

$$\begin{aligned}\frac{dN_u}{dt} &= -(\frac{1}{\tau_{u-e}} + \frac{1}{\tau_{u-other}})N_u \\ \frac{dN_e}{dt} &= +\frac{1}{\tau_{u-e}}N_u - \frac{1}{\tau_e}N_e.\end{aligned}$$

This more complicated set of equations has as it's solution the following double exponential expression,

$$N_e = A(e^{-(\frac{t}{\tau_e})} - e^{-(\frac{t}{\tau_{u-e}})}).$$

Where both the lifetime of the emitting level (τ_e), and of the source level (τ_u) are represented, and the A parameter, determined experimentally in this case, involves the

constants $\frac{1}{\tau_{u-e}}$ and $\frac{1}{\tau_{u-other}}$. An additional parameter was also required in the fitting stage, to account for the voltage offset in the measuring equipment. This 'baseline' has been removed for the purposes of plotting the intensity on a logarithmic scale, in which the basic exponential relation is represented by a straight line.

The fitting routine used the 4th/5th Runge-Kutta method to fit the three or four parameters to the data. In such an analysis, it is important to gauge the accuracy of the parameters obtained. The standard deviation, σ, in the parameter p_i for a sample size of m, and the total number of parameters n is given by

$$\sigma(p_i)^2 = \left(\frac{E'E}{m-n}\right)[(A'A)^{-1}]_{ii},$$

The term E is the vector of errors between calculated and experimental data, and A_{ij} is a matrix of partial derivative values,

$$A_{ij} = \frac{\partial y_i}{\partial p_j}$$

where y_i is the i_{th} experimental data point [12]. This expression for the standard deviation was used to determine the uncertainty in each single and double exponential fit.

Figures 4.20-4.23 present the remainder of the recorded transients fitted using the above methods. For Figures 4.19 and 4.22 the risetimes were found to exactly correlate to the fluorescence lifetime of the $^4S_{3/2}$ multiplet, confirming the double exponential model. Table 4.11 presents the various fluorescence lifetimes obtained, contrasted with those of Peale *et al* for the fully-doped material K_2ErF_5[3].

A striking feature of these results is the marked increase in the lifetime of the $^4S_{3/2}$ multiplet in the low dopant concentrations used here. This increased lifetime is also evident for the same multiplet at room temperature. The crystal structure is such that no large distortions are produced by the substitution of Er^{3+} ions for Y^{3+} in the lattice and hence no drastic change to the crystal field conditions should occur. Most likely the reduced lifetime in the highly doped material is due to concentration quenching of the emission by energy-transfer/migration between neighbouring Er^{3+} ions.

Results have been included in Table 4.11 for multiplets that were not studied in this thesis. These results have proved useful reference for discussions in later chapters. Comparing the results of this study with those of Peale *et al* , it would seem reasonable to predict that the multiplet lifetimes in $K_2YF_5:Er^{3+}$ decrease with increased concentration.

Emitting Multiplet	This Study 12K	100K	300K	Peale *et al* 80K	300K
$^4S_{3/2}$	800±10	750±50	490±8	70	2
$^4F_{9/2}$	330±2	330±24	-	230	-
$^4I_{9/2}$	810±12	-	-	-	-
$^4I_{11/2}$	-	-	-	200/1500*	230
$^4I_{13/2}$	-	-	-	1070	766

Table 4.11: Photoluminescent lifetimes in microseconds (μs) for various multiplets of $K_2YF_5:Er^{3+}$ (this study) and K_2ErF_5 (Peale *et al* [3]). Lifetimes are shown for several temperatures. The result by Peale *et al* marked * was observed to have a double exponential decay.

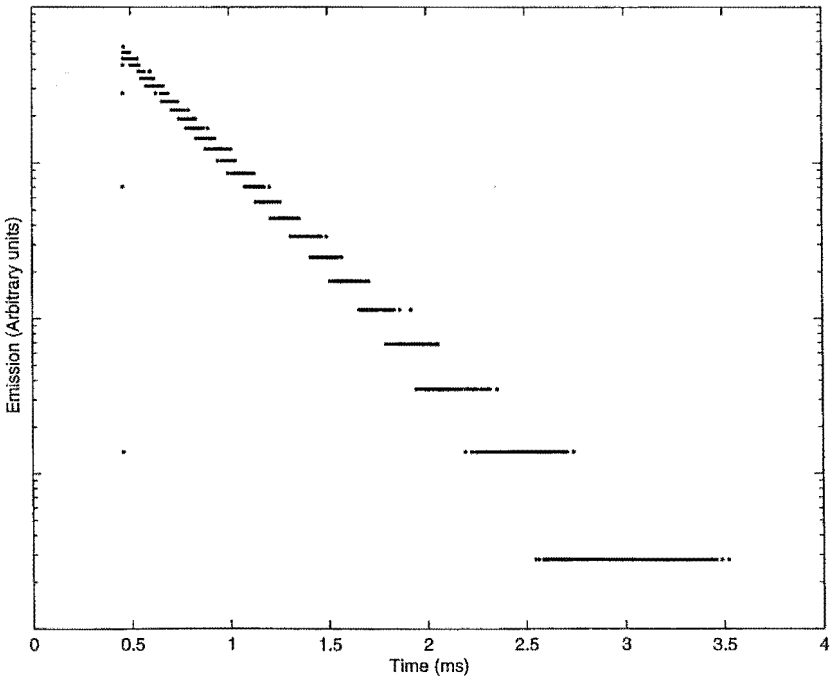

Figure 4.20: Transient recorded for $^4I_{9/2}$ emission after pulsed excitation into the $^2H_{11/2}$ multiplet. The temperature of the sample was 12K.

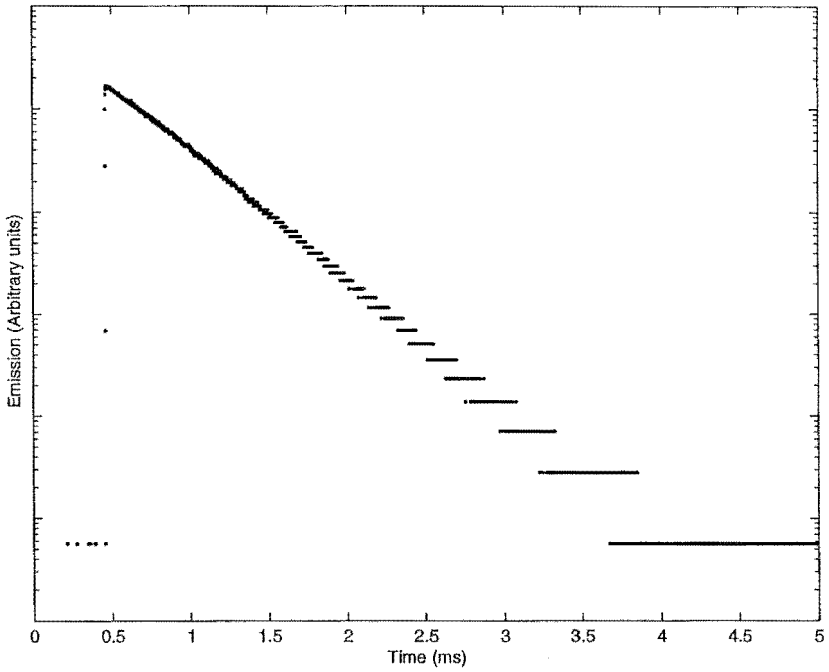

Figure 4.21: Transient recorded for $^4S_{3/2}$ emission after pulsed excitation into the $^2H_{11/2}$ multiplet. The temperature of the sample was 100K.

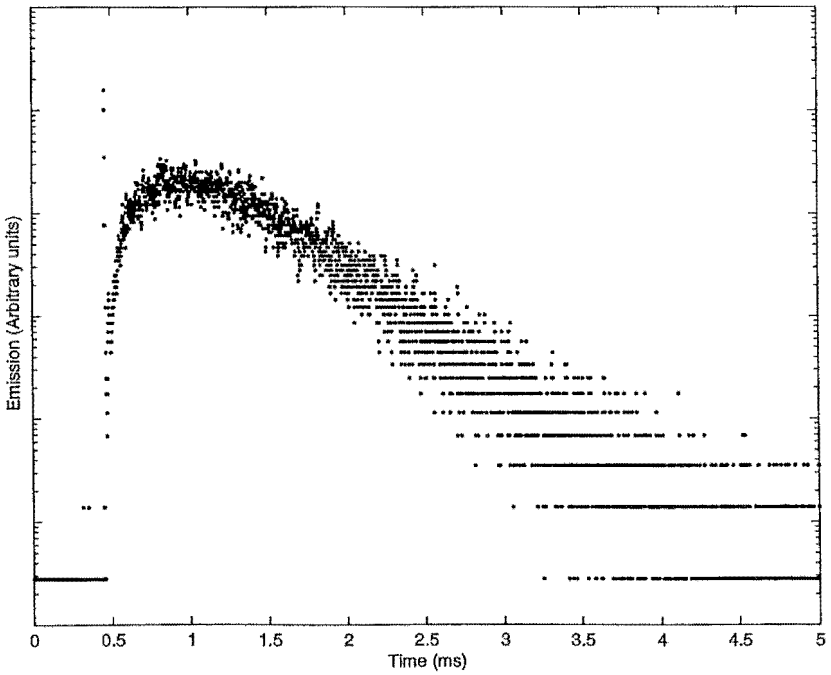

Figure 4.22: Transient recorded for $^4F_{9/2}$ emission after pulsed excitation into the $^2H_{11/2}$ multiplet. The temperature of the sample was 100K.

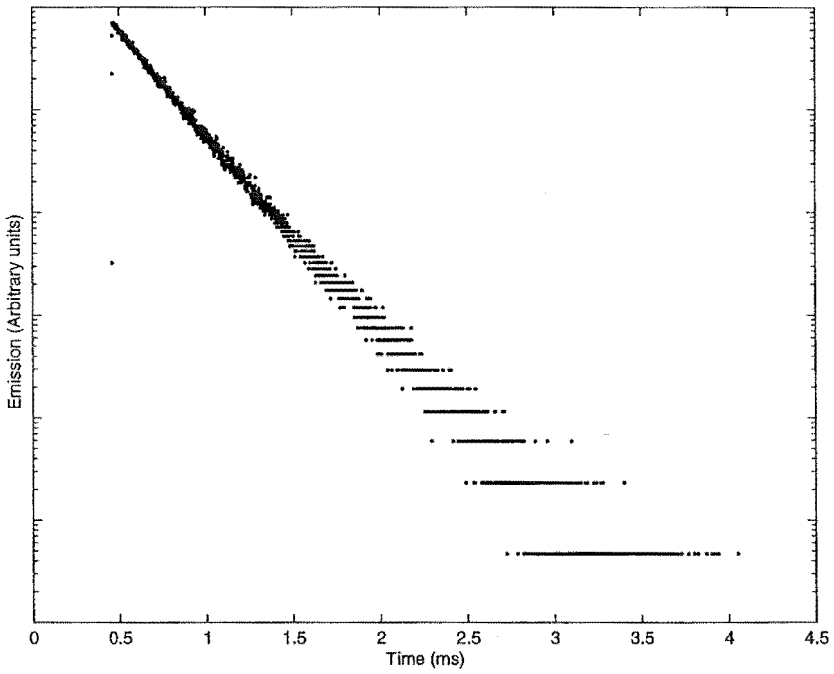

Figure 4.23: Transient recorded for $^4S_{3/2}$ emission after pulsed excitation into the $^2H_{11/2}$ multiplet. The temperature of the sample was 300K.

4.4 Crystal field analysis for $K_2YF_5:Er^{3+}$

Peale *et al* [3] have performed a crystal-field analysis of the dominant Er^{3+} centre in K_2YF_5, assuming a trigonal C_{3V} symmetry for that site. Although the point-group C_{3V} is not a sub-group of the host crystal symmetry D_{2h}, the positions of the F^- ions in each $[YF_5]^{2-}$ structure are approximately trigonal about the yttrium ion. 26 crystal-field energy levels were used, completely representing the multiplets $^4I_{15/2}$ to $^4F_{7/2}$ inclusive. However, an inconclusive fit was reported, with a standard deviation of $25cm^{-1}$ from the experimental values. Those workers postulated structural differences between the hydrothermally grown K_2YF_5 and those previously published as being responsible.

Considering the extended absorption data presented in this study, and the differing ground-state splitting obtained, a further attempt has been made to fit a C_{3V} crystal-field Hamiltonian to the experimental energy levels. Dr. Mike Reid [13] has written several useful computer routines that have automated the complex task of constructing the free-ion wave-functions, then fitting the crystal-field parameters to the experimental energy levels. The initial free-ion wave-functions were calculated from parameters given for the Er^{3+} ion by Carnall *et al* [1].

The free-ion parameters in Table 4.12 are the coefficients of the inter-configurational interaction (α, β, and γ), the spin-orbit parameter (ζ), and the radial integrals of each of the electrostatic, magnetic and many-body electrostatically correlated magnetic terms (F^k, M^k, P^k, and T^k respectively). Note that the magnetic and two-body terms (M^k and P^k) can each be shown to observe a constant ratio, and are fitted in terms of the total value.

The accuracy of a fitting process can rely heavily upon the initial values of the parameters. The quantity that is minimised here is in this case the sum of the squared differences of the experimental crystal-field level energies, and those calculated. It is possible that a set of parameters with this quantity minimised is completely non-physical. Care must therefore be taken to provide reasonable starting parameters.

Free-ion parameter	Value (cm^{-1})
F^2	100274
F^4	70555
F^6	49900
α	17.88
β	-599
γ	1719
T^2	-441
T^3	-42
T^4	-64
T^6	314
T^7	-387
T^8	-363
ζ	-2381
M_{TOT}	4.58
P_{TOT}	852

Table 4.12: Parameters of the free-ion Hamiltonian for Er^{3+} as given for Er^{3+} in LaF_3 by Carnall *et al* [1].

The trigonal C_{3V} symmetry Hamiltonian used for the least-squares fit to the experimental data is given by

$$\begin{aligned} H_{C_{3V}} &= B_0^2 C_0^{(2)} + B_{cubic}^4 \left[C_0^{(4)} + \sqrt{\frac{10}{7}} (C_3^{(4)} - C_{-3}^{(4)}) \right] + B_{trig}^4 \left[C_0^{(4)} - \frac{1}{2}\sqrt{\frac{7}{10}} (C_3^{(4)} - C_{-3}^{(4)}) \right] \\ &+ B_{cubic}^6 \left[C_0^{(6)} - \frac{1}{4}\sqrt{\frac{35}{6}} (C_3^{(6)} - C_{-3}^{(6)}) + \frac{1}{8}\sqrt{\frac{77}{3}} (C_6^{(6)} - C_{-6}^{(6)}) \right] \\ &+ B_{trig}^6 \left[C_0^{(6)} + \frac{4}{7}\sqrt{\frac{10}{21}} (C_3^{(6)} - C_{-3}^{(6)}) + \frac{4}{7}\sqrt{\frac{11}{21}} (C_6^{(6)} - C_{-6}^{(6)}) \right] \\ &+ \hat{B}_{trig}^6 \left[\sqrt{\frac{11}{42}} (C_3^{(6)} - C_{-3}^{(6)}) + \sqrt{\frac{5}{21}} (C_6^{(6)} - C_{-6}^{(6)}) \right]. \end{aligned}$$

The exact combinations of the tensor operators, $C_q^{(k)}$, here are the invariant scalars in the point group symmetry reduction $SO_3 \rightarrow O \rightarrow D_3 \rightarrow C_3$. [14]

A good starting value of the parameter B_0^2 can be obtained from the splitting of the $J=^3/_2$ multiplets. The expression for the matrix elements of the perturbation Hamiltonian $H_{C_{3V}}$ is [8]

$$\begin{aligned}\langle l^n\alpha SLJJ_z|\, H_{C_{3V}}\, |l^n\alpha' SL'J'J'_z\rangle &= \sum_{k,q} B_q^k \left\langle l||C^{(k)}||l\right\rangle \times (-1)^{J-J_z} \begin{pmatrix} J & k & J' \\ -J_z & q & J'_z \end{pmatrix} \\ &\times (-1)^{S+L'+J+k}\sqrt{(2J+1)(2J'+1)} \times \begin{Bmatrix} J & J' & k \\ L' & L & S \end{Bmatrix} \\ &\times \left\langle l^n\alpha SL||U^{(k)}||l^n\alpha SL'\right\rangle .\end{aligned}$$

From the triangle conditions for the 6-j symbols, it is clear that for a multiplet with $J{=}^3/_2$, k must be less than 3, which leaves only the term $B_0^2C_0^{(2)}$ in the expression for the crystal-field Hamiltonian. The evaluation of the matrix elements of the Hamiltonian is further complicated by the crystal-field mixing that will occur between each state with equal J. The free-ion wave-function previously calculated for the $^4S_{3/2}$ multiplet was

$$\begin{aligned}\left|^4S_{3/2}\right\rangle &= 0.8278\left|^4S_{3/2}\right\rangle + 0.0436\left|^4D_{3/2}\right\rangle + 0.2224\left|^4F_{3/2}\right\rangle \\ &- 0.4324\left|^2P_{3/2}\right\rangle - 0.2207\left|^2D^{(1)}_{3/2}\right\rangle - 0.0241\left|^2D^{(2)}_{3/2}\right\rangle .\end{aligned}$$

Due to this mixing between the $J{=}^3/_2$ states, the matrix elements for $C_0^{(2)}$ become the sum of all possible αSL combinations. The $\left\langle l^n\alpha SL||U^{(k)}||l^n\alpha SL'\right\rangle$ terms and 3-j and 6-j symbols are tabulated in books such those by Nielson and Koster [15], and Rotenberg *et al* [16], whilst the remaining terms can be evaluated using methods from Wybourne [8]. The splitting of the only two levels of this multiplet due to the crystal-field perturbation, will be equal to the product of the crystal-field parameter B_0^2 and the matrix element of $C_0^{(2)}$ which has been evaluated. The value obtained in this way for the parameter B_0^2 was 660cm^{-1} .

Reasonable starting values for the remaining B_q^k parameters were obtained from comparisons with results from other host systems, and careful observation of the way they varied as the fit proceeded.

The optimised crystal-field parameters obtained from the fit are listed in Table 4.13. This is clearly a better fit than was previously obtained as the standard deviation has decreased to 18cm^{-1} , even though more crystal-field levels were included. The number of data points that were fitted to this accuracy, given the *ab initio* nature of the fit itself, is a somewhat positive indication of the usefulness of the trigonal approximation.

Crystal-field parameter	Fitted value (cm^{-1})
F^2	99412
F^4	70377
F^6	49437
ζ	-2372.3
B_0^2	-661
B_{cubic}^4	659
B_{cubic}^6	-228.6
B_{trig}^4	-1556
B_{trig}^6	-3.6
$\hat{B}_{trig}^6$	-482.9
No. of Parameters	10
No. of Data points	56
Standard Deviation (cm^{-1})	17.6

Table 4.13: Fitted parameters of the Crystal-Field Hamiltonian for $K_2YF_5:Er^{3+}$

A better procedure would take account of the symmetries of the calculated wavefunctions, matched to that obtained from polarisation data from properly oriented samples. The nature of the crystals used in this study was such that polarisation spectroscopy was not attempted, and only the spectral position of the wavefunction was considered. This is a limiting factor upon the accuracy of the obtained fit.

Chapter 5

Upconversion processes in erbium-doped K_2YF_5

Upconverted fluorescence emission from K_2YF_5:Er^{3+} has been observed for various laser excitation energies. The following chapter details the spectroscopy and sets out the mechanisms involved in these previously unreported processes.

5.1 Upconversion mechanisms

An upconversion process is one where light emission is produced from excited ions, at higher energies (smaller wavelengths) than the source of excitation. In general it can be said that the energies of two or more photons are combined to provide excitation beyond that of the single photon energy. There are a number of recognised and well-studied mechanisms to provide for this. This section introduces some of the common upconversion mechanisms, and those relevant to the following study of K_2YF_5:Er^{3+} . A good overview of the field can also be found in *Up-conversion and Excited State Energy Transfer in Rare-Earth Doped Materials.* [17]

Sequential absorption upconversion

Sequential Absorption Upconversion (S.A.U.) is a process whereby a single ion absorbs both photons in succession. The initial excitation excites the ion into a metastable excited state, where a second, or excited-state absorption can occur. This process is shown in Figure 5.1

Depending on the energy level scheme of the ion, and the multiplet lifetimes, it is also common (see later work on $^4I_{11/2}$ upconversion excitation) for the ion to decay to a lower energy state, which acts as the metastable state.

Upconversion of this type can be easily achieved with two different pump lasers, one tuned to the frequency of the first, or ground-state absorption transition (1-2' on Figure 5.1) , the other to that of the second, or excited-state absorption (2-3 on the same

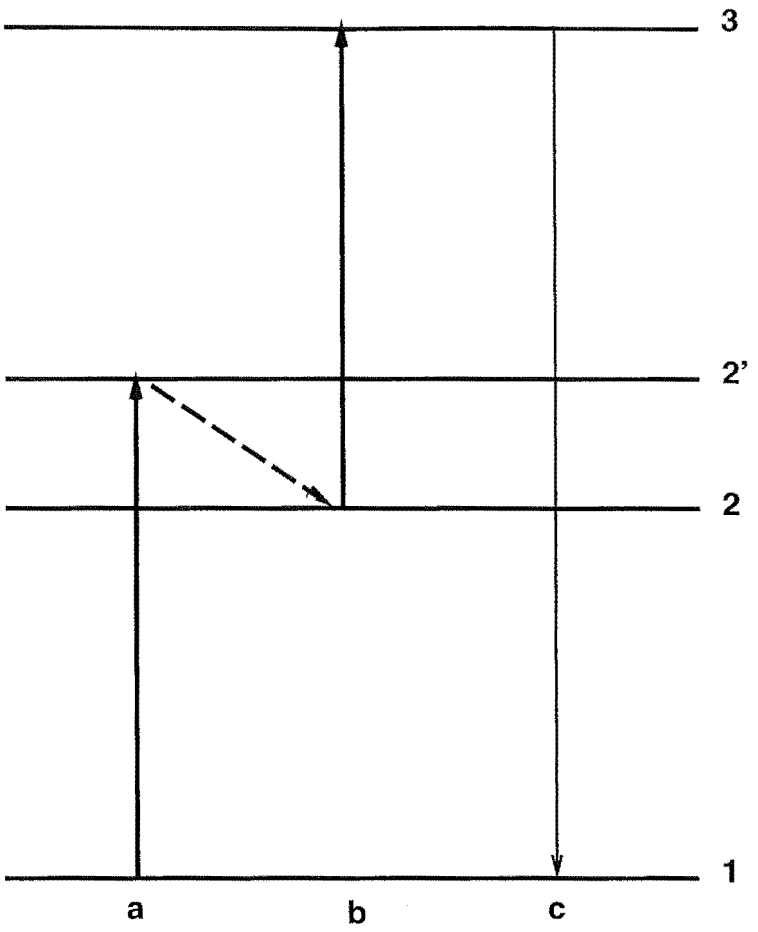

Figure 5.1: The Sequential Absorption Upconversion process. (a) The initial absorption provides excitation 1→2'. The ion may then decay via phonon emission into a metastable state 2, or in some situations, this condition is met by the initially excited state 2'. (b) The second, or excited-state absorption. (c) Upconversion emission from the excited state 3.

figure). Several workers have used various schemes of this type to demonstrate sequential-absorption upconversion for rare-earths in various hosts, and in some cases even made an upconversion laser.

Another common approach is to use a single laser source to provide both ground- and excited-state excitations. Excepting the rare occasion where both transitions require the same excitation energy, one transition will have a larger excitation energy than the other and the laser will be resonant with a single transition. Both excitations can still proceed however. A transition with energy higher than resonance will occur via the release of lattice phonons, provided the energy 'mismatch' falls within the vibrational spectrum of the host material. And similarly, provided an energy shortfall is within the thermally occupied energies of the vibrational spectrum, then excitation below resonant energy will also occur. The second process however, will be considerably weaker than the first and

will be (obviously) temperature dependant.

Energy transfer upconversion

Upconversion by energy-transfer involves at least two optically active ions. Each is excited by the absorption of photons, with one 'donor' ion transferring all or part of its energy non-radiatively to the second 'acceptor'. Figure 5.2 shows a common example of energy-transfer upconversion, where the two ions in question are identical, and a cross-relaxation pathway exists whereby the energy of an exciting transition on the second ion is resonant with a downward transition on the first.

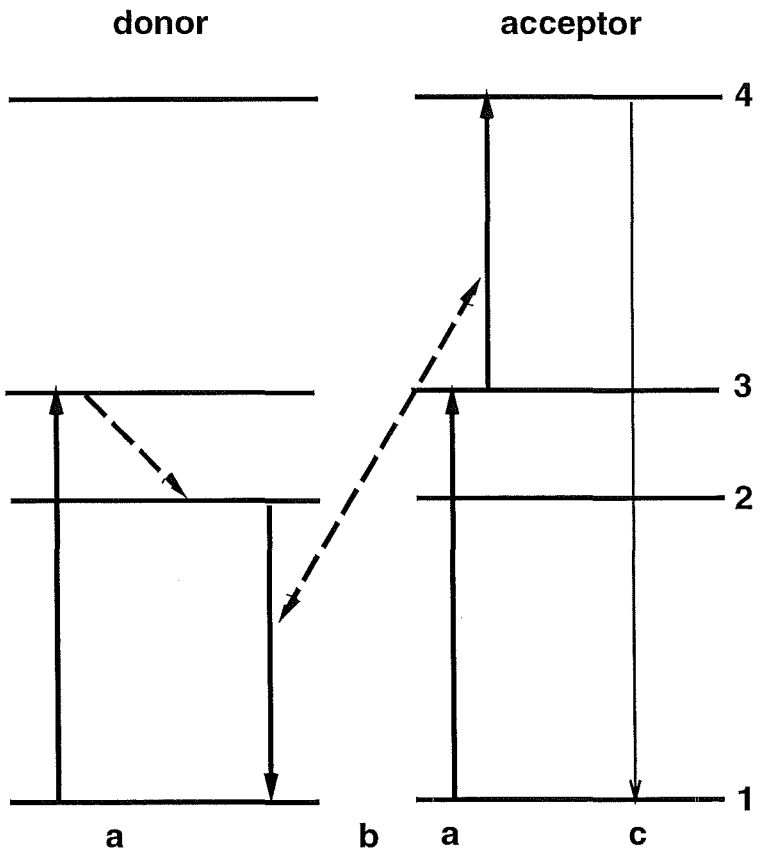

Figure 5.2: An example of the energy-transfer upconversion process. (a) Initially, both ions are excited into the state 3, whereupon the donor ion undergoes a decay to the lower energy state 2. (b) The donor ion decays (2-3), by means of an transfer of energy to the acceptor ion, exciting that ion into the higher state 4. (c) Upconversion emission (4-1).

Although this energy transfer happens predominantly through the mechanism of cross-relaxation, it is also possible for the excitation energy to migrate through the lattice as an exciton before the energy is transferred. [17].

It is common to find such cross-relaxations in the behaviour of cluster centres, although high concentrations of single, active ions will produce the same effect. It should be noted that these processes, and the conditions under which they occur, are identical to those for 'fluorescence quenching', where higher energy emissions are reduced in favour of a cross-relaxation to lower energy levels.

Photon avalanche upconversion

Photon avalanche, although different in characterisation than the previous mechanisms, should perhaps be considered as a combination of the two. In this process an initially upconverted ion (by either sequential absorption or energy transfer), undergoes a cross-relaxation that simultaneously excites a second ion from the ground state to the state from which the sequential absorption can occur. The terminating level of the first ion is the same state as the first. In this way, a single ion in the upconverted state produces two ions in the state from which excited-state absorption to the upconverted state can occur.

This geometric series build-up in the population of the upper state provides a greater absorption of a laser source tuned resonant to that excited state absorption. Figure 5.3 demonstrates the photon avalanche process as it applies to two identical ions.

The photon avalanche effect is characterised by a minimum power threshold necessary to sufficiently populate the first-excited state, so as to be sure of this build-up. Other evidence has recently been presented regarding the temporal profiles of fluorescence emissions, and laser transmission through the sample, in the region of the threshold power [18].

Other mechanisms

Wright [17] describes several more classes of upconversion mechanism. Most of these can be considered as combinations involving a few basic features, such as excited state absorption, and energy-transfer, whether it be direct ion-ion transfer, energy migration, or even radiative transfer. In any complex spectroscopic system involving excited proximate ions, there is also the possibility that more than one such competing process is present.

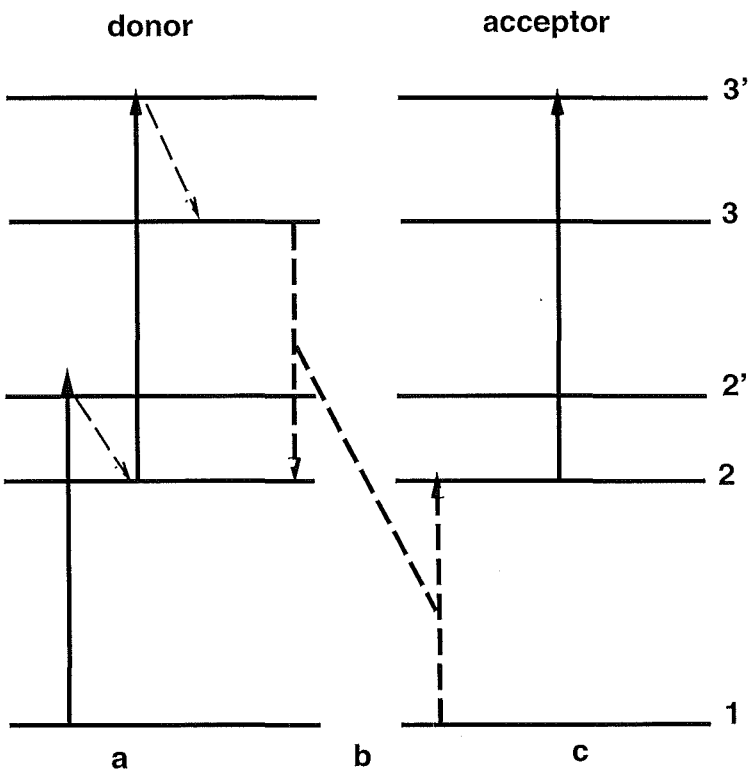

Figure 5.3: Photon avalanche upconversion between two identical ions. (a) An initial sequential-absorption upconversion with the laser resonant with the excited-state absorption. (b) the excited donor ion decays to the state 2, via an energy-transfer with the acceptor ion, which is excited also into state 2. (c) two ions are now in state 2, resonant with the laser excitation.

5.2 Visible upconversion from infrared excitation into the $^4I_{11/2}$ multiplet

The $^4I_{11/2}$, or A multiplet of Er^{3+} has absorption transitions in the range 10200-10400cm^{-1} , well within the range of the long-wavelength optics set for the titanium-sapphire ring laser. A sample of K_2YF_5 with a nominal Er^{3+} concentration of 0.6% was cooled to 12K using the methods described in Section 3.2. Upon excitation, the sample was seen to emit dominantly in green wavelengths, even in the initial off-resonance configuration. Figure 5.4 shows the broad-band emission at green (540nm) wavelengths as a function of laser excitation energy.

A comparison with the optical absorption spectra immediately shows the excitation spectrum of green upconversion contains more spectral lines than can be accounted for from simple $^4I_{15/2} \rightarrow ^4I_{11/2}$ absorption. Correlation with the spectral data show that these extra features are due to the excited state absorption transition $^4I_{11/2} \rightarrow ^4F_{7/2}$.

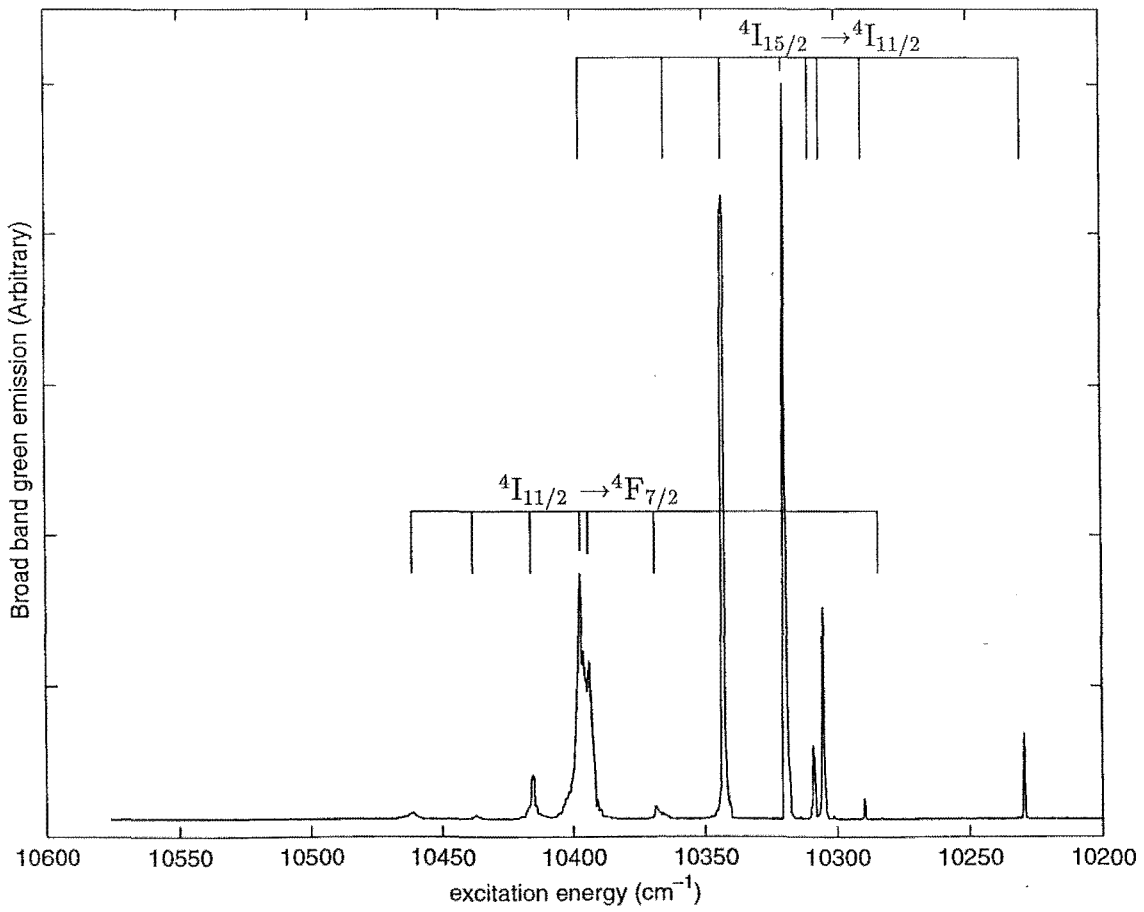

Figure 5.4: 12K Broad-band green emission at around 540nm as a function of excitation energy. The resonant transitions are labelled.

In order to determine the number of different sites that are involved in this upconversion emission, the laser selective excitation technique was employed. Initially the green fluorescence at around 545nm was located. The emission spectra obtained for a laser excitation energy of 10316cm^{-1} is shown in Figure 5.5. The fluorescence peaks clearly characterise emissions originating from the two levels of the upper $^4S_{3/2}$ (E) state, and terminating on the various $^4I_{15/2}$ crystal field levels. Knowledge of the ground-state crystal-field level splitting enable these emission features to be classified with the assignments given in Table 5.2.

Transition energy (cm^{-1})	Transition assignment
18476	E_2-Z_1
18442	E_2-Z_2
18411	E_1-Z_1
18403	E_2-Z_3
18377	E_1-Z_2
18366	E_2-Z_4
18338	E_1-Z_3
18300	E_1-Z_4
18193	E_2-Z_5
18162	E_2-Z_6
18128	E_1-Z_5
18097	E_1-Z_6
18062	E_1-Z_7
17975	E_2-Z_8
17910	E_1-Z_8

Table 5.1: $^4S_{3/2} \rightarrow {}^4I_{15/2}$ upconverted fluorescence from excitation into the $^4I_{11/2}$ multiplet. The transition assignments are given, based on absorption data. Energies are given to $\pm$1cm^{-1} .

A narrow-band excitation scan was performed on the strong and isolated E_1-Z_3 transition at 18338cm^{-1} . The excitation spectrum obtained (Figure 5.6) does not differ significantly from that recorded when detecting broad-band green emission. Thus it is concluded that the upconversion behaviour has its origin in a single site and further, from the close correlation with absorption results, it is clear that this site is the dominant site in the material.

The various excitation energies were calibrated for this upconversion scheme and are listed in Table 5.2. The transition assignments for this calibration are based on absorption data from Section 4.1 and have been corrected for wavelengths in air.

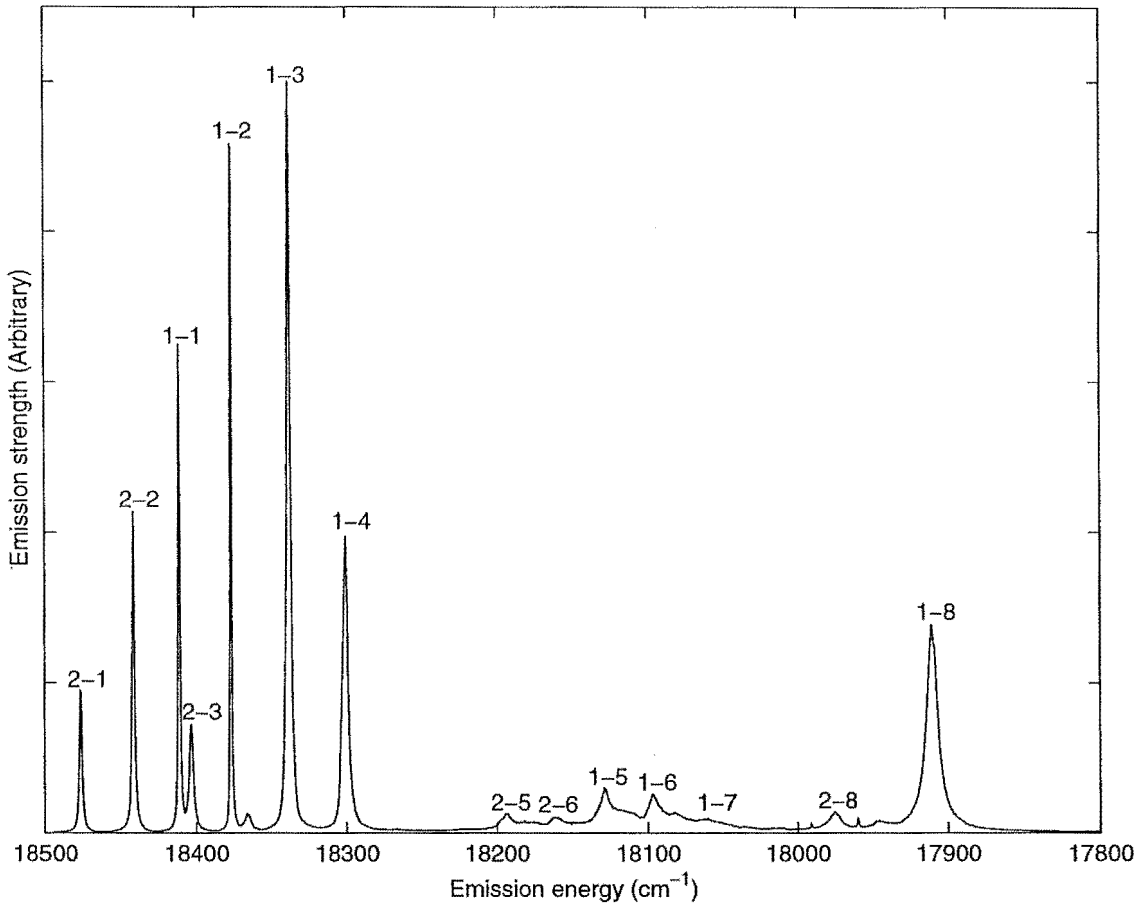

Figure 5.5: 12K $^4S_{3/2}$ emission from infrared excitation at 10316cm^{-1} . Transition assignments E_m - Z_n are labelled m-n for brevity.

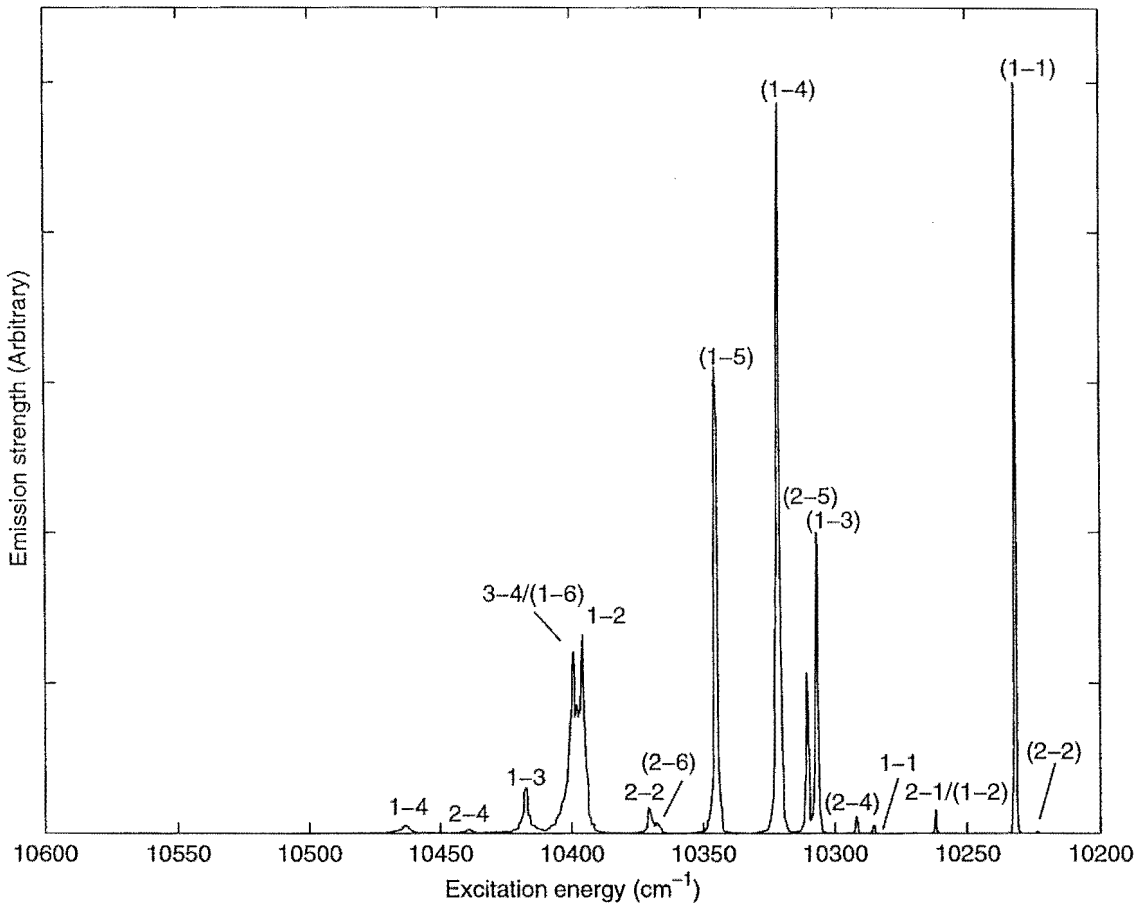

Figure 5.6: 12K Narrow band excitation into the $^4I_{11/2}$ multiplet monitoring $^4S_{3/2} \rightarrow ^4I_{15/2}$ emission at 18338cm^{-1} . Transition assignments are based on optical absorption work. Unbracketed transitions m-n refer to excited state absorptions A_m-G_n. Bracketed transitions (m-n) refer to ground-state absorptions, Z_m-A_n. In the case of double resonance, both assignments are given.

Excitation energy (cm^{-1})	Absorption type	Transition assignment
10468	ESA	A_1-G_4
10441	ESA	A_2-G_4
10417	ESA	A_1-G_3
10398	ESA/GSA	A_3-G_4/Z_1-A_6
10395	ESA	A_1-G_2
10366	ESA	A_2-G_2
10363	GSA	Z_2-A_6
10344	GSA	Z_1-A_5
10316	GSA	Z_1-A_4
10306	GSA	Z_2-A_5
10302	GSA	Z_1-A_3
10288	GSA	Z_2-A_4
10283	ESA	A_1-G_1
10261	ESA/GSA	A_2-G_1/Z_1-A_2
10233	GSA	Z_1-A_1
10225	GSA	Z_2-A_2

Table 5.2: $^4S_{3/2} \rightarrow {}^4I_{15/2}$ upconverted fluorescence from excitation into the $^4I_{11/2}$ multiplet. The transition assignments are given, based on absorption data. Energies are given to $\pm 1 cm^{-1}$. The label ESA refers to an excited-state absorption, while GSA refers to a ground-state absorption transition.

The excitation features clearly characterise both the $^4I_{15/2}$ -$^4I_{11/2}$ ground-state and the $^4I_{11/2}$ -$^4F_{7/2}$ excited state absorption. The two excitation features labelled with ESA/GSA have resonance with both an excited state- and a ground state absorption.

The relationship between upconversion emission strength and input laser power was determined by the measurement of broad-band green emission (545nm) while varying the input laser power. The results of this experiment are shown in Figure 5.7.

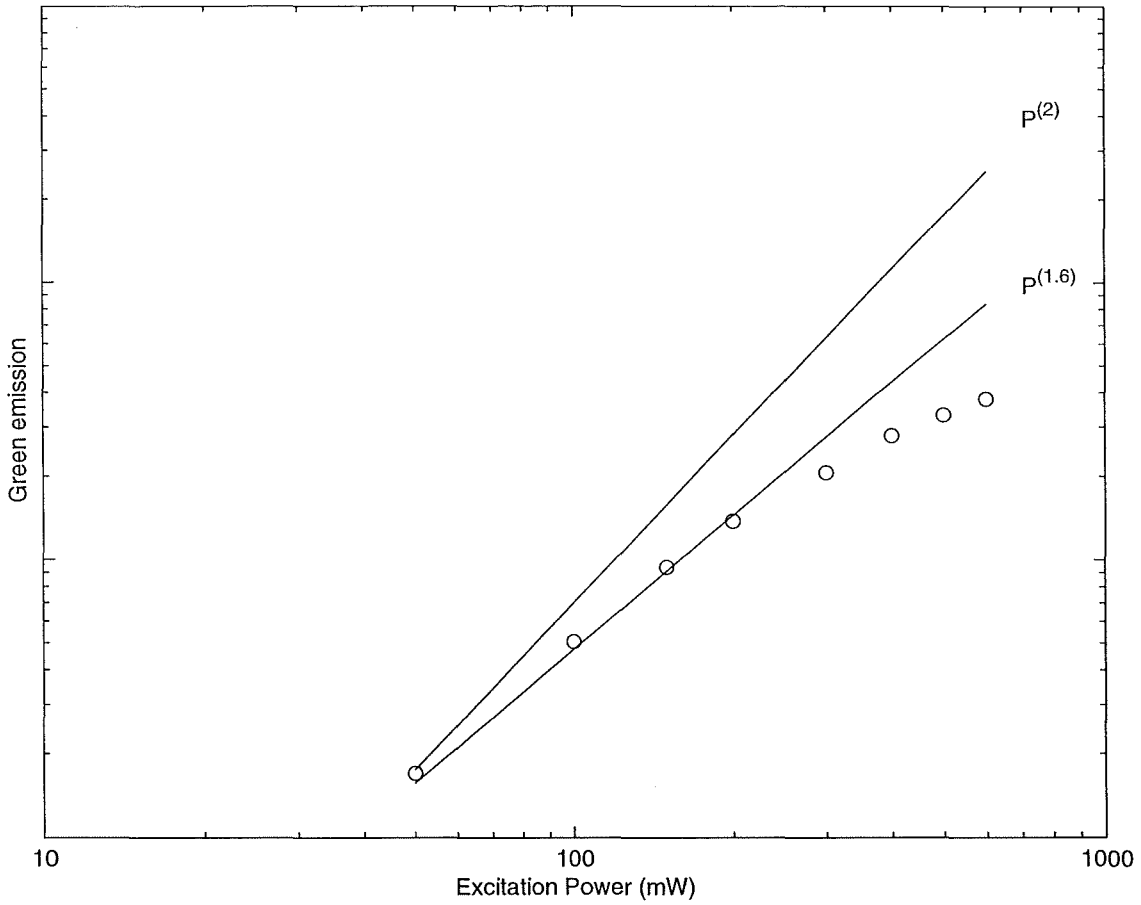

Figure 5.7: Green upconverted emission intensity dependence on input laser power. Lines show ideal power-law relations.

For upconversion processes involving two input photons the upconverted emission intensity would be expected to follow a quadratic dependence on the input laser power. The data show an exponent of 1.6 up to 200mW where saturation towards a more linear power dependence occurs. Another feature of this experiment was the observation in emission of relatively long-lifetime decays immediately the laser beam is incident on the sample. Initial fluorescence decays exponentially to a steady level with a time-constant of τ ~0.5s. These lifetimes are far longer than those expected for fluorescence lifetimes of rare-earth ion multiplets at such low temperatures, and further investigations are detailed

in later sections.

The relation between input laser power, and upconversion emission strength can also be seen to vary depending upon the type of resonance (either ground-state or excited-state) of the transition. Figure 5.8 shows the comparison between the power-dependence relations of both types of resonance. The above saturation-type effects beginning about 150mW are predominantly seen with excitation transitions resonant with a ground-state absorption.

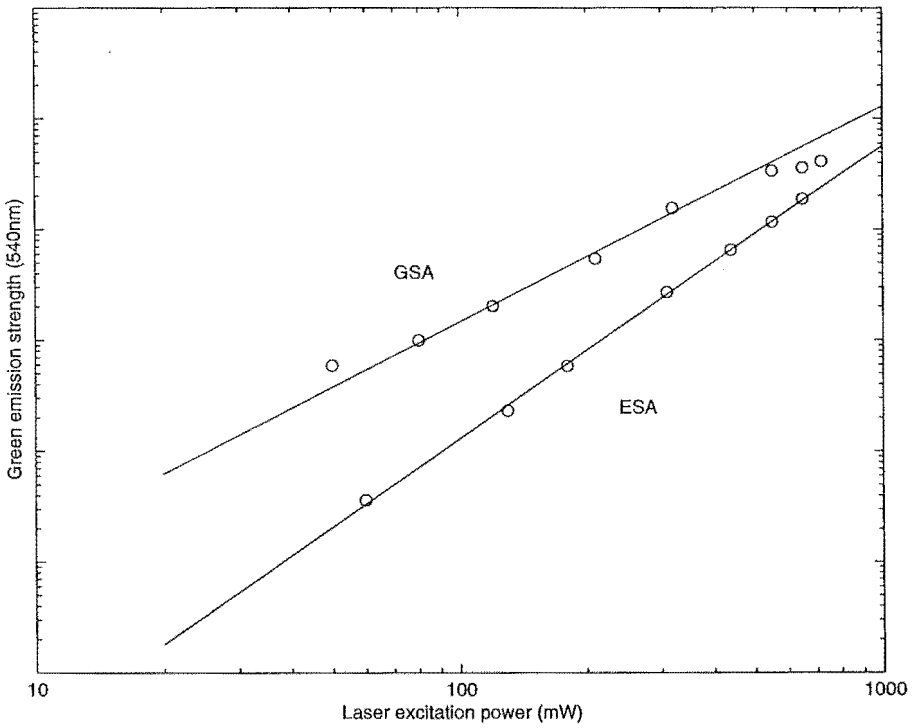

Figure 5.8: Comparison between power-dependence for ground-state and excited-state type resonant transitions. The solid lines represent a best-fit to each of the GSA and ESA data, and correspond to power law exponents of 1.6 and 1.8 respectively.

For low powers at least, the power dependence experiment confirms the mechanism responsible as being a two-photon process.

The incident laser energies that produce the upconversion emission are resonant with either a ground-state $^4I_{15/2} \rightarrow ^4I_{11/2}$ absorption, or the generally higher energy $^4I_{11/2} \rightarrow ^4F_{7/2}$ absorption. This is a characteristic of a two-photon sequential absorption upconversion process. The relatively long fluorescence lifetime of the $^4I_{11/2}$ level ($\sim 300\mu s$ - from Section 4.3) 'stores' excited ions for a sufficiently long time to allow a high probability that the ion will absorb the laser photons. The upconversion mechanism proposed is shown in Figure 5.9.

The excitation energies that are resonant with the ground-state absorption are non-resonant with the excited-state absorption that represents the second step of the up-conversion process. These lower energy photons will still provide excitation from the excited-state by the absorption of suitable lattice phonons. The question as to whether this phonon-assisted process is energetically feasible is addressed using the standard Boltzmann model for the density of vibrational states. At the lowest temperatures used here of 12K, the density of the phonon population has dropped to half at approximately $15cm^{-1}$. In most cases, the energy deficit for the excited-state absorption is of this order of magnitude, and the upconversion process can proceed.

The laser photons resonant with the excited-state absorption have energy greater than that required for the ground-state absorption. These photons are absorbed by ions in the ground-state, releasing the extra energy to the lattice as phonons. This phonon-release process requires only a favourable density of states, and is not dependent upon the occupied thermal distribution.

Several factors influence the temperature dependence of the upconversion process. For example, thermal broadening of the absorption lines will reduce the rate of excitation for resonant transitions. However, the increase in linewidth of the same transitions will relax the resonance conditions. Similarly, an increase in the temperature leads to a corresponding increase in the phonon density, increasing the probability of processes that involve the absorption of phonons. Another factor is the redistribution of population among the resonant crystal-field levels, particularly the reduction in the ground-state population.

As more thermally energetic phonons become available, the strength of upconversion emission from ground-state absorption transitions may be observed to rise as phonon absorption becomes more probable. Eventually, thermal broadening effects will dominate, and considerably reduce the observed emission as the temperature increases beyond about 100K.

The measured temperature dependence is shown in Figures 5.10 and 5.11. Figure 5.10 shows relative broadening of the emission peaks with the increased temperature, while Figure 5.11 is a plot of the integrated emission strength from excitation at each temperature. As the temperature increases, the upconversion signal increases, probably due to the increase in phonon population. The thermal broadening of the lines can be clearly seen in Figure 5.10. It is proposed that this, combined with the removal of ions from the $^4I_{15/2}$ ground-state by thermal redistribution, is responsible for the sharp drop in upconversion emission above 100K. It should be noted that the upconversion emission is still visible at room temperature at an intensity roughly 20% of the maximum.

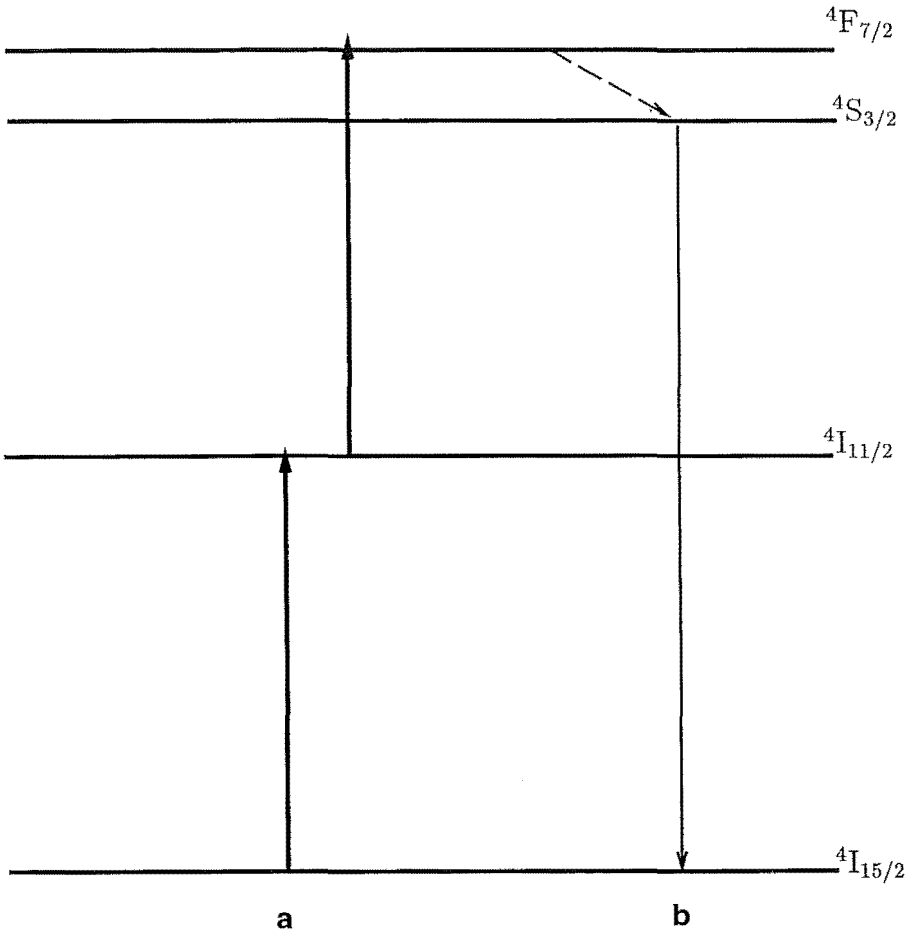

Figure 5.9: Proposed upconversion mechanism for infrared to green emission with infrared excitation into the $^4I_{11/2}$ multiplet of $K_2YF_5:Er^{3+}$

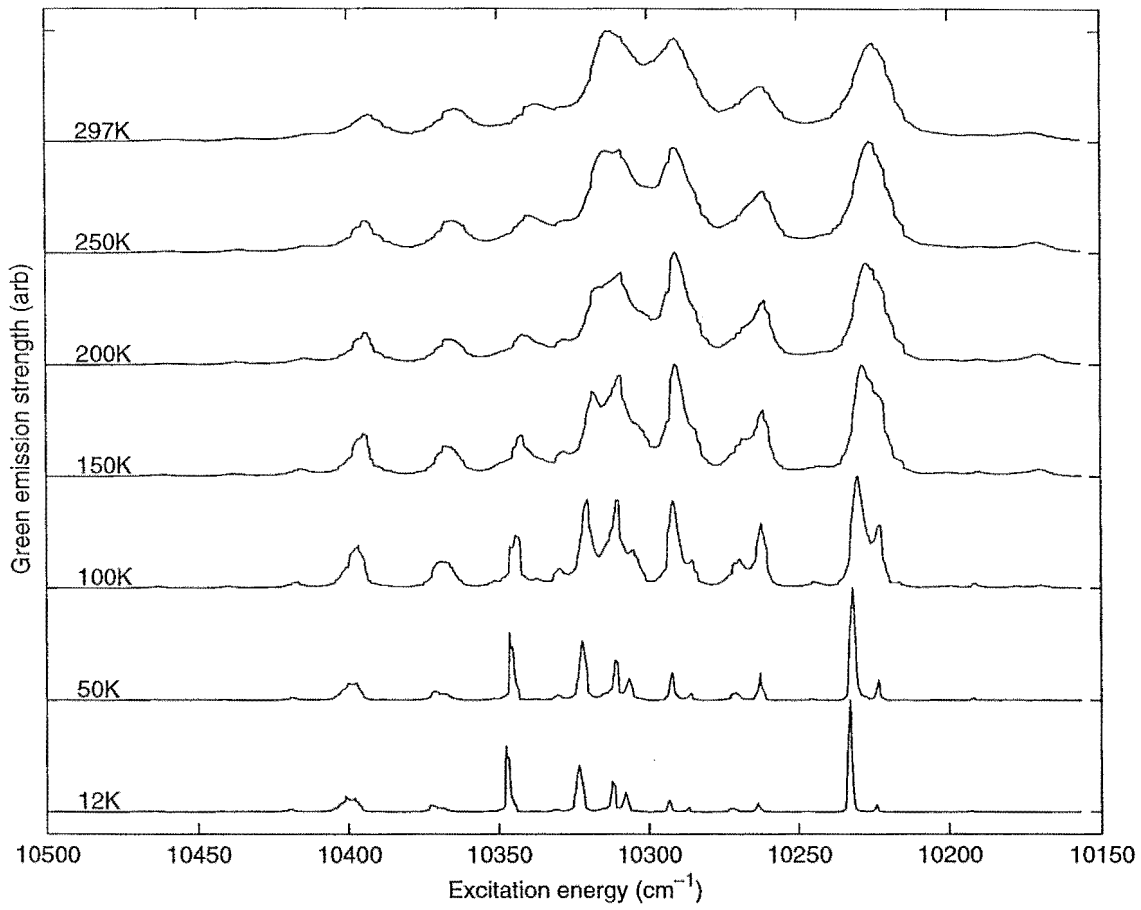

Figure 5.10: Temperature dependence of green (545nm) upconverted emission, with excitation into the $^4I_{11/2}$ multiplet

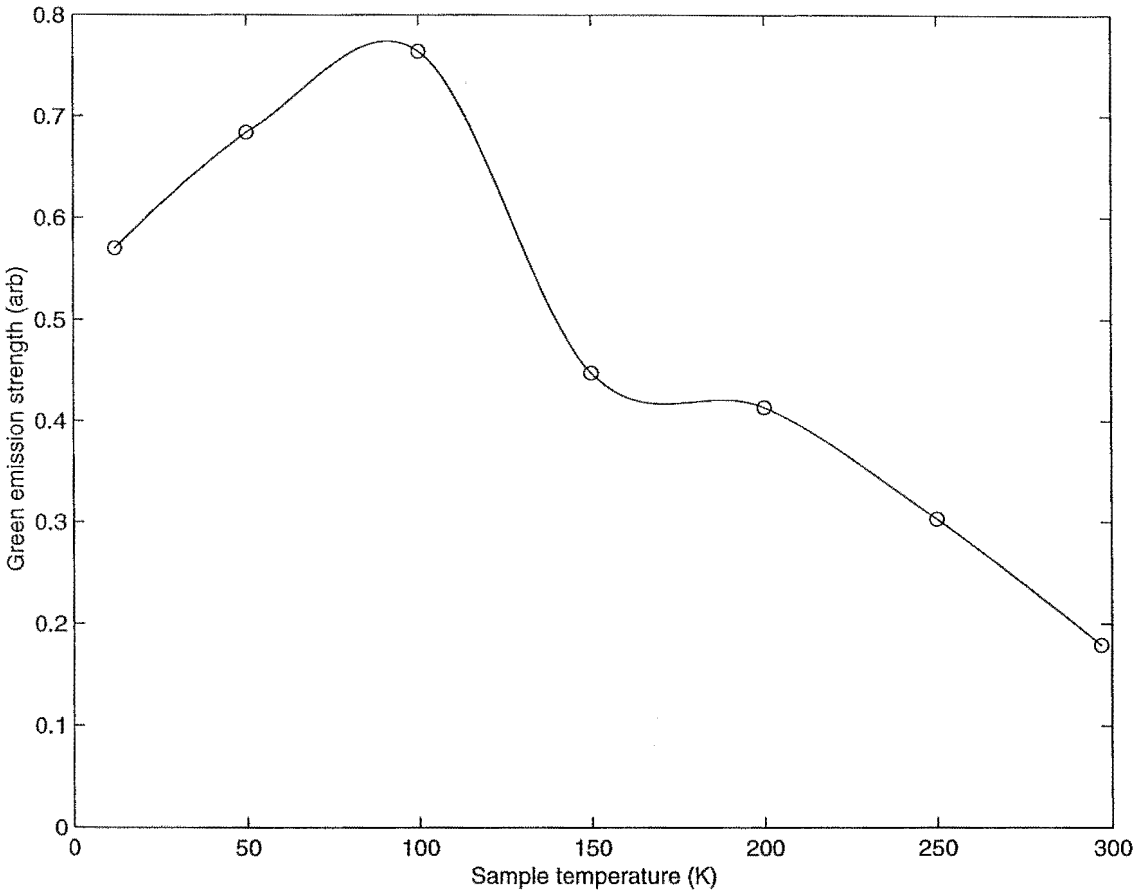

Figure 5.11: Integrated emission strengths for green (545nm) upconversion with excitation into the$^4I_{11/2}$ multiplet of K_2YF_5:Er^{3+} . Solid curve is a guide to the eye only.

5.3 Infrared to blue and near-ultraviolet upconversion in $K_2YF_5:Er^{3+}$

$^2H_{9/2} \rightarrow ^4I_{15/2}$ and $^4G_{11/2} \rightarrow ^4I_{15/2}$ upconversion emission in $K_2YF_5:Er^{3+}$

The energy of upconversion emission from a two-photon process has the obvious limit of twice the laser excitation energy. However, low-intensity fluorescence was observed in the blue and near-ultraviolet spectral regions around 25000cm^{-1} . As the laser photon energy was ~10200cm^{-1} , processes of higher order than two-photon must be involved. Using optical absorption data, this emission has been determined to originate from the $^2H_{9/2}$ (K) and $^4G_{11/2}$ (L) multiplets, at energies of 24000cm^{-1} and 26000cm^{-1} respectively.

The excitation spectra of the emission from both these multiplets were recorded and are shown in Figures 5.12 and 5.13. The excitation energies of the observed features in both correspond to those of the already calibrated $^4S_{3/2} \rightarrow ^4I_{15/2}$ upconversion fluorescence transition. Both the $^2H_{9/2} \rightarrow ^4I_{15/2}$ and the $^4G_{11/2} \rightarrow ^4I_{15/2}$ emission excitation spectra show a mixture of $^4I_{15/2} \rightarrow ^4I_{11/2}$ ground-state transitions and $^4I_{11/2} \rightarrow ^4F_{7/2}$ excited-state absorptions, although no new excitation features.

The excitation spectrum resulting from a 3-step multiphoton process, involving the dominant mechanism of sequential absorption as an initial step, would be expected to firstly characterise the transitions (both ground- and excited-state absorptions) of the initial upconversion process. The additional condition of resonance with further ESA transitions will produce an excitation spectrum that is a convolution of the 2-step excitation spectrum and the energies required for the further excited-state absorption. Under such a scheme, the transition intensities for the various subsequent excited-state absorptions may change markedly in comparison to the original two-photon excitation features.

The fluorescence lifetime of the $^4S_{3/2}$ multiplet of Er^{3+} has been measured to be 800μs, making it suitable as a metastable state for this type of excited-state absorption. Candidate terminating multiplets are the $^2G_{9/2}$,$^2K_{15/2}$ and $^2G_{7/2}$ multiplets, which are all in the region of 27000-28000cm^{-1} . An absorption of a laser photon by an ion in the $^4S_{3/2}$ energy level would excite the ion to about 28700cm^{-1} , requiring roughly 1000cm^{-1} of excess energy released as lattice phonons. The strengths of the excitation lines for such a process would be dependant upon the vibrational spectrum of the material in the region of 1000cm^{-1} , about which little is known.

By considering the possibility of energy transfer between nearby Er^{3+} ions several more energetically favourable mechanisms can be proposed. The previous evidence from site-selective spectroscopy (see Section 4.2) suggests at least one minor symmetry site for the Er^{3+} ion that may represent the random event that two ions are near each other in

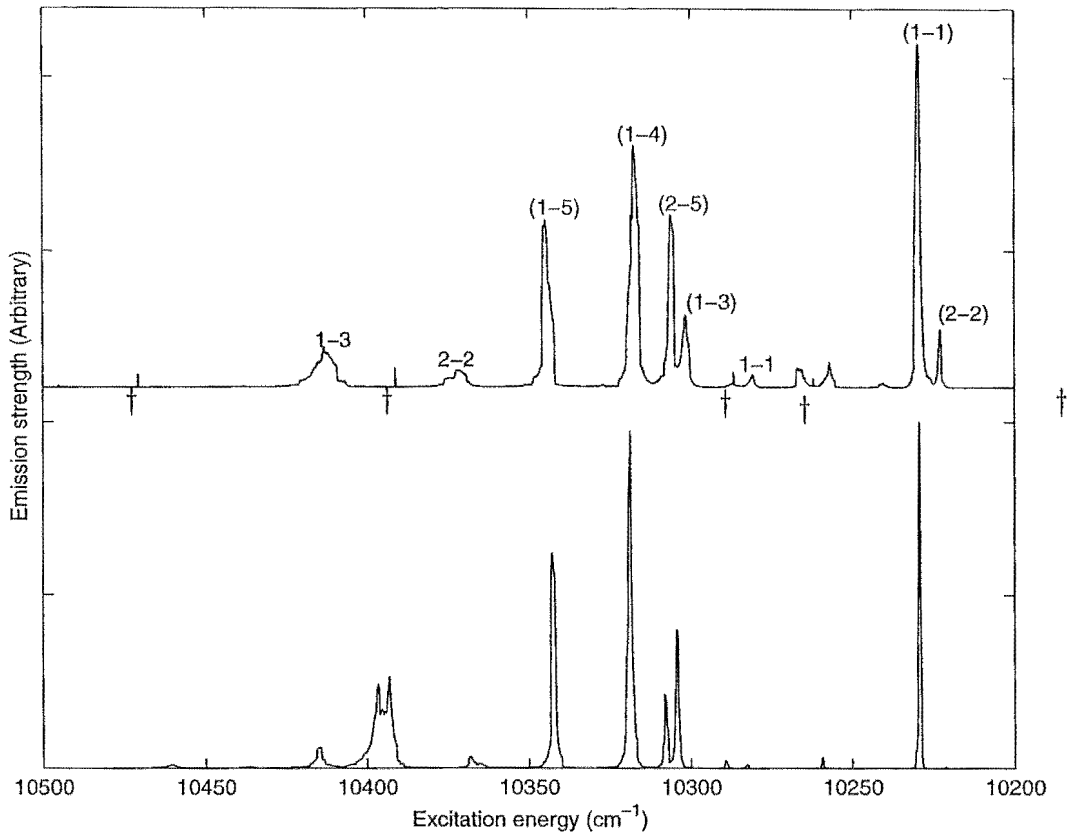

Figure 5.12: 12K $^4I_{11/2}$ excitation spectra for $^2H_{9/2} \rightarrow ^4I_{15/2}$ upconverted fluorescence (top). The corresponding $^4S_{3/2} \rightarrow ^4I_{15/2}$ upconversion emission (bottom) is shown for comparison. Unbracketed transitions m-n refer to excited state absorptions resonant with A_m-G_n. Bracketed transitions (m-n) refer to ground-state absorptions, Z_m-A_n. In the case of double resonance, both assignments are given. The sharp narrow features labelled † are equipment anomalies.

the one-dimensional chain. Direct energy transfer would be possible between such ions. Recent workers have also demonstrated that energy transfer in Tb^{3+}-K_2YF_5 can occur through energy migration along the linear-chain [6]. The separation between donor and acceptor for this last process need not be so small.

Assuming two or more ions can undergo such an energy-transfer, Figure 5.14 shows several mechanisms that could serve to explain the $^2H_{9/2}$ and $^4G_{11/2}$ fluorescence emission.

Figure 5.14(a) shows one possible cross-relaxation that has been demonstrated in other erbium-doped materials [19]. Given a single ion in the excited $^4S_{3/2}$ state, a decay via energy transfer to $^4I_{15/2}$ would provide sufficient energy to excite a coupled $^4I_{11/2}$ ion into the $^2G_{7/2}$ or $^2K_{15/2}$ states. Non-radiative decay by these ions to the emitting $^4G_{11/2}$ and $^2H_{9/2}$ multiplets would allow for the observed emission.

A second cross-relaxation mechanism is shown in Figure 5.14(b). Here the path is

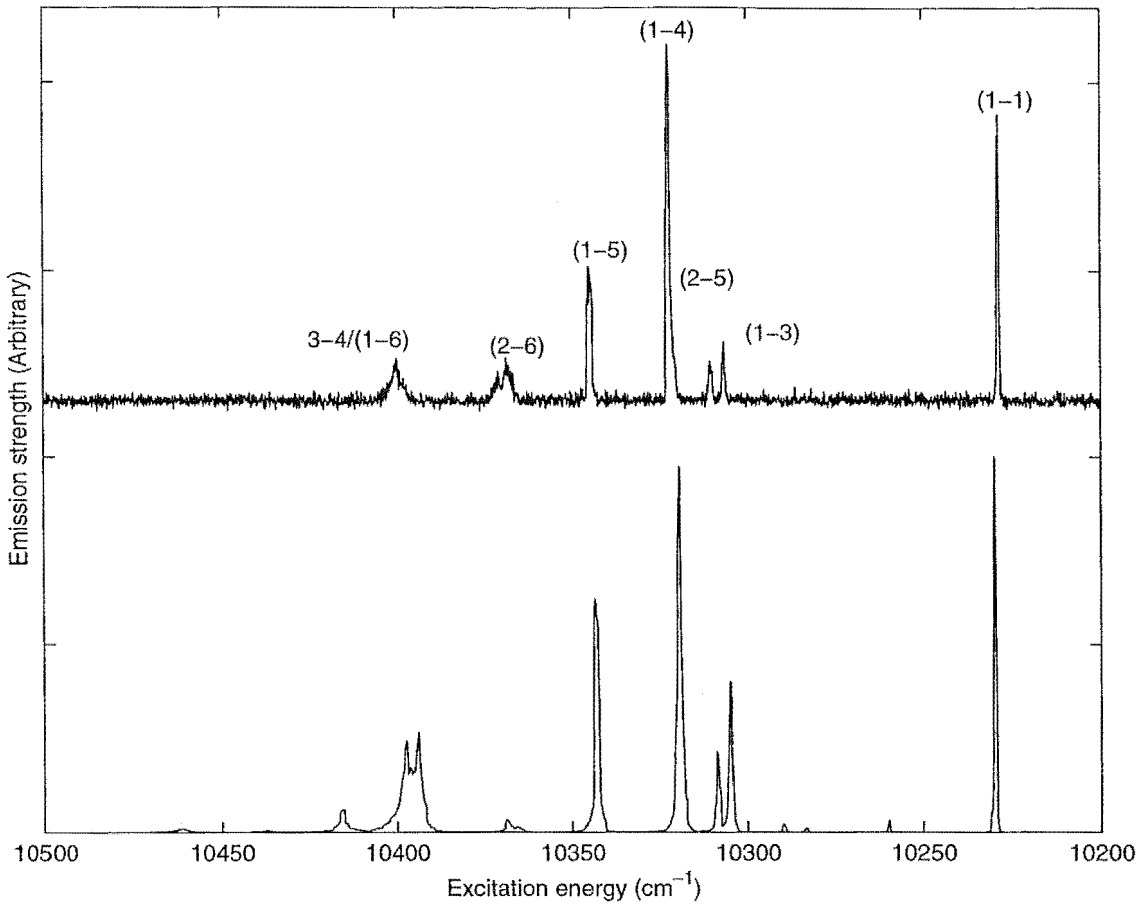

Figure 5.13: 12K $^4I_{11/2}$ excitation spectra for $^4G_{11/2} \rightarrow ^4I_{15/2}$ upconverted fluorescence (top). The corresponding $^4S_{3/2} \rightarrow ^4I_{15/2}$ upconversion emission (bottom) is shown for comparison. Unbracketed transitions m-n refer to excited state absorptions resonant with A_m-G_n. Bracketed transitions (m-n) refer to ground-state absorptions, Z_m-A_n. In the case of double resonance, both assignments are given.

$^4S_{3/2} + {}^4S_{3/2} \rightarrow ^2H_{9/2} + {}^4I_{9/2}$, that is, one excited Er^{3+} ion transfers the $^4S_{3/2} \rightarrow ^2H_{9/2}$ transition energy to the other, in the process itself decaying to the $^4I_{9/2}$ energy level. This process has an energy shortfall of about $100cm^{-1}$ as the $^4S_{3/2} \rightarrow ^4I_{9/2}$ transition can provide at most $6000cm^{-1}$ of the $6100cm^{-1}$ needed to promote an ion from $^4S_{3/2}$ to $^2H_{9/2}$. At a temperature of 12K, the probability of this process will be quite low.

A similar, more energetically favourable mechanism is shown in Figure 5.14(c), where the path is $^4S_{3/2} + {}^4S_{3/2} \rightarrow ^4G_{11/2} + {}^4I_{11/2}$. Here the decay process provides at least $8000cm^{-1}$, compared to a minimum energy requirement for the upwards process of $7930cm^{-1}$.

The upconversion fluorescence spectra recorded for the $^2H_{9/2} \rightarrow ^4I_{15/2}$ and $^4G_{11/2} \rightarrow ^4I_{15/2}$ transitions are shown in Figures 5.15 and 5.16. The $^2H_{9/2} \rightarrow ^4I_{15/2}$ fluorescence spectrum characterises transitions from the three lowest and presumably most

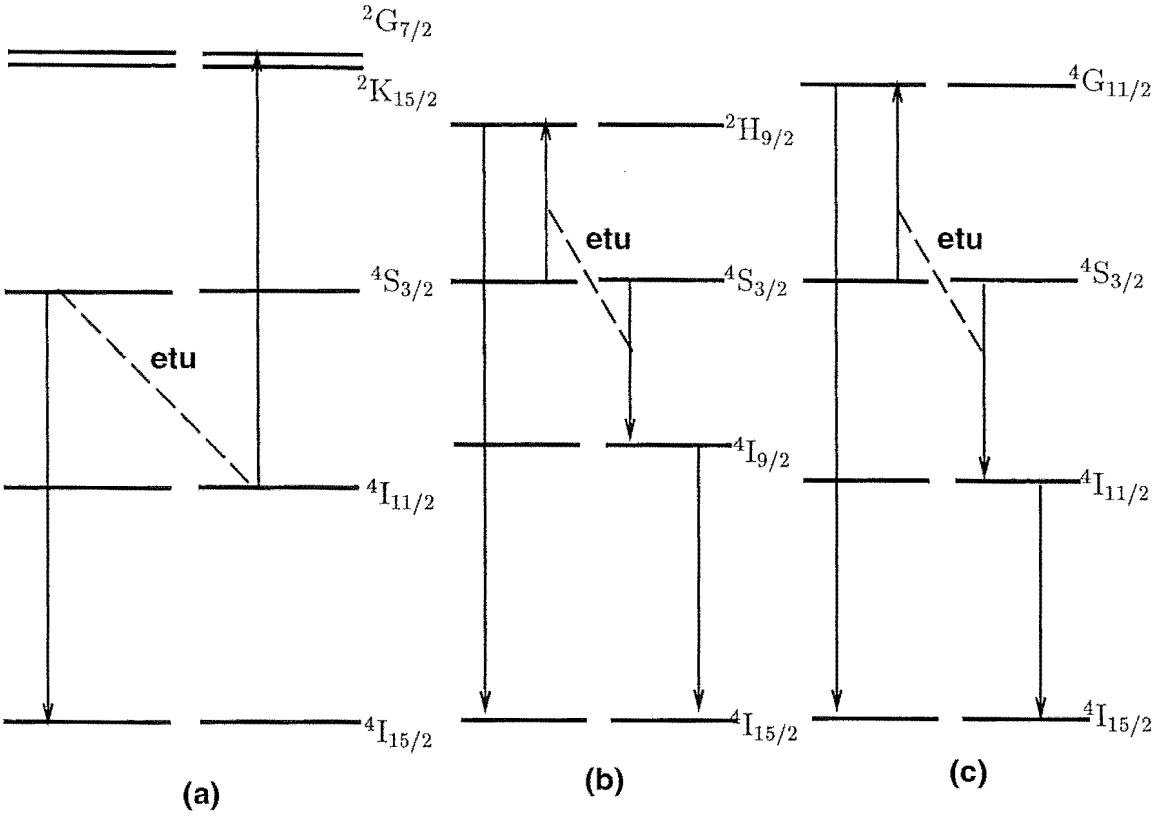

Figure 5.14: Possible energy-transfer upconversion mechanisms to explain $^2H_{9/2}$ and $^4G_{11/2}$ emissions. (a) $^4S_{3/2} + {}^4I_{11/2} \rightarrow {}^4I_{15/2} + {}^2G_{7/2}$ ($^2K_{15/2}$) energy transfer after initial upconversion to $^4S_{3/2}$ (b) $^4S_{3/2} + {}^4S_{3/2} \rightarrow {}^2H_{9/2} + {}^4I_{9/2}$ energy transfer. (c) $^4S_{3/2} + {}^4S_{3/2} \rightarrow {}^4G_{11/2} + {}^4I_{11/2}$ energy transfer.

thermally populated, energy levels of the $^2H_{9/2}$ multiplet. The ground-state splitting pattern is clearly reproduced for each originating upper state level, enabling the transition assignments to be made. Upconversion emission from the higher energy $^2P_{3/2}$ multiplet terminates at the $^4I_{13/2}$ multiplet, and can also be observed adjacent to the $^2H_{9/2} \rightarrow {}^4I_{15/2}$ emission.

The strength of the emission from the $^4G_{11/2}$ multiplet is very weak. The large linewidths of the spectral features are an artifact of the large spectrometer slits, and hence low resolution, required in order to obtain useable data. Despite the low resolution, the features clearly characterise an emission from the two lower crystal-field levels of the $^4G_{11/2}$ multiplet, to the various levels of the $^4I_{15/2}$ ground-state. The energies of the $^4G_{11/2}$ levels L_1 and L_2 so obtained are in agreement with the values obtained from optical absorption studies (Section 4.1).

The fluorescence energies and assigned transitions for the $^2H_{9/2} \rightarrow {}^4I_{15/2}$ and $^4G_{11/2} \rightarrow {}^4I_{15/2}$ emissions are shown in Table 5.3.

Transition energy (cm^{-1})	Transition assignment
26390	-
26371	L_2-Z_1
26351	-
26332	L_1-Z_1
26312	-
26296	L_1-Z_2
26258	L_1-Z_3
26220	L_1-Z_4
26087	L_2-Z_5
26049	L_1-Z_5
26018	L_1-Z_6
25977	L_1-Z_7
25861	-
25831	L_1-Z_8
24650	K_3-Z_1
24614	K_2-Z_1
24580	K_2-Z_2
24540	K_2-Z_3
24523	K_1-Z_1
24503	K_2-Z_4
24488	K_1-Z_2
24450	K_1-Z_3
24412	K_1-Z_4
24334	K_2-Z_5
24266	K_2-Z_7
24239	K_1-Z_5
24208	K_1-Z_6
24172	K_1-Z_7
24114	K_2-Z_8
24056	-
24022	K_1-Z_8

Table 5.3: $^4G_{11/2} \rightarrow {}^4I_{15/2}$ and $^2H_{9/2} \rightarrow {}^4I_{15/2}$ upconverted fluorescence. The transition assignments are given, based on absorption data. Energies are $\pm 1 cm^{-1}$.

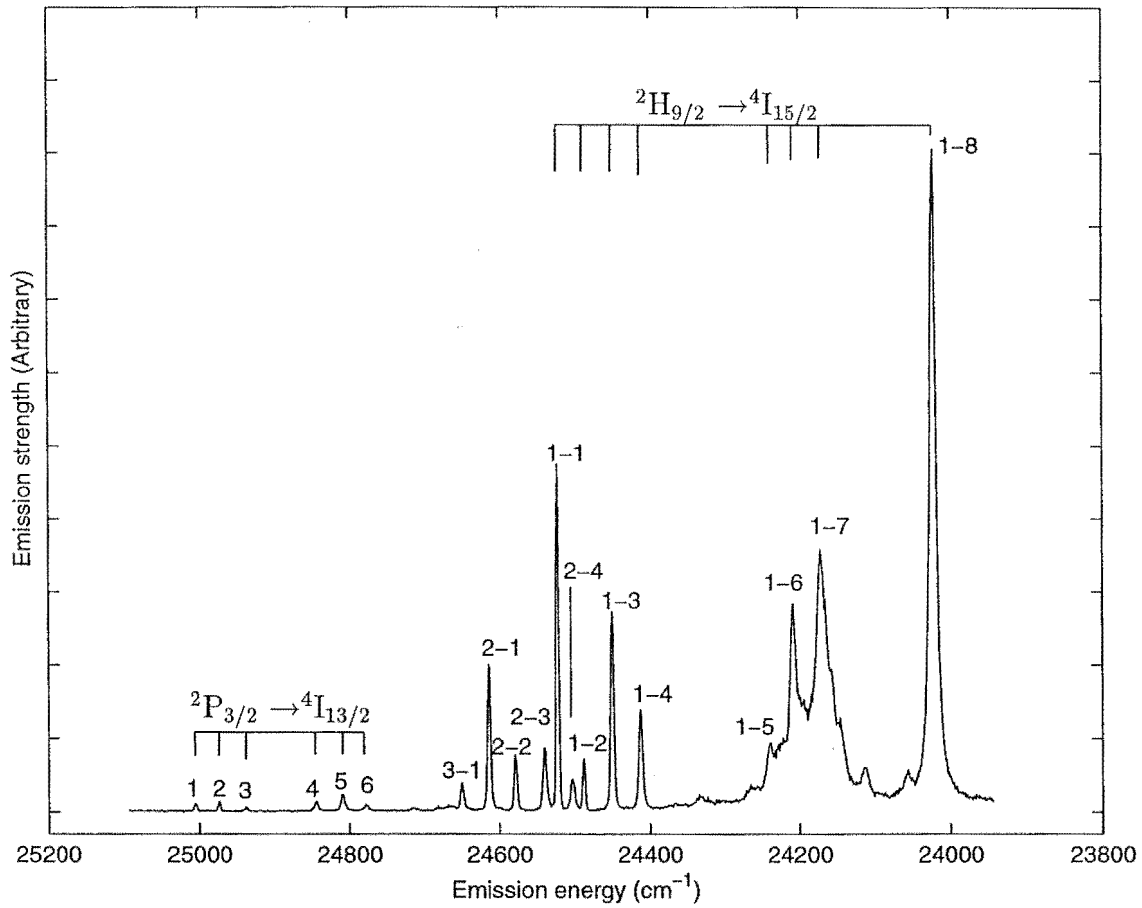

Figure 5.15: 12K near-ultraviolet $^2H_{9/2} \rightarrow ^4I_{15/2}$ emission from infrared excitation into the $^4I_{11/2}$ multiplet. Transition labels K_m-Z_n are given m-n for brevity. The emissions P-Y are labelled by their terminating level only.

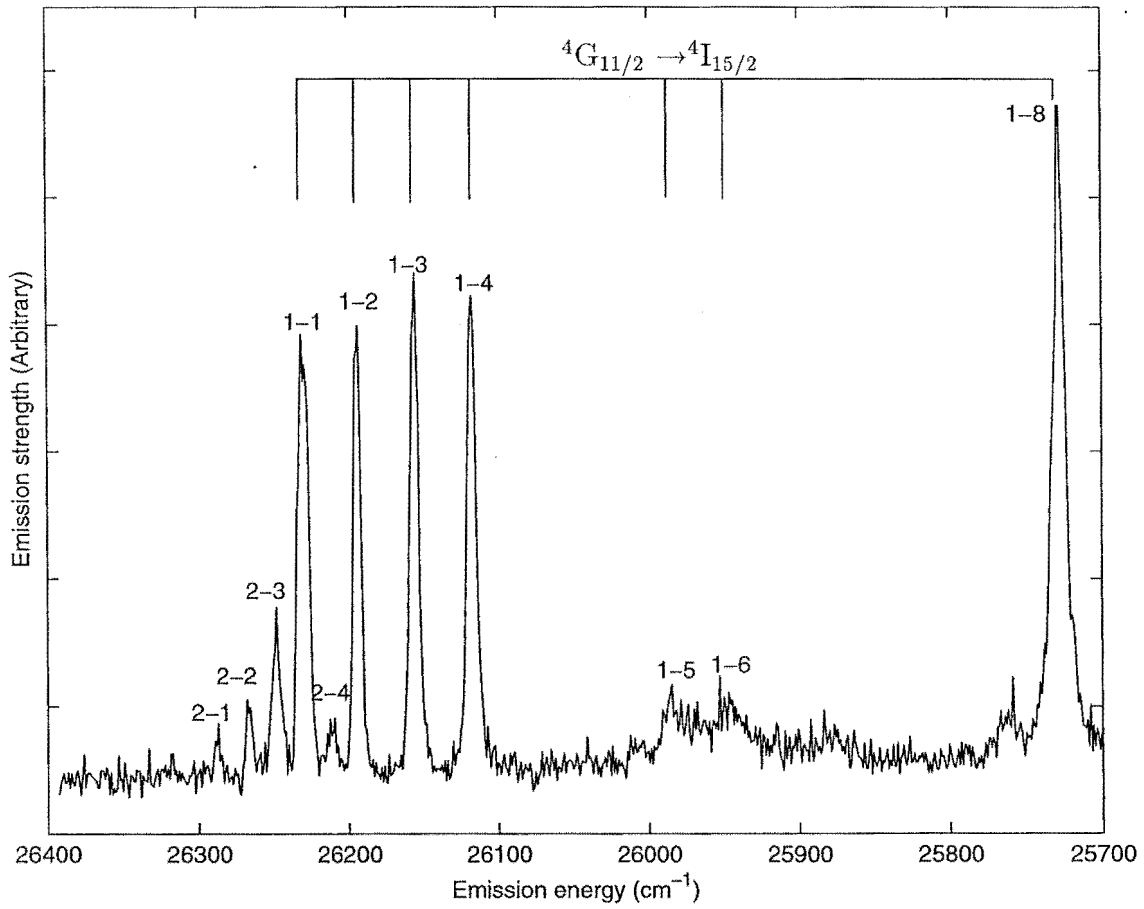

Figure 5.16: 12K near-ultraviolet $^4G_{11/2} \rightarrow ^4I_{15/2}$ emission from infrared excitation into the $^4I_{11/2}$ multiplet. Transitions L_m-Z_n are labelled m-n for brevity.

$^2P_{3/2} \rightarrow ^4I_{13/2}$ upconversion fluorescence

A set of six minor features are visible on the high energy side of the $^2H_{9/2} \rightarrow ^4I_{15/2}$ upconversion fluorescence transitions shown in Figure 5.15. These emissions do not originate from the $^2H_{9/2}$ multiplet, rather the splitting pattern characterises the $^4I_{13/2}$ (Y) multiplet of Er^{3+} , putting the originating multiplet in the region of $\sim$31000cm^{-1} . Carnall *et. al.* [1] give the $^2P_{3/2}$ (P) multiplet of Er^{3+} in LaF_2 at 31700cm^{-1} hence the assignments given in Figure 5.15 and Table 5.4. The $^2P_{3/2}$ multiplet is roughly 500-1000cm^{-1} higher in energy than could be reached by a sequential absorption of three infrared laser photons.

Transition energy (cm^{-1})	Transition assignment
25006	P_1-Y_1
24974	P_1-Y_2
24937	P_1-Y_3
24844	P_1-Y_4
24809	P_1-Y_5
24778	P_1-Y_6
24668	P_1-Y_7

Table 5.4: $^2P_{3/2} \rightarrow ^4I_{15/2}$ upconverted fluorescence. The transition assignments are given, based on absorption data. Energies are $\pm$1cm^{-1} .

The $^2P_{3/2} \rightarrow ^4I_{13/2}$ fluorescence is considerably weaker than other upconversion emissions observed, hence long integration times ($\sim$4s) and wide slits were required to take reliable measurements. Further, to avoid detection of internally scattered light from brighter emissions, an ultraviolet transmission filter (5mm Corning Glass CS-7-59) was used which also reduced detector efficiency by 15%.

Figure 5.17 shows the $^2P_{3/2} \rightarrow ^4I_{13/2}$ emission at 25006cm^{-1} as a function of the laser excitation energy. Also shown for reference is the excitation spectrum for broad-band $^4S_{3/2}$ green emission which has been previously calibrated and assigned to appropriate transitions.

The excitation spectra of these ultraviolet emissions characterises the same set of ESA/GSA transitions as that for the dominant $^4S_{3/2}$ emission. As in the case of the $^2H_{9/2}$ and $^4G_{11/2}$ upconverted emissions, the ESA transitions are slightly weaker, with those at 10468, 10441 and 10417cm^{-1} not visible above the noise level. Clearly the close correlation of these excitation features with those from the broad-band $^4S_{3/2}$ emission indicates that the mechanism behind the $^2P_{3/2} \rightarrow ^4I_{13/2}$ emissions relies initially upon the $^4I_{15/2} \rightarrow ^4I_{11/2}$ / $^4I_{11/2} \rightarrow ^4F_{7/2}$ sequential absorption process detailed previously.

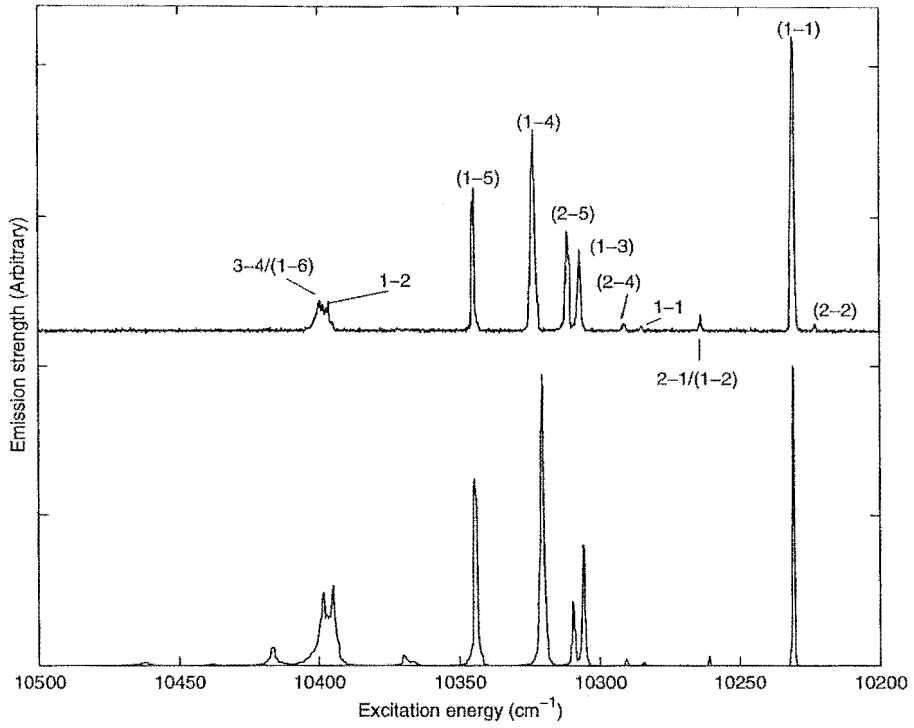

Figure 5.17: $^2P_{3/2} \rightarrow {}^4I_{15/2}$ narrow-band (top) and $^4S_{3/2}$ to $^4I_{15/2}$ broad-band (bottom) excitation spectra. Unbracketed transitions m-n refer to excited state absorptions resonant with A_m-G_n. Bracketed transitions (m-n) refer to ground-state absorptions, Z_m-A_n. In the case of double resonance, both assignments are given.

Any mechanism whereby an Er^{3+} ion is promoted to the $^2P_{3/2}$ multiplet or higher, can also produce the emission from the $^2H_{9/2}$ and $^4G_{11/2}$ multiplets. The similarity of the $^2P_{3/2}$ excitation spectrum (Figure 5.17) to those of the $^2H_{9/2}$ and $^4G_{11/2}$ multiplets also suggests that a single mechanism may be responsible for both.

There are several processes that can be suggested for further investigations. Given the resonance conditions and decreasing lifetimes of higher multiplets, a four-step sequential-absorption mechanism seems unlikely. A more feasible possibility is that an energy transfer exists, say $^4S_{3/2} + {}^4F_{9/2} \rightarrow {}^4I_{15/2} + {}^2K_{13/2}$ or similar, that excites ions into the ultraviolet multiplets directly from the initial upconversion. A detailed study of the ultraviolet multiplets from $^2P_{3/2}$ to $^4G_{9/2}$ for different concentration crystals would be useful.

5.4 Visible upconversion from infrared excitation into the $^4I_{9/2}$ multiplet

The $^4I_{9/2}$ multiplet of Er^{3+} lies at an energy of 12500cm^{-1} , well within the tuning range for the Titanium-sapphire laser in the short-wave mirror configuration. A sample of K_2YF_5:Er^{3+} with a nominal Er^{3+} concentration of 0.6% was excited using this laser source and the resultant emission were again (as in the case of $^4I_{11/2}$ excitation) dominated by green upconversion. An excitation spectra was taken of the broad-band green emission at 540nm (the band pass was approximately 50nm) and the results are shown in Figure 5.18.

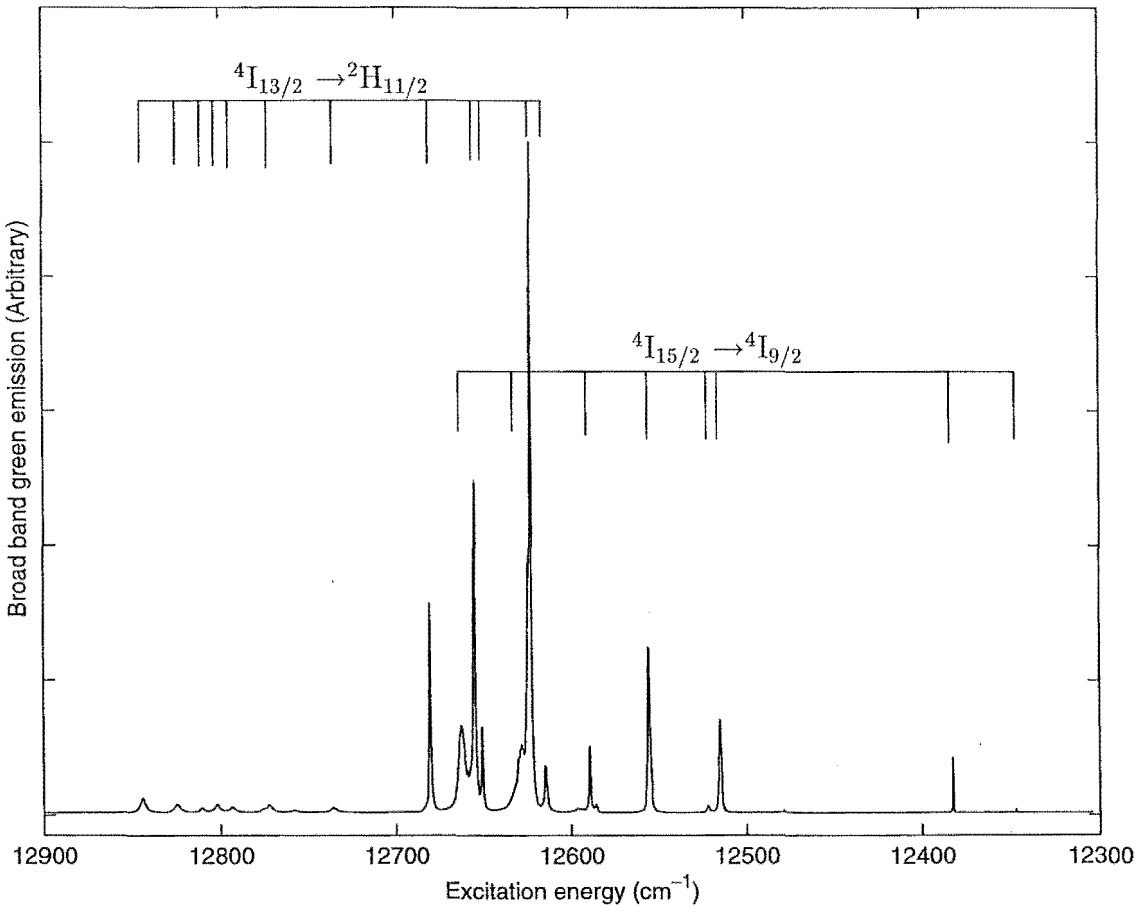

Figure 5.18: 12K excitation spectra of the $^4I_{9/2}$ multiplet of Er^{3+} monitoring broad-band emission at 540nm. Resonant transitions are labelled.

As for excitation into the $^4I_{11/2}$ multiplet, the dominant green emission was found to characterise the $^4S_{3/2} \rightarrow ^4I_{15/2}$ fluorescence, and the spectrum is shown in Figure 5.19. The transition energies are identical to those given in Table 5.2 and are not retabulated here. The strong isolated feature at 18377cm^{-1} was monitored to determine the Er^{3+}

symmetry centres that contribute to this upconversion emission. The results of this site-selective excitation are given in Figure 5.20 and were found to be identical in features to the broad-band emission spectra. Thus the same dominant Er^{3+} site in K_2YF_5 is then involved in both upconversion processes.

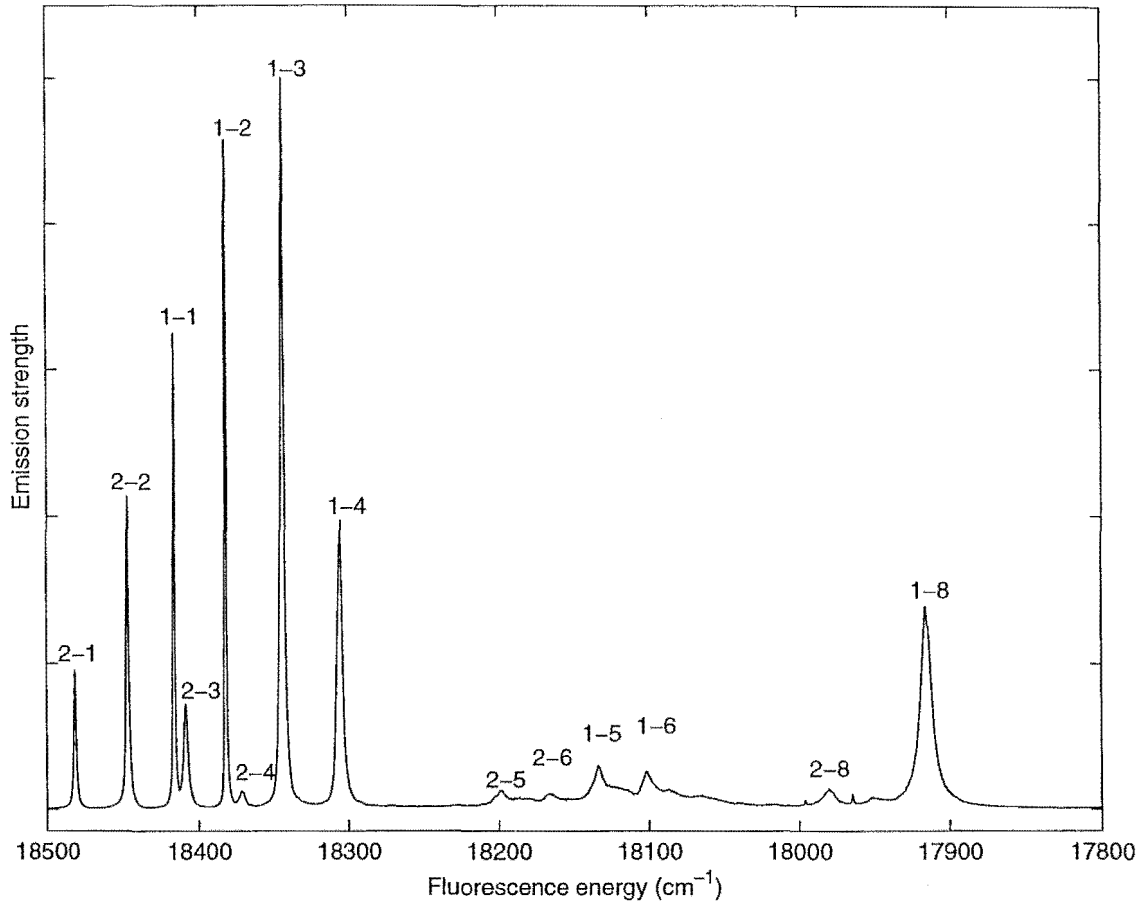

Figure 5.19: 12K $^4S_{3/2} \rightarrow ^4I_{15/2}$ upconverted fluorescence from $^4I_{9/2}$ excitation. Transitions E_m - Z_n are labelled m-n for brevity.

The upconversion excitation features were calibrated and found to characterise resonance energies from each of the $^4I_{15/2} \rightarrow ^4I_{9/2}$ (Z-B), $^4I_{13/2} \rightarrow ^2H_{11/2}$ (Y-F) and $^4I_{11/2} \rightarrow ^4F_{3/2}$ (A-I) transitions. The transition assignments in Table 5.5 show the excitation energies of the features, specifying the originating and terminating levels of the transition.

The broad-band emission strength of the green fluorescence was studied as a function of input laser power and the results are shown in Figure 5.21. As predicted for processes involving a two-photon interaction, a quadratic relation is convincingly shown. The slope of the best fit line shown is 2.0.

The mechanism proposed for this upconversion is a sequential-absorption process, similar to those in the previous case of $^4I_{11/2}$ excitation, although with two distinct paths.

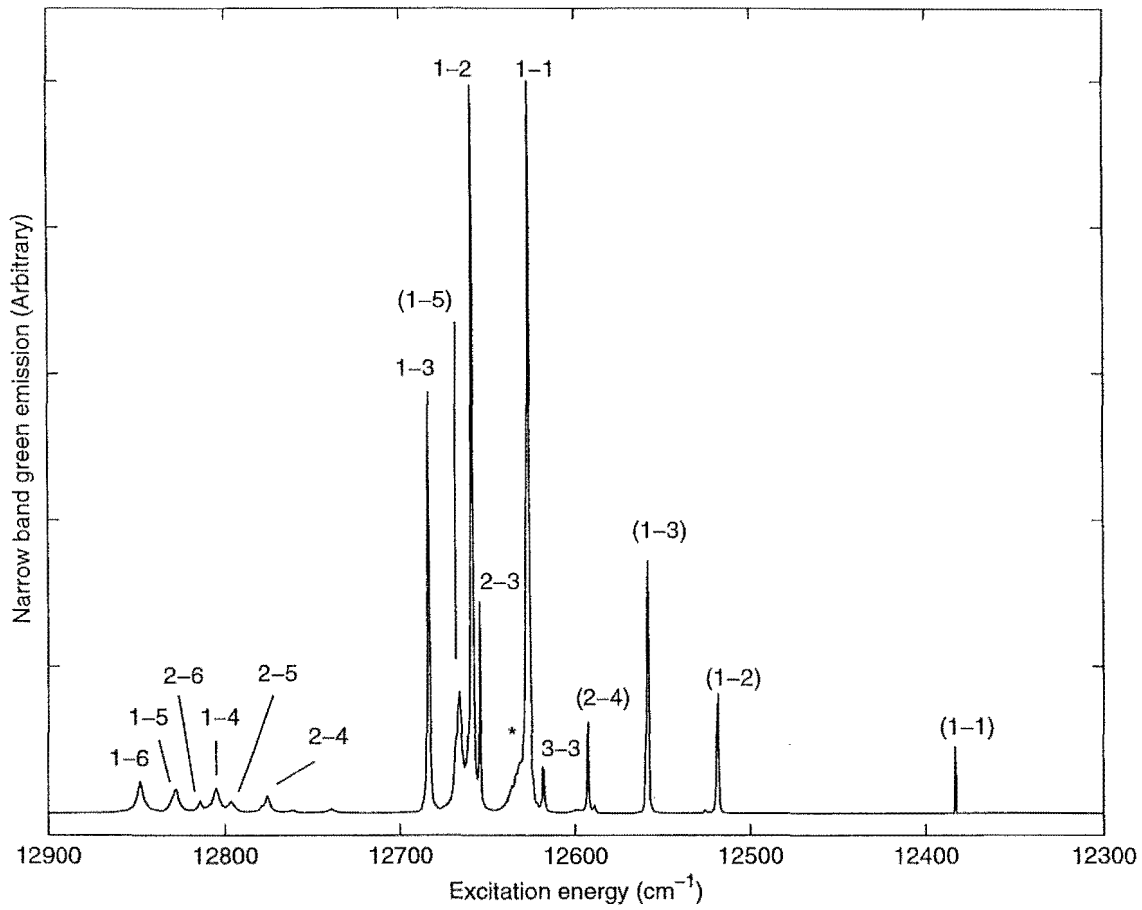

Figure 5.20: 12K Excitation spectra of the $^4I_{9/2}$ multiplet of Er^{3+} , monitoring narrow-band emission at 18377cm^{-1} . Unbracketed transitions m-n refer to excited state absorptions resonant with Y_m-F_n. Bracketed transitions (m-n) refer to ground-state absorptions, Z_m-B_n. In the case of double resonance, both assignments are given. The small feature marked * is the GSA transition (1-4).

Excitation energy (cm^{-1})	Transition assignment
12843	Y_1-F_6
12826	Y_1-F_5
12812	Y_2-F_6
12803	Y_1-F_4
12795	Y_2-F_5
12776	Y_3-F_6
12772	Y_2-F_4
12758	Y_3-F_5
12736	Y_3-F_4
12683	Y_1-F_3
12664	Z_1-B_5
12656	Y_1-F_2
12652	Y_2-F_3
12629	Z_2-B_5
12624	Y_1-F_1/Y_2-F_2
12616	Y_3-F_3
12599	Z_2-B_4
12593	Y_2-F_1
12589	Z_3-B_5/Y_3-F_2
12556	Z_1-B_3/Y_3-F_1
12522	Z_2-B_3
12514	Z_1-B_2
12479	Z_2-B_2
12382	Z_1-B_1
12343	Z_1-B_2

Table 5.5: Calibrated excitation energies for $^4S_{3/2} \rightarrow ^4I_{15/2}$ upconversion fluorescence. The transition assignments are given, based on absorption data. All energies $\pm 1 cm^{-1}$

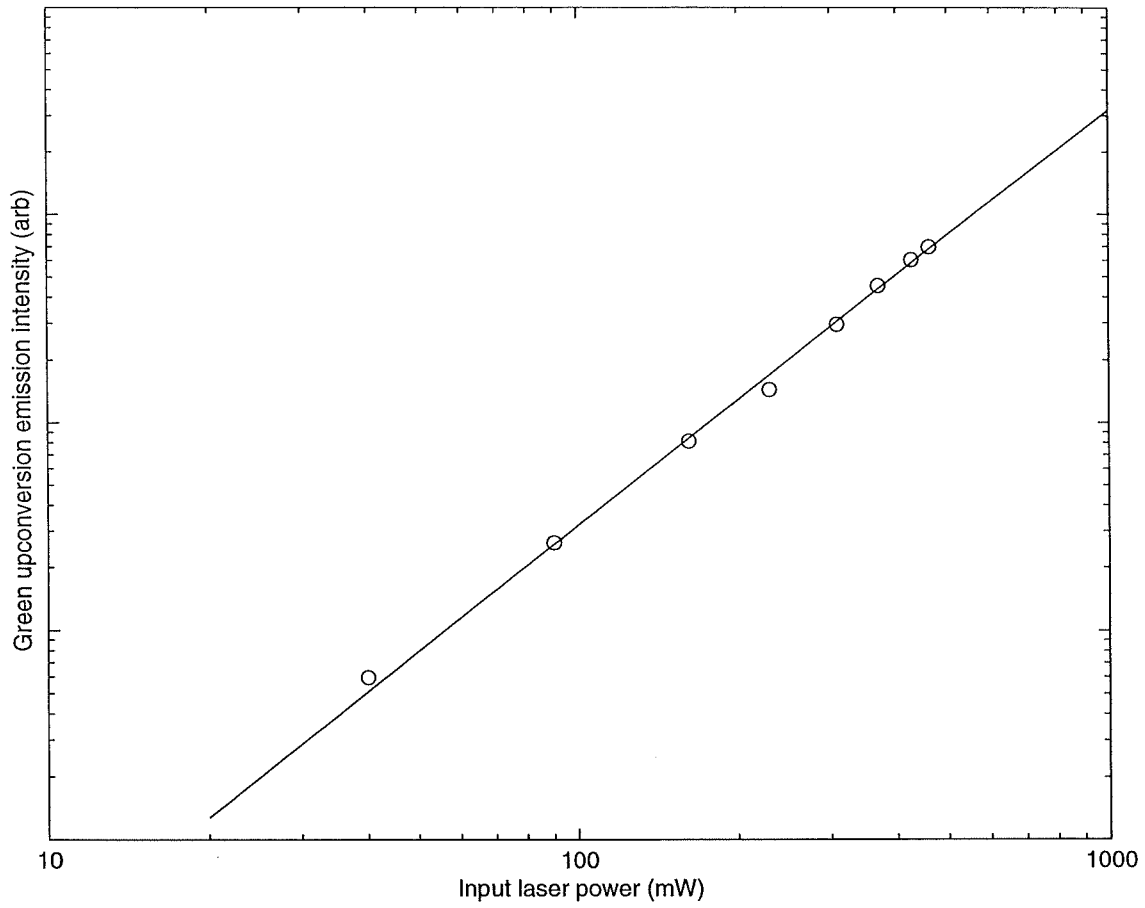

Figure 5.21: Input power dependence of visible emission at 540nm from excitation into the $^4I_{9/2}$ multiplet. Solid line represents a best fit to the experimental data and corresponds to a slope of 2.

The dominant mechanism is clearly that of an absorption resonant with $^4I_{15/2}$ - $^4I_{9/2}$, followed by a decay into the $^4I_{13/2}$ multiplet. The long lifetime of this multiplet of about 800μs facilitates the absorption of a second photon, resonant with the $^4I_{13/2}$ - $^2H_{11/2}$ transition. The $^2H_{11/2}$ multiplet was not found to produce upconversion fluorescence, due to the more favourable non-radiative decay to the close-lying $^4S_{3/2}$ multiplet. The $^4I_{9/2}$ multiplet is also long-lived, and provides for a possible second excited-state absorption into the $^2H_{9/2}$ multiplet. Figure 5.22 shows the proposed mechanism. The laser photons have energies roughly 300cm^{-1} higher than that of the $^4I_{9/2} \rightarrow ^2H_{9/2}$ transition. With the laser resonant with this ESA, the ground-state absorption (with higher energies) is not possible. Therefore, the excitation features corresponding to the energies of the $^4I_{9/2} \rightarrow ^2H_{9/2}$ ESA are not seen.

Figure 5.20 clearly shows that the energies of the $^4I_{15/2} \rightarrow ^4I_{9/2}$ GSA are generally lower than those required for the $^4I_{13/2} \rightarrow ^2H_{11/2}$ ESA. The SAU upconversion process can still proceed for several of those GSA transitions with energies in the region 12600-12700cm^{-1} by the absorption of lattice phonons. Laser energies resonant with lower energy GSA transitions are assumed to populate the $^4S_{3/2}$ multiplet through the $^4I_{9/2} \rightarrow ^2H_{9/2}$ excited-state absorption.

Another energetically possible sequence involves decay to the $^4I_{11/2}$ state followed by excited-state absorption to $^4F_{3/2}$. The $^4I_{11/2}$ multiplet is reasonably long-lived, and hence an excited-state absorption into the $^4F_{3/2}$ state may be possible. However, due to the lack of excitation features characterising the ESA transition ($^4I_{11/2} \rightarrow ^4F_{3/2}$), this mechanism is not thought significant in populating the $^4S_{3/2}$ multiplet.

The temperature dependence of the upconversion emission from the $^4S_{3/2}$ multiplet is shown in Figure 5.23 . As the temperature is increased to room temperature, standard thermal broadening decreases the overall intensity of the emission. One feature of this dependence is the increase with temperature of the relative intensity of the excitation line assigned to the ground state absorption Z_1-B_4. This feature can be clearly seen on the high-energy shoulder of the strong ESA transition Y_1-F_1. This is consistent with the proposed sequential absorption model. The energies and density of the lattice phonons increases with temperature, hence the GSA excitation lines can be expected to strengthen.

These variable temperature dependence spectra were collected whilst keeping input power, experimental geometry, and collection conditions as constant as possible. The emission was also recorded in a broad-band sense , to avoid misleading effects from thermal broadening in the collection process. The integrated emissions from each can therefore give a good indication of the total emission temperature dependence. Figure 5.24 shows the resulting integration.

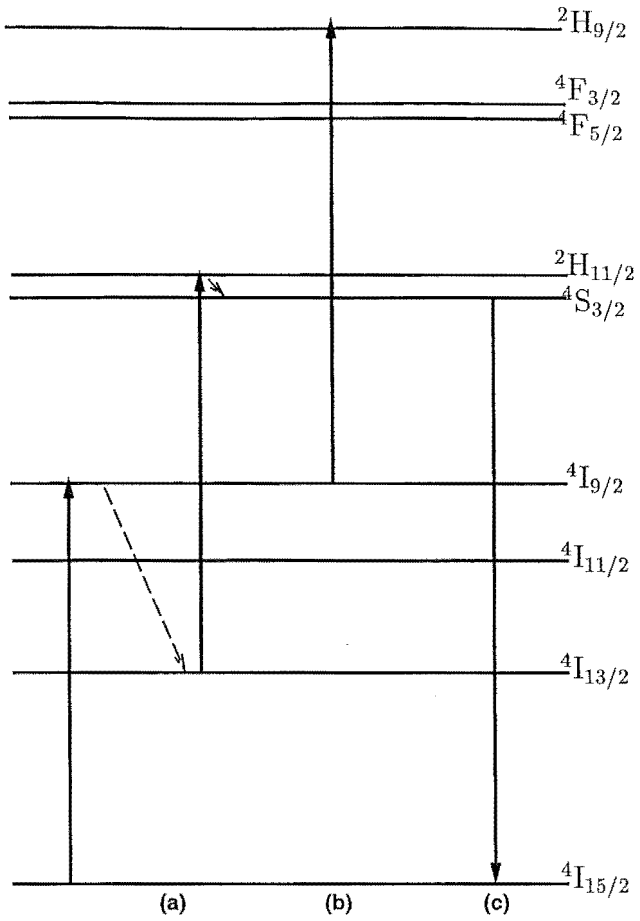

Figure 5.22: Two-photon sequential absorption mechanism for $^4S_{3/2}$ upconversion emission. An initial excitation into the $^4I_{9/2}$ multiplet is followed by (a) decay into the lower metastable $^4I_{13/2}$ state. This decay is followed by excitation into the $^2H_{11/2}$ multiplet by excited-state absorption. The ion then decays to the $^4S_{3/2}$ multiplet. (b) Shows another possible ESA from the $^4I_{9/2}$ multiplet into the $^2H_{9/2}$ multiplet. (c) The dominant $^4S_{3/2} \rightarrow ^4I_{15/2}$ upconversion emission is produced by both mechanisms.

The integrated emission had a maximum at about 50K, consistent with a rise in emission due to the increased efficiency of the phonon-assisted process discussed earlier.

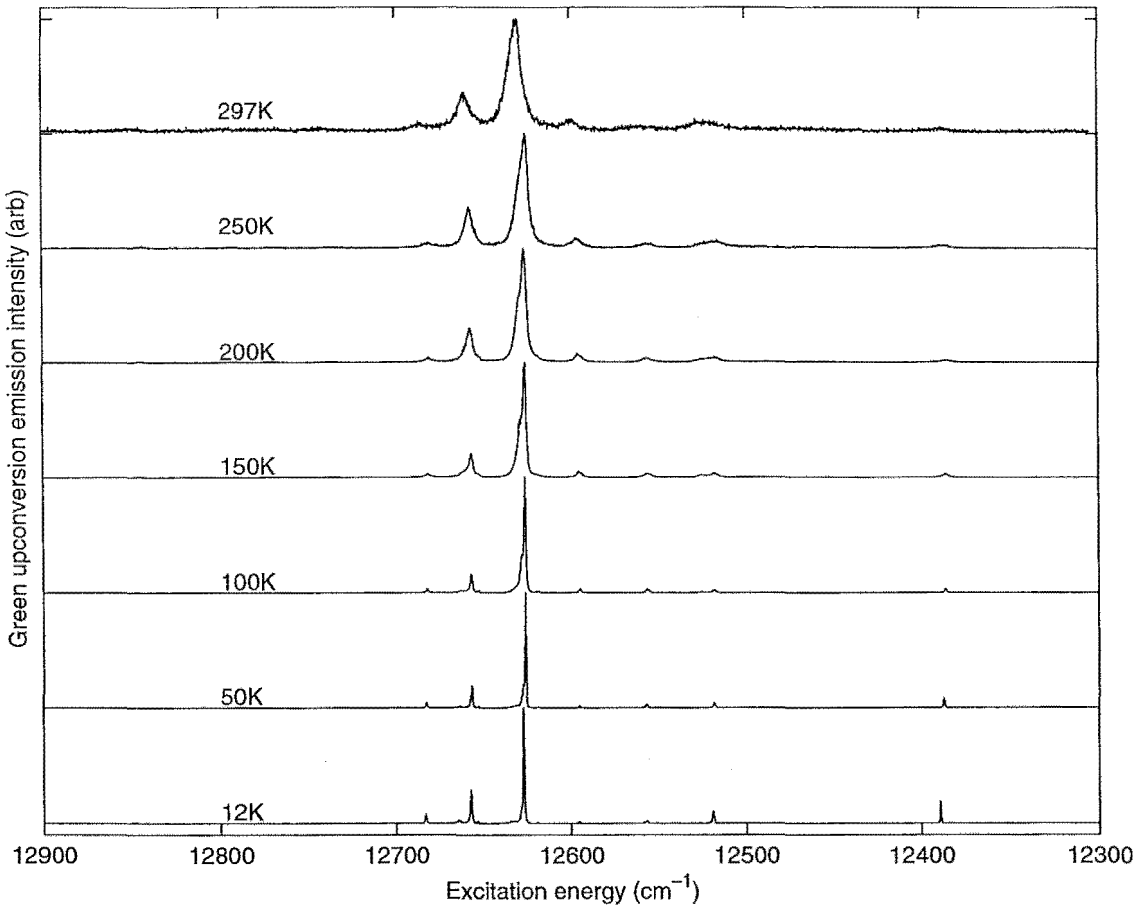

Figure 5.23: Temperature dependence of green (545nm) upconverted emission, with excitation into the $^4I_{9/2}$ multiplet of Er^{3+} . Note that the heights of each spectra have been normalised to allow presentation.

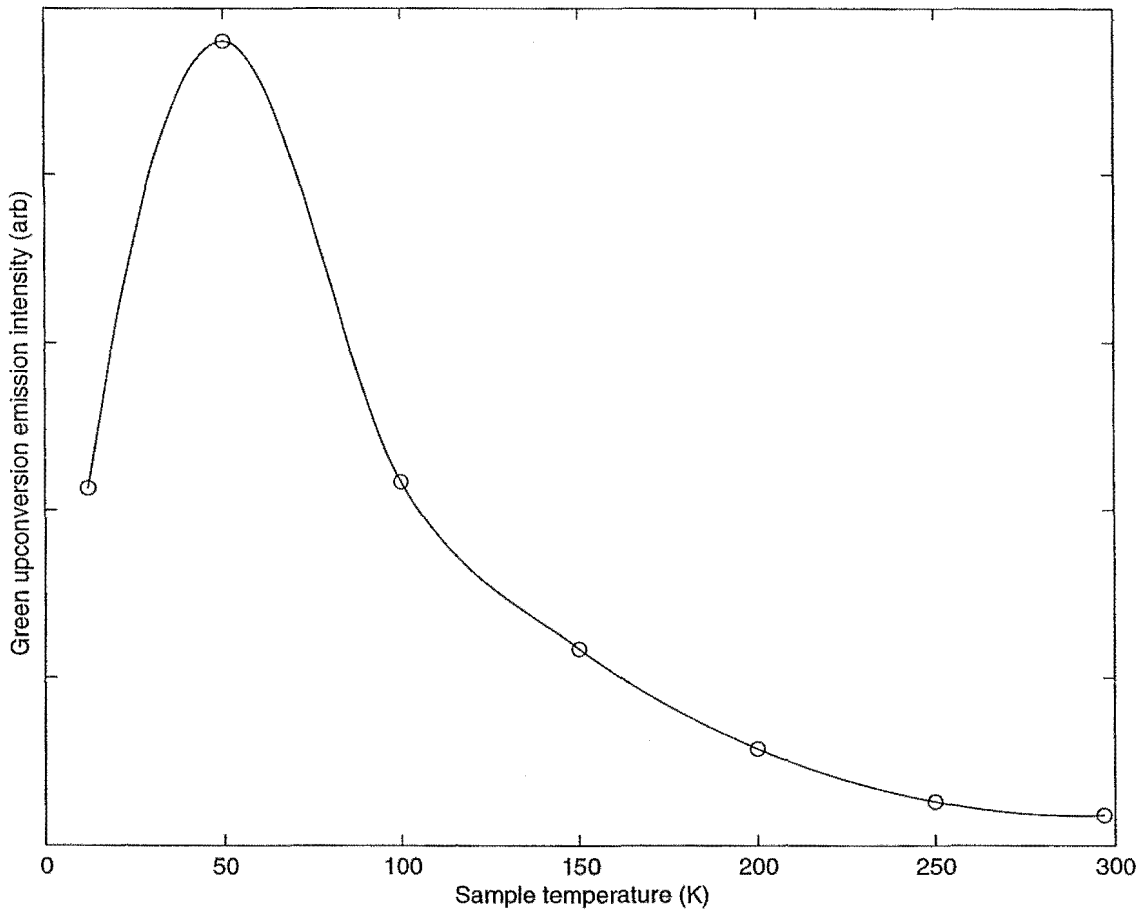

Figure 5.24: Temperature dependence of the integrated signal strength for green (545nm) upconversion with excitation into the $^4I_{9/2}$ multiplet of K_2YF_5:Er^{3+} . Solid curve is a guide to the eye only.

5.5 Blue and ultraviolet upconversion emissions from $^4I_{9/2}$ excitation

$^4F_{5/2} \rightarrow ^4I_{15/2}$, $^2H_{9/2} \rightarrow ^4I_{15/2}$ and $^4G_{11/2} \rightarrow ^4I_{15/2}$ upconversion emission

As in the case for excitation into the $^4I_{11/2}$ multiplet, higher energy emissions were also found from excitation into the $^4I_{9/2}$ multiplet of $K_2YF_5:Er^{3+}$. Upconversion fluorescence originating from the $^4F_{5/2}$, $^2H_{9/2}$ and $^4G_{11/2}$ multiplets was recorded. An excited-state absorption populating $^2H_{9/2}$ from $^4I_{9/2}$ has already been described in the previous section. For a two-photon upconversion process, the final energy of an ion cannot be more than twice the laser photon energy. The energy of the laser at around 12700cm^{-1} gives this limit to be about 25000cm^{-1} , which is lower than the measured energy of the $^4G_{11/2}$ multiplet at 26300cm^{-1} . Therefore, higher-order processes are responsible for the fluorescence from the $^4G_{11/2}$ and $^2P_{3/2}$ multiplets.

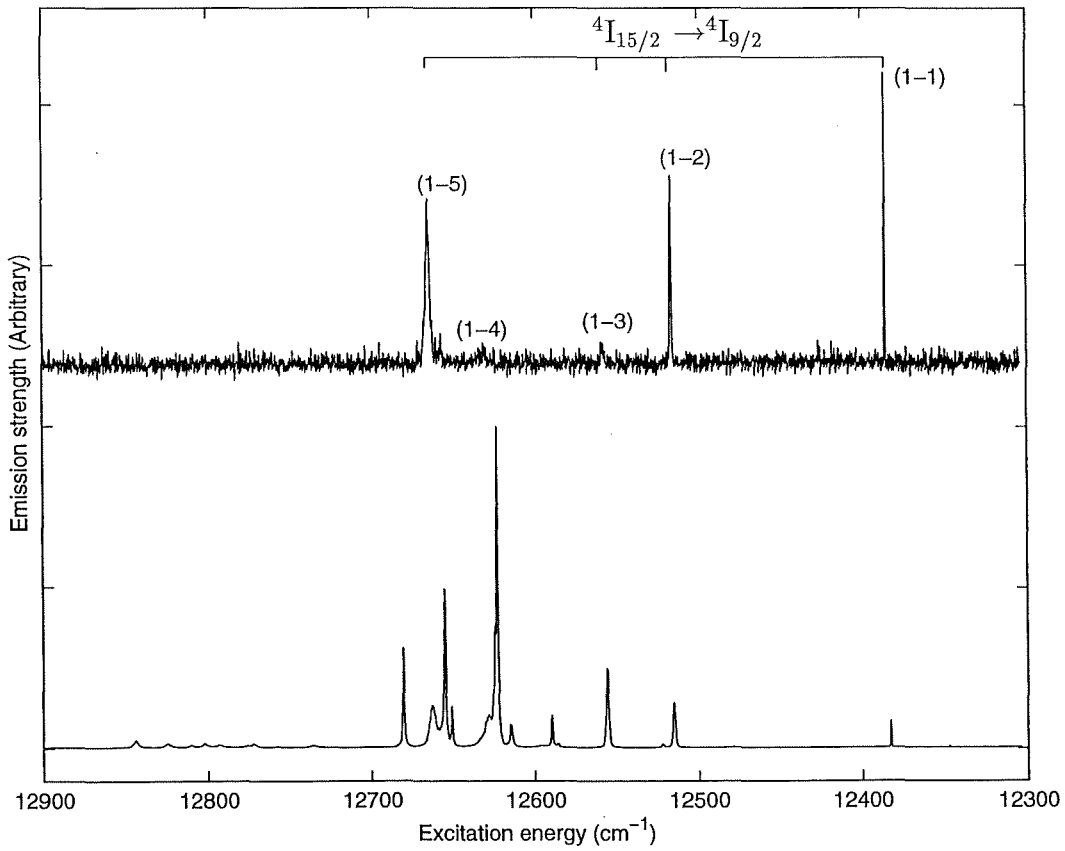

Figure 5.25: (top) 12K Excitation spectra of $^4I_{9/2}$ monitoring $^4G_{11/2} \rightarrow ^4I_{15/2}$ emission (bottom) broad-band $^4S_{3/2}$ emission excitation for reference. Bracketed transitions (m-n) refer to ground-state absorptions, Z_m-B_n. In the case of double resonance, both assignments are given.

The emission from all three multiplets was very weak compared with the dominant

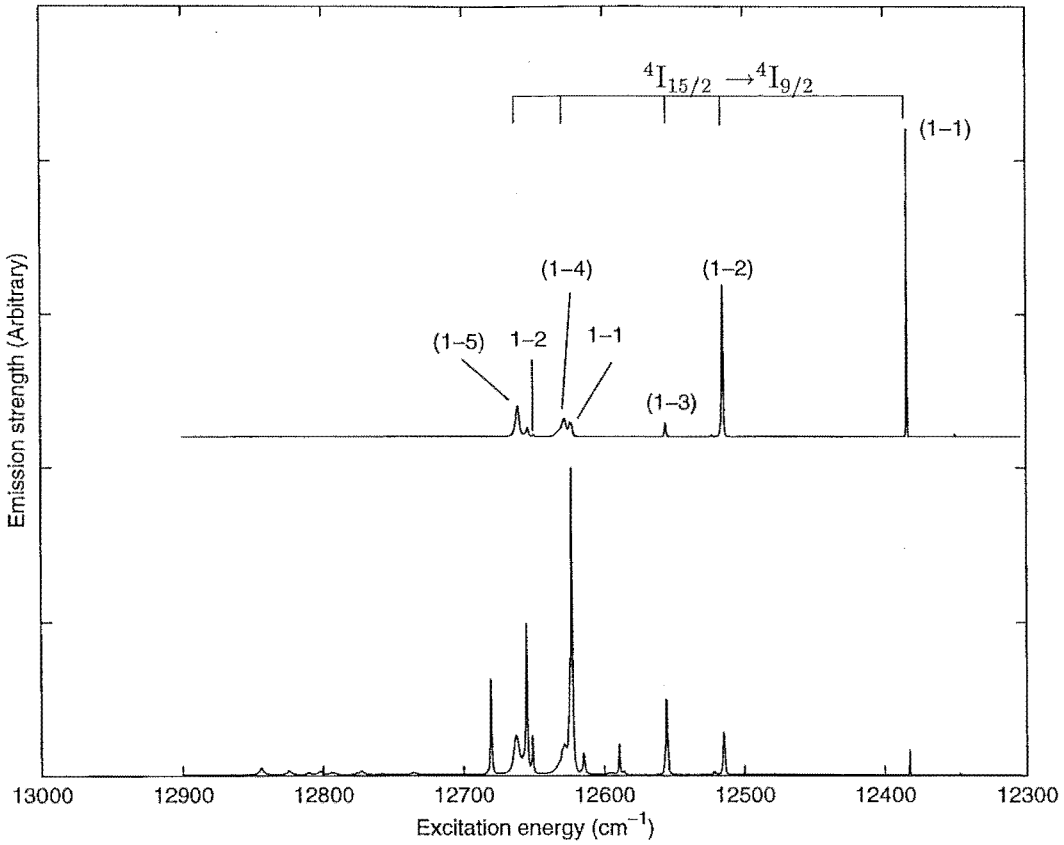

Figure 5.26: (top) 12K Excitation spectra of $^4I_{9/2}$ monitoring $^2H_{9/2} \rightarrow ^4I_{15/2}$ emission (bottom) broadband $^4S_{3/2}$ emission excitation for reference. Unbracketed transitions m-n refer to excited state absorptions resonant with Y_m-F_n. Bracketed transitions (m-n) refer to ground-state absorptions, Z_m-B_n. In the case of double resonance, both assignments are given.

green emission from the $^4S_{3/2}$ multiplet. Often broad linewidths and lower resolutions were obtained as a direct result of the large slit-widths used to obtain the results. The excitation spectra of the emission from the $^4G_{11/2}$ and $^2H_{9/2}$ multiplets are shown in Figures 5.25 and 5.26 respectively. The high noise levels in the $^4G_{11/2} \rightarrow ^4S_{3/2}$ excitation spectra are a direct result of the weakness of those emissions.

The reliance of the $^2H_{9/2}$ and $^4G_{11/2}$ upconversion upon the initial Z-B/Y-F process is shown clearly in the above figures. The energies of the excitation features above, are in all cases coincident with calibrated energies from that initial mechanism. Table 5.5 shows the significant excitation features from the above figures, along with transition assignments for the basic two-step upconversion process from the previous section.

Although the $^2H_{9/2}$ and $^4G_{11/2}$ excitation spectra are very similar to each other, they both differ significantly from the excitation spectrum of the $^4S_{3/2}$ upconversion fluorescence. It is possible that the differences arise because of a further resonance condition

Emission	Excitation energy (cm^{-1})	Prev. assignment	
$^4G_{11/2} \rightarrow ^4I_{15/2}$	12663	Z_1-B_5	
	12629	Z_1-B_4	
	12592	Z_1-B_3	
	12513	Z_1-B_2	
	12382	Z_1-B_1	also D_1-N_8
$^2H_{9/2} \rightarrow ^4I_{15/2}$	12664	Z_1-B_5	
	12656	Y_1-F_2	
	12629	Z_1-B_4	
	12624	Y_1-F_1	
	12592	Z_1-B_3	
	12513	Z_1-B_2	
	12382	Z_1-B_1	also D_1-N_8

Table 5.6: Calibrated excitation features of blue upconversion emission. The transition assignments are given, based on the previous section. All energies are $\pm 1 cm^{-1}$

such as that required for a third photon absorption. The initial two-step process terminates at the $^2H_{11/2}$ multiplet, which decays rapidly to the $^4S_{3/2}$ emitting multiplet. The lifetimes of the $^4S_{3/2}$ and $^4F_{9/2}$ multiplets are $\tau = 330\mu s$ and $\tau = 800\mu s$ respectively, both are long enough to enable each state to act as a metastable storage level for a sequential absorption process. Further, the upconversion transition Z_1-B_1 at $12382 cm^{-1}$ has the laser also resonant with the transition D_1-N_8 between multiplets $^4F_{9/2}$ and $^2K_{15/2}$. Although the higher energy laser photons ($12300\text{-}12600 cm^{-1}$) from the dominant SAU mechanism are non-resonant with the $^4F_{9/2} \rightarrow ^2K_{15/2}$ excited-state absorption, the energy mismatch is of the order of $200 cm^{-1}$. It is therefore reasonable to propose a phonon-assisted sequential-absorption process.

Extra transitions of this type would necessarily be competing with the energy transfer mechanisms proposed to explain this emission from the $^4I_{11/2}$ excitation.

Fluorescence spectra were recorded for the $^4G_{11/2}$ and $^2H_{9/2}$ multiplets and are shown in Figures 5.27 and 5.28 respectively. The noise levels and low resolution of the spectrum for $^4G_{11/2}$ are a direct result of the large slit-widths required to measure this weak emission.

Figure 5.28 clearly shows fluorescence transitions from the two thermally populated crystal-field levels of the $^2H_{9/2}$ multiplet, terminating at the ground-state $^4I_{15/2}$ multiplet. Also visible in this figure is fluorescence originating from the $^2P_{3/2}$ multiplet.

Very weak upconversion emission was also observed from the $^4F_{5/2}$ multiplet of Er^{3+}.

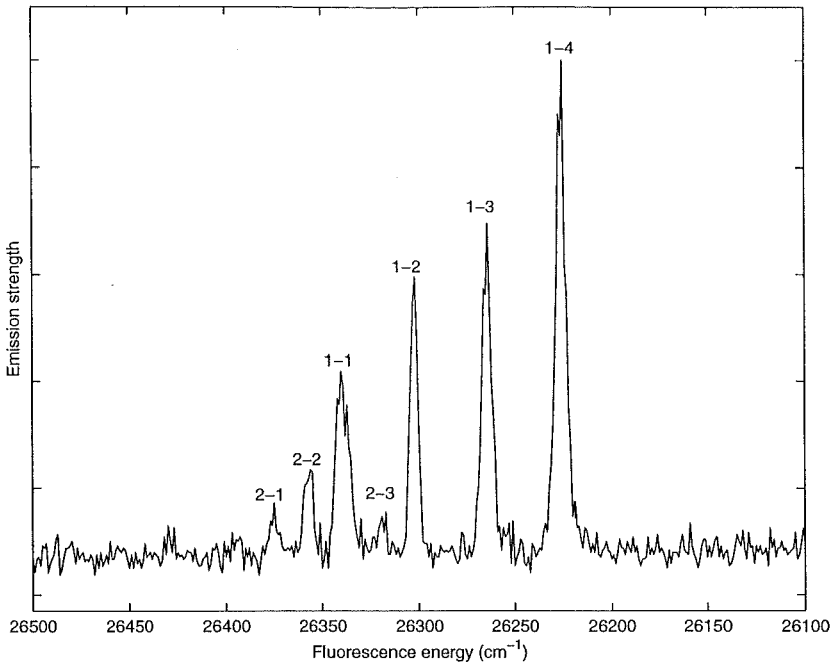

Figure 5.27: 12K $^4G_{11/2} \rightarrow ^4I_{15/2}$ upconverted fluorescence from $^4I_{9/2}$ excitation. Transition assignments are based on absorption data. Transitions L_m - Z_n are labelled m-n for brevity. Features are instrument broadened.

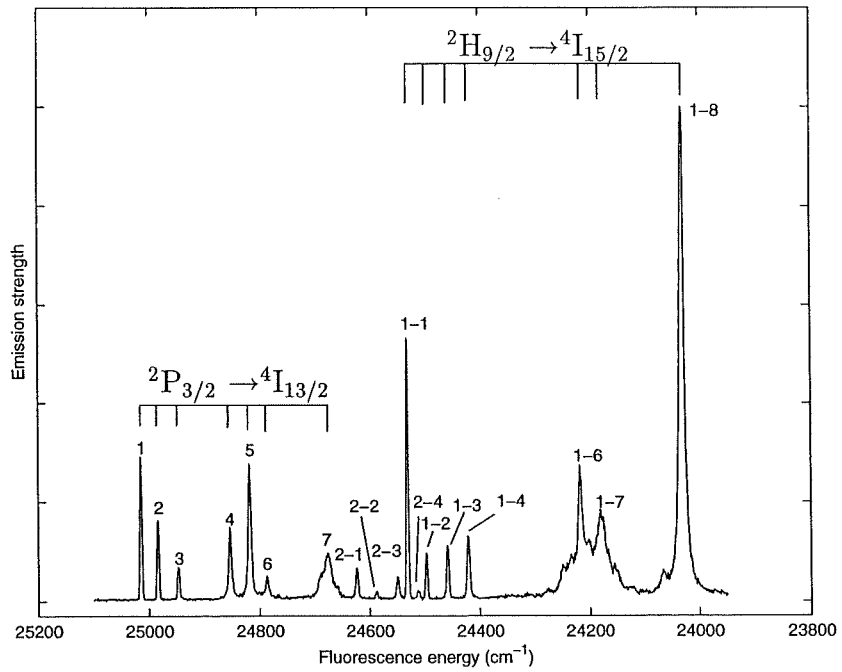

Figure 5.28: 12K $^2H_{9/2} \rightarrow ^4I_{15/2}$ upconverted fluorescence from $^4I_{9/2}$ excitation. Transition assignments are based on absorption data. Transitions K_m - Z_n are labelled m-n for brevity. Transitions $^2P_{3/2} \rightarrow ^4I_{13/2}$ are labelled by terminating level only. Features are instrument broadened.

Long integration times were necessary in order to resolve the fluorescence and only the components H_{1-2}-Z_{1-4} could be resolved. Figure 5.29 shows the emission spectrum of this multiplet, in which the fluorescence transitions have been assigned from previous absorption work.

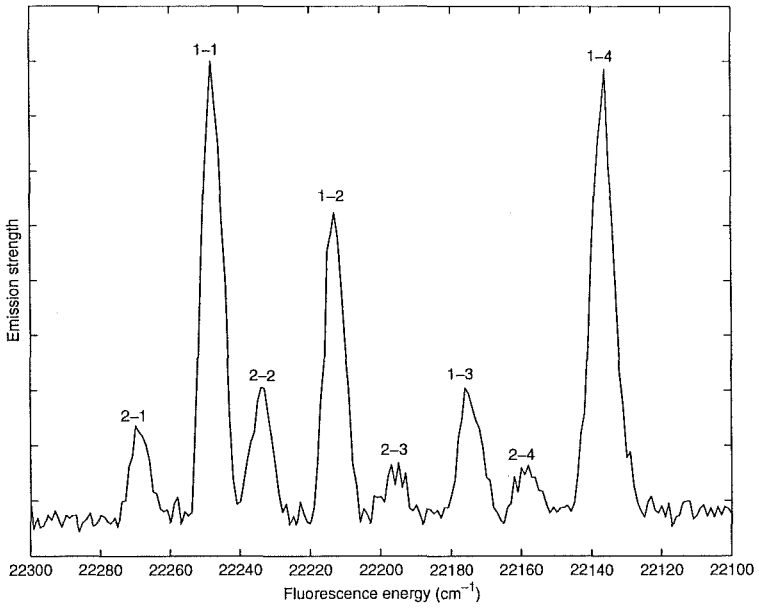

Figure 5.29: 12K $^4F_{5/2} \rightarrow ^4I_{15/2}$ upconverted fluorescence from $^4I_{9/2}$ excitation. Transition assignments are based on absorption data. Transitions H_m - Z_n are labelled m-n for brevity. Features are instrument broadened.

$^2P_{3/2} \rightarrow ^4I_{13/2}$ upconversion emission

The upconversion fluorescence from the high lying $^2P_{3/2}$ multiplet seen in Figure 5.28 is stronger relative to the $^2H_{9/2}$ emission in this excitation scheme, than for $^4I_{11/2}$ excitation. Consequently the excitation spectrum (shown in Figure 5.30) for this multiplet is clearer.

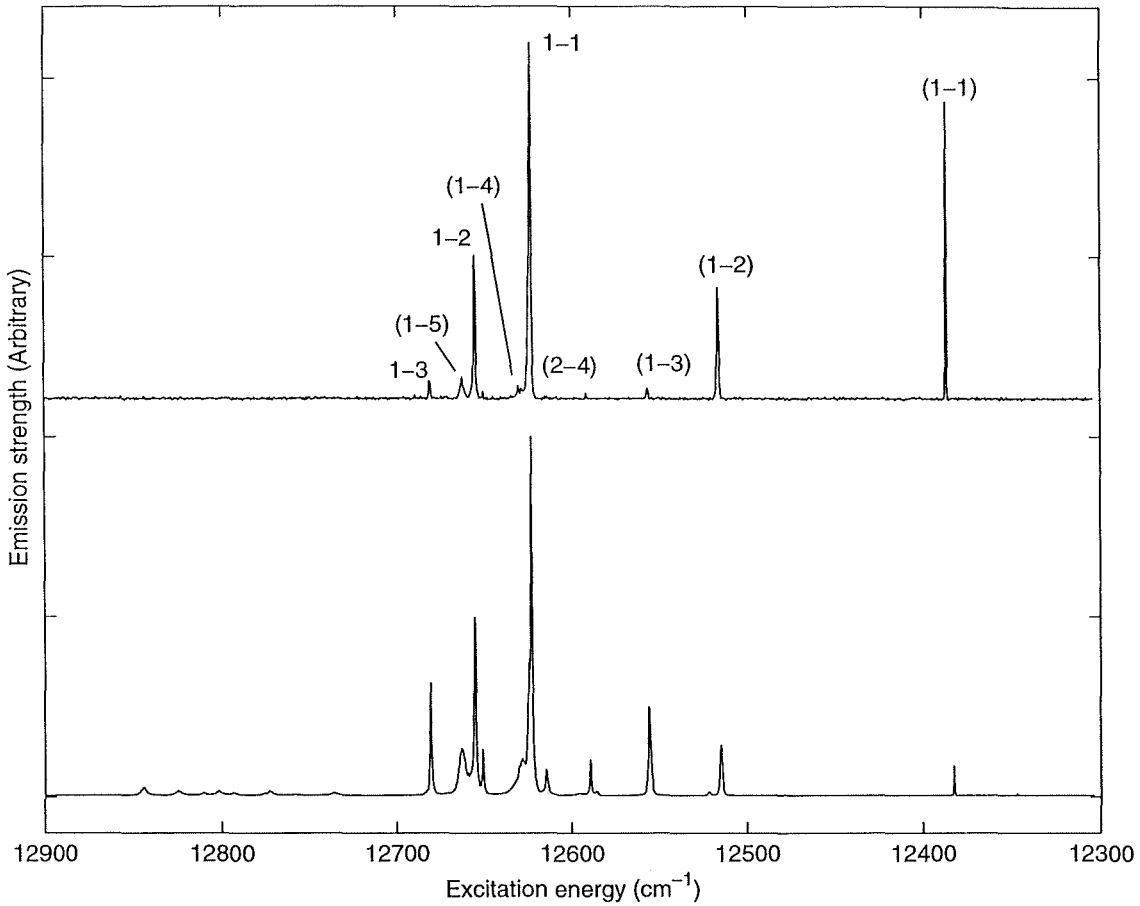

Figure 5.30: (top) 12K excitation spectra of $^4I_{9/2}$ monitoring $^2P_{3/2} \rightarrow ^4I_{13/2}$ emission (bottom) broadband $^4S_{3/2}$ emission excitation for reference. Unbracketed transitions m-n refer to excited state absorptions resonant with Y_m-F_n. Bracketed transitions (m-n) refer to ground-state absorptions, Z_m-B_n. In the case of double resonance, both assignments are given.

The excitation spectrum bears a close similarity to the excitation spectrum for the $^4S_{3/2}$ upconversion emission, sharing both excitation features and similar relative intensities. This is consistent with the energy transfer scheme presented in Section 5.3 for this upconversion emission where ions are excited directly into this state from the $^4F_{9/2}$ or $^4S_{3/2}$ multiplets. In that scheme, ions excited into the $^4S_{3/2}$ multiplet have an equal probability of promotion into the UV multiplets, hence the excitation spectrum will characterise the initial upconversion process. The difference between this spectrum, and those for the emissions from the $^2H_{9/2}$ and $^4G_{11/2}$ multiplets suggest different mechanisms are

responsible for each. Hence it is suggested that the three-step SAU mechanism, proposed earlier for the emissions from the $^2H_{9/2}$ and $^4G_{11/2}$ multiplets, is in competition with this energy-transfer process in that case.

5.6 Red to green and ultraviolet upconversion in $K_2YF_5:Er^{3+}$

From absorption and LSE studies, the $^4F_{9/2}$ multiplet was known to have levels with energies around 15300cm^{-1} that could be excited using a Rhodamine 640 dye laser. As in the case for the two previously studied excitation schemes, this multiplet exhibited strong green upconversion emissions from the $^4S_{3/2}$ multiplet. The fluorescence spectra for the $^4S_{3/2} \rightarrow ^4I_{15/2}$ emissions were found to be identical to those for previous $^4I_{11/2}$ and $^4I_{9/2}$ excitations and are not repeated here. Excitation spectra of the green emission are shown in Figures 5.31 and 5.32. The two excitation spectra correspond to two different wavelength ranges of the birefringent filter used to tune the Rhodamine 640 dye laser.

The energies of the excitation features have been calibrated and are assigned to either a ground-state absorption ($^4I_{15/2} \rightarrow ^4F_{9/2}$) or an excited-state absorption ($^4I_{13/2} \rightarrow ^4F_{5/2}$) components of a sequential absorption upconversion mechanism. Table 5.6 gives the energies and assignments of the features.

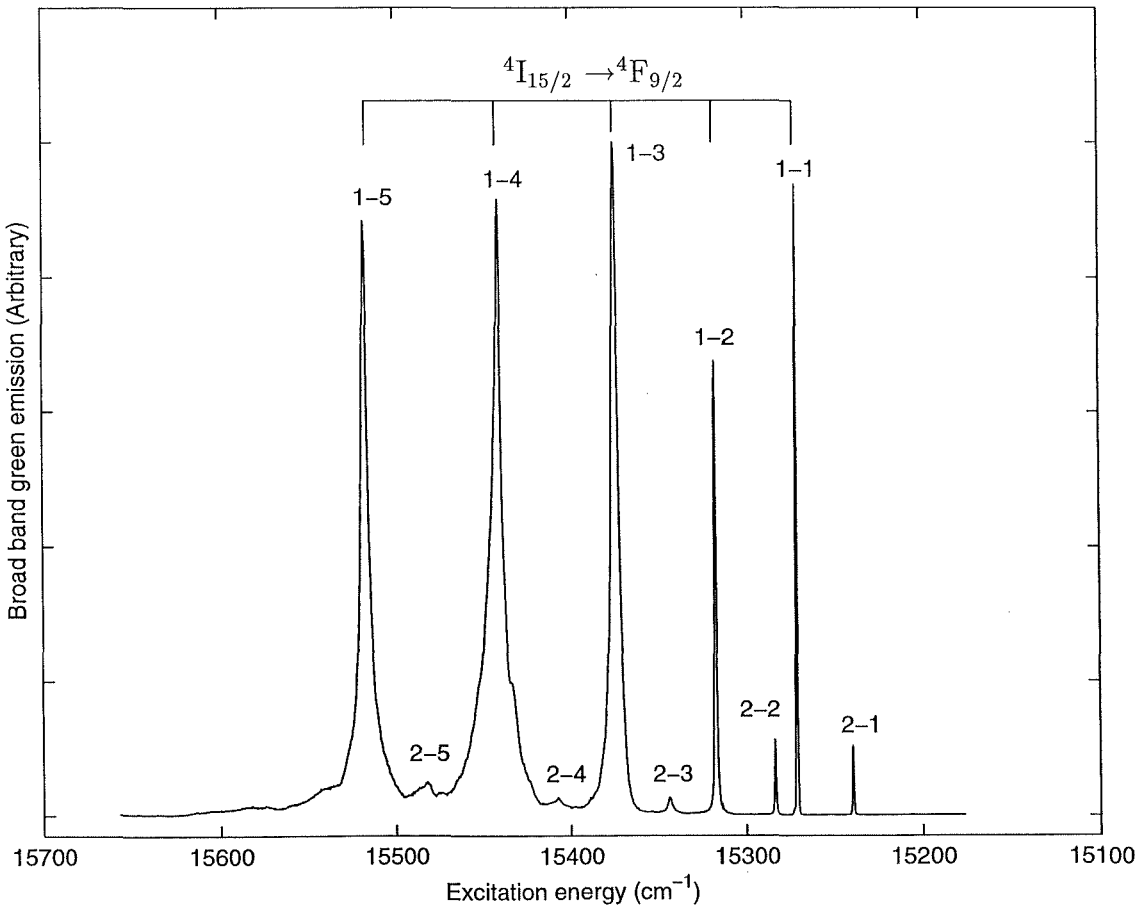

Figure 5.31: 12K Broad-band excitation spectra of $^4F_{9/2}$ monitoring $^4S_{3/2} \rightarrow ^4I_{13/2}$ upconverted emission. Transitions Z_m - D_n are labelled m-n for brevity.

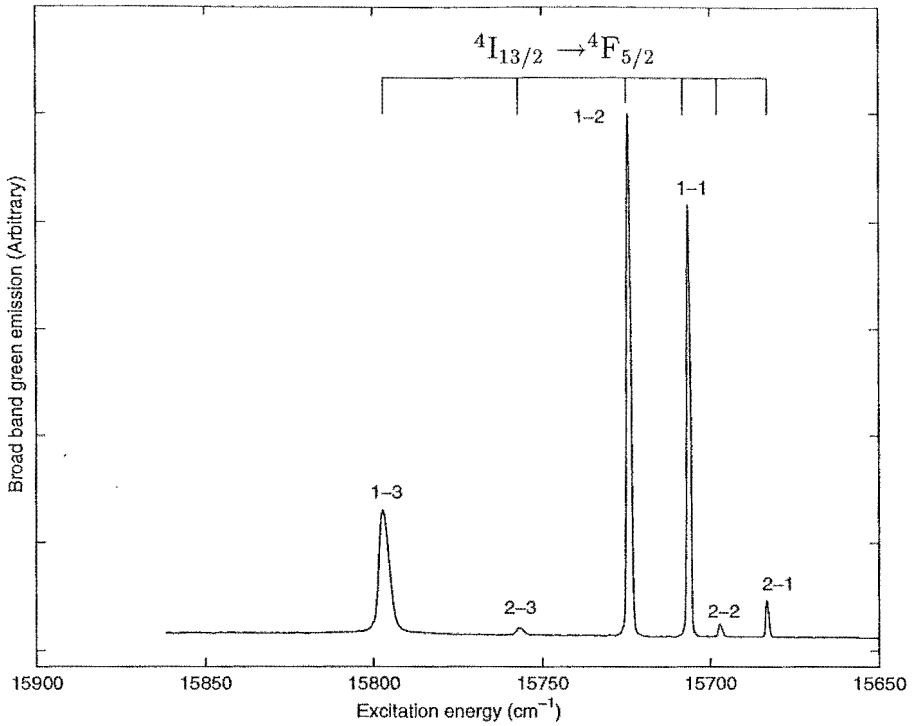

Figure 5.32: 12K Broad-band excitation spectra of $^4F_{9/2}$ monitoring $^4S_{3/2} \rightarrow ^4I_{13/2}$ emission. Transitions Y_m - H_n are labelled m-n for brevity.

The power dependence of the green $^4S_{3/2} \rightarrow ^4I_{15/2}$ emissions was recorded and the results are shown in Figure 5.33. The solid line represents the best fit to the data, which is linear with slope of exactly 2.0, indicating a quadratic relationship between input laser power and green emission. This power dependence confirms the proposed sequential-absorption mechanism.

Higher energy upconversion emission was recorded at very low intensities, even considering the small power range available (0-100mW). Emissions from the $^2H_{9/2}$ multiplet, and even the extremely weak $^2P_{3/2} \rightarrow ^4I_{13/2}$ emission, were able to be recorded. The fluorescence energies for these emissions were also identical to those for the previous two upconversion schemes. It is therefore suggested that similar processes are responsible.

Excitation energy (cm^{-1})	Transition assignment
15233	Z_2-D_1
15268	Z_1-D_1
15283	Z_2-D_2
15318	Z_1-D_2
15346	Z_2-D_3
15381	Z_1-D_3
15411	Z_2-D_4
15446	Z_1-D_4
15480	Z_2-D_5
15515	Z_1-D_5
15682	Y_2-H_1
15704	Y_2-H_2
15712	Y_1-H_1
15734	Y_1-H_2

Table 5.7: $^2P_{3/2} \rightarrow ^4I_{15/2}$ upconverted fluorescence. The transition assignments are given, based on absorption data. All energies are $\pm 1 cm^{-1}$

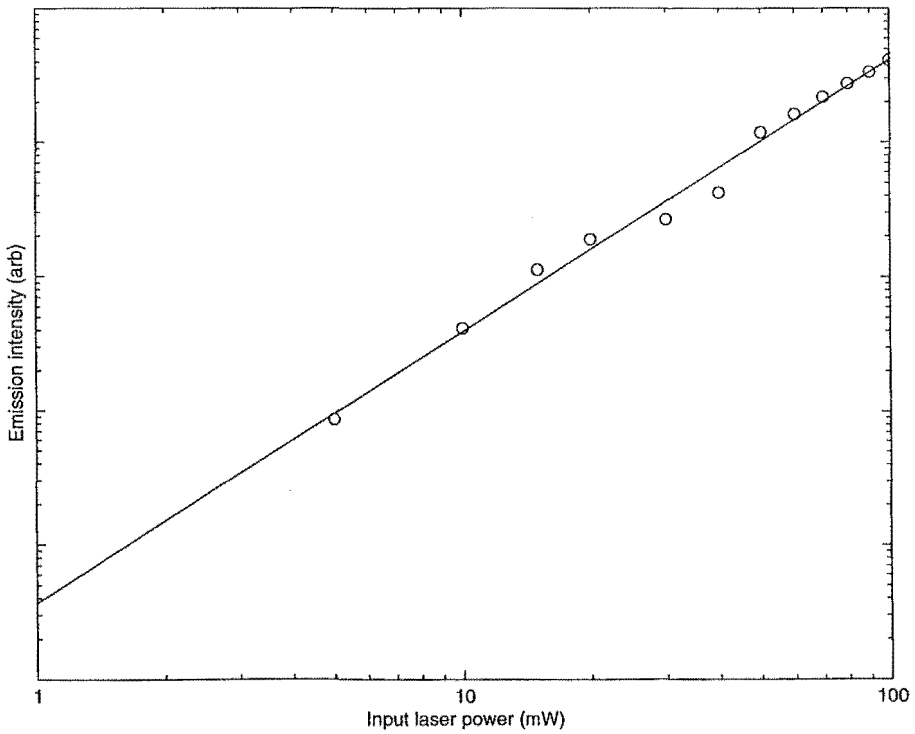

Figure 5.33: 12K Power dependence of $^4S_{3/2} \rightarrow ^4I_{15/2}$ upconversion emission from excitation into the $^4F_{9/2}$ multiplet. Solid line represents a best fit to the experimental data, and has a slope of 2.0.

5.7 Fluorescence bleaching in $K_2YF_5:Er^{3+}$

An interesting feature observed in this study was a bleaching of fluorescence emissions after initial laser excitation into the $^4I_{11/2}$ multiplet of Er^{3+} . These decays were often visible with the naked eye in the dominant green emissions and had charcteristic times of the order of 0.5s. The experiments below were performed with spectroscopic equipment described earlier. The photomultiplier tube signal from the Keithley electrometer was output to a purpose-built analog-to-digital converter. The response time of the A-D converter was found to be negligible compared to the decay times that were being measured. A manual shutter was used to gate the laser source.

Slow-decay emissions

Figures 5.34 and 5.35 show the fluorescence intensities from the $^4S_{3/2}$ and $^4I_{11/2}$ emissions, as a function of time immediately after the laser beam is opened onto the sample.

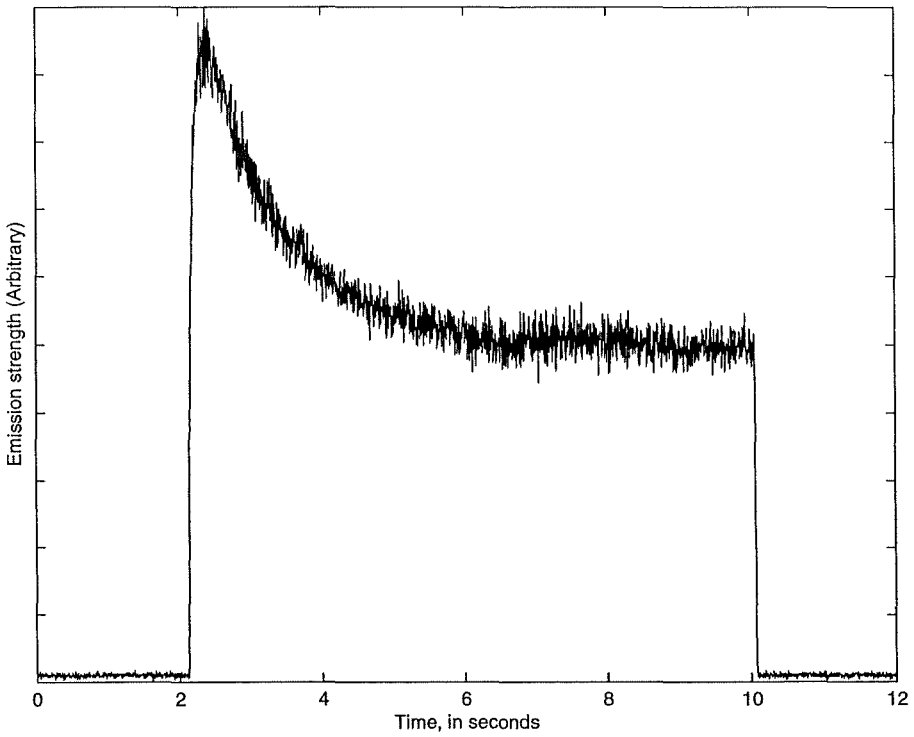

Figure 5.34: 12K Temporal profile of $^4S_{3/2} \rightarrow ^4I_{15/2}$ emissions, with excitation into the $^4I_{11/2}$ multiplet of $K_2YF_5:Er^{3+}$. The laser was tuned to the Z_1-A_1 GSA at 10233cm^{-1} , with input power 300mW.

The incident laser power for the above figures was 300mW, with the excitation frequency resonant with the Z_1-A_1 ground-state absorption at 10233cm^{-1} . The results were

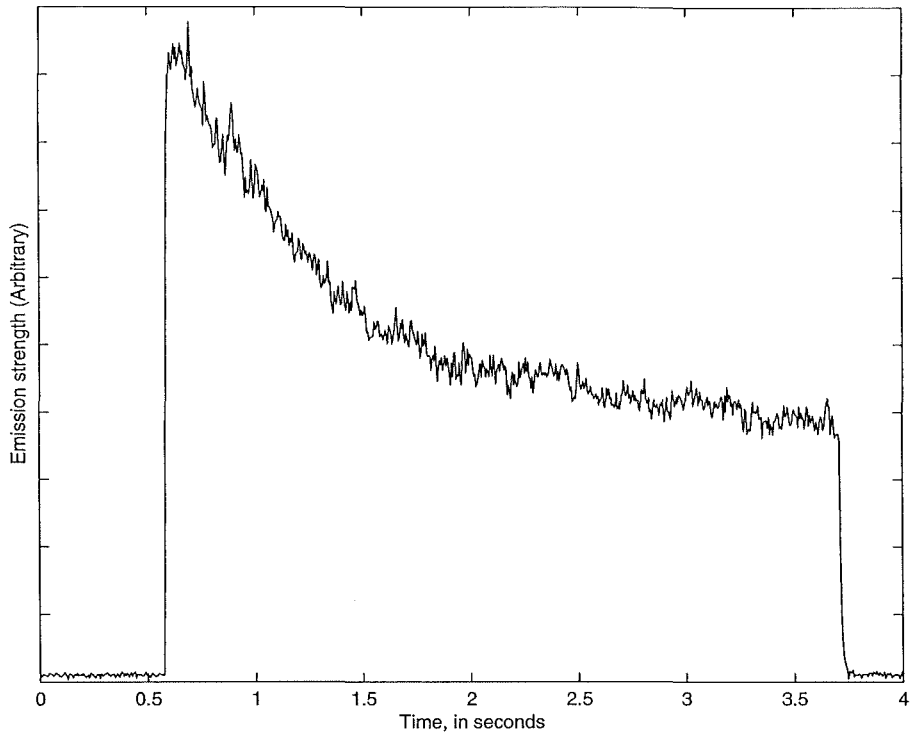

Figure 5.35: 12K Temporal profile of $^4I_{11/2} \rightarrow ^4I_{15/2}$ emissions, with excitation into the $^4I_{11/2}$ multiplet of $K_2YF_5:Er^{3+}$. The laser was tuned to the Z_1-A_1 GSA at 10233cm^{-1} , with input power 300mW.

fitted to an exponential decay by computer, and analysed in a similar way to the fluorescence lifetimes in Section 4.3. The decay constant of the $^4S_{3/2} \rightarrow ^4I_{15/2}$ emission profile was found to be 1.1s, whilst that of the $^4I_{11/2} \rightarrow ^4I_{15/2}$ emission was 640ms.

Although excitation into the $^4I_{15/2} \rightarrow ^4I_{11/2}$ ground-state absorption transitions produced this behaviour consistently, the characteristic times obtained differed between excitation energies.

Slightly different results could be obtained by tuning the laser onto certain excited state absorption transitions. Figures 5.36 and 5.37 highlight these differences, both sets of results were again taken at 300mW input power with excitation into the 10417cm^{-1} (Figure 5.36) and 10468cm^{-1} (Figure 5.37) excited-state absorption features. The first figure, for an excitation resonant with $A_1 \rightarrow G_3$, shows a noticeable rise time to the emissions, with no decay visible. Also evident from this figure, is the fact that a brief recovery time also exists for the system to revert to its original state after laser excitation ends. For short shuttered intervals, where the laser excitation is only briefly removed, no rise occurs.

By contrast, Figure 5.37 clearly shows a decay profile for an $A_1 \rightarrow G_4$ ESA transition.

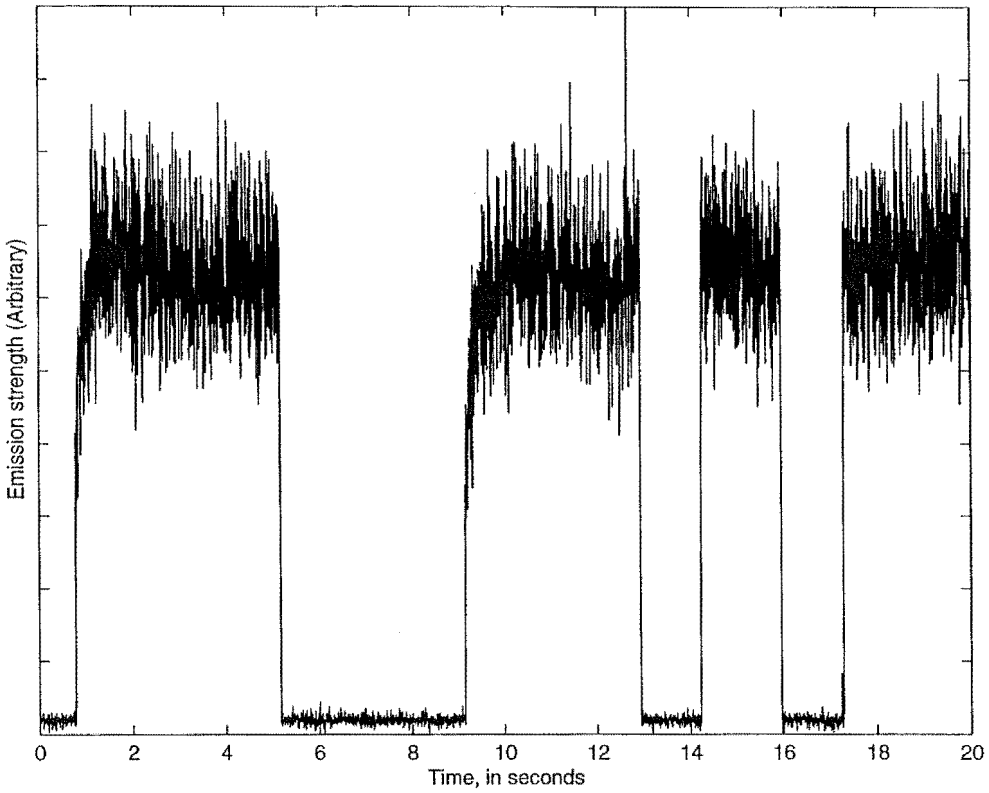

Figure 5.36: 12K Temporal profile of $^4S_{3/2} \rightarrow ^4I_{15/2}$ emissions, with excitation into the $^4I_{11/2}$ multiplet of $K_2YF_5:Er^{3+}$. The laser was tuned to the A_1-G_3 ESA at 10417cm^{-1} , with 300mW input power.

The rate of the decay has been found to increase gradually with increasing power, from 200-400mW. The behaviour is not observed at powers below 200mW. For the excitation of the ground-state absorption $Z_1 \rightarrow A_1$, the emission profiles for both $^4I_{11/2} \rightarrow ^4I_{15/2}$ and $^4S_{3/2} \rightarrow ^4I_{15/2}$ emissions were recorded at laser power increments between 30mW and 400mW. The decay times of each observed profile were recorded and are shown in Figure 5.38.

The results clearly show a relationship between input laser power, and the characteristic time for the fluorescence bleaching for both $^4S_{3/2}$ and $^4I_{11/2}$ emission. As the input power in increased, the characteristic time for both is seen to decrease.

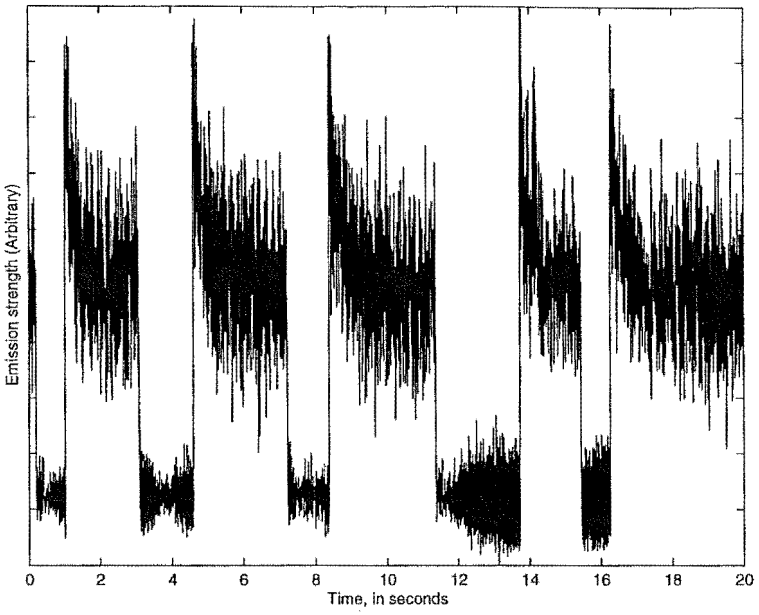

Figure 5.37: 12K Temporal profile of $^4I_{11/2} \rightarrow ^4I_{15/2}$ emissions, with excitation into the $^4I_{11/2}$ multiplet of $K_2YF_5:Er^{3+}$. The laser was tuned to the A_1-G_4 ESA at 10468cm^{-1} , with input power 300mW

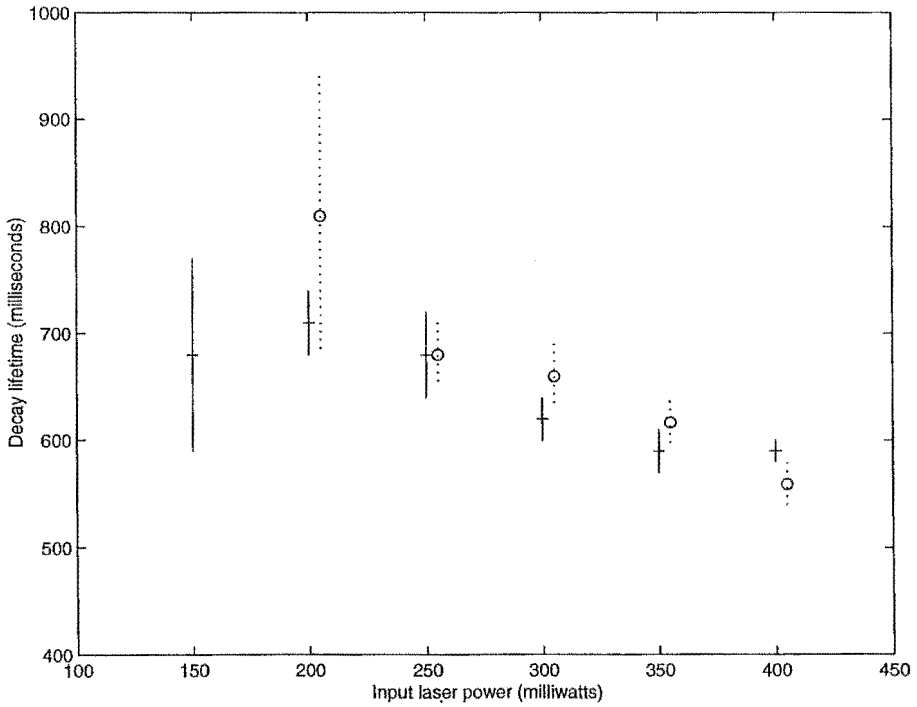

Figure 5.38: Dependence of decay lifetime on input laser power for excitation into the Z_1-A_1 ground-state absorption. The solid points are the lifetimes of decay profiles measured for $^4I_{11/2} \rightarrow ^4I_{15/2}$ emissions. The dotted points, which are offset for clarity, represent the measures lifetimes of $^4S_{3/2} \rightarrow ^4I_{15/2}$ emission profiles.

Depletion of ground-state population by laser excitation

An experiment was designed to examine the effect of laser excitation on the ground-state population of the $K_2YF_5:Er^{3+}$ system. The $^2H_{11/2}$ multiplet has been measured by optical absorption, and has several very strongly absorbing transitions. This multiplet does not fluoresce, decaying instead non-radiatively to the strongly emitting $^4S_{3/2}$ multiplet. An optical 'white-light' lamp was focused on the sample, and the transmitted light collected and dispersed by the SPEX 1701 spectrometer. The spectrometer was tuned to monitor the signal from the strongly absorbing $^2H_{11/2}$ transition. The sample was then also excited by the Ti:S laser source. The white light source was not considered to significantly alter the dynamics of the process, and no emissions exist from the $^2H_{11/2}$ multiplet to affect the absorption results. However, the absorption strength clearly depends on the ground-state population, and any change will give a good indication of that quantity.

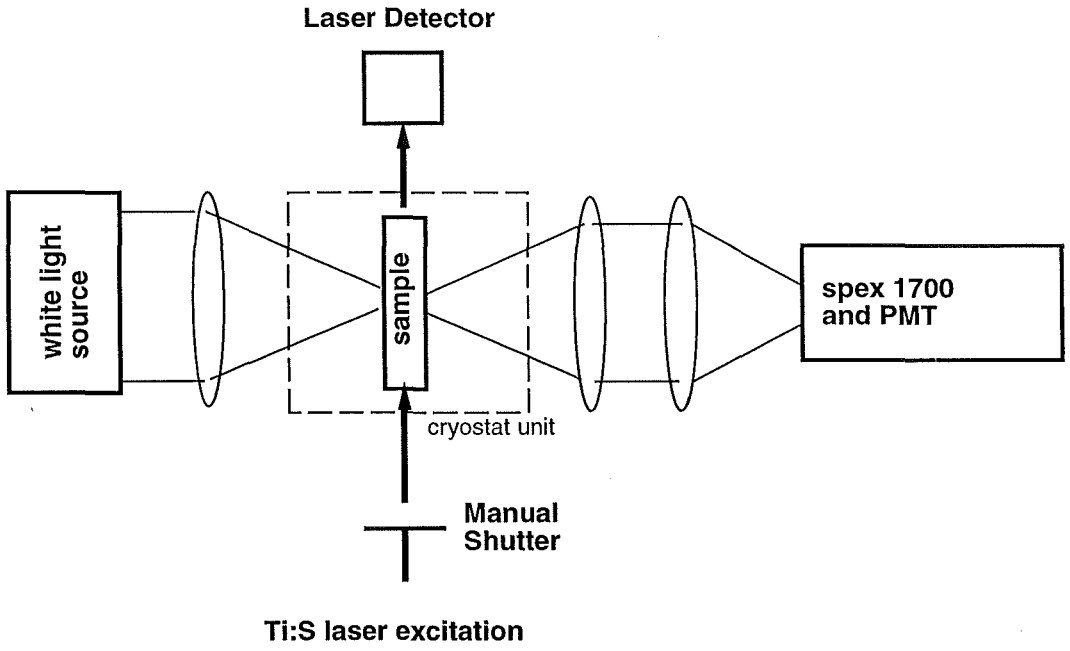

Figure 5.39: Experimental setup for laser depletion experiments

Also measured simultaneously was the intensity of the transmitted laser beam through the sample. This was achieved by mounting a silicon infrared diode in the path of the beam after the sample. In this way, an indication of the populations of the multiplets from which excitation can be achieved ($^4I_{15/2}$ and $^4I_{11/2}$) can be gained. Figure 5.39 shows the experimental setup.

Due to the focussing of the Ti:S laser beam to less than 0.3 mm^2 in cross-sectional area, the optical absorption measures the $^2H_{11/2}$ transmission from a sizable fraction of

the sample (which has cross-sectional area $\sim 1mm^2$) out of the laser beampath. thus any changes in the $^2H_{11/2}$ transmission can be assumed to correspond to significant changes in the ground-state population.

Initially the laser was tuned onto a ground-state excitation feature at $10233cm^{-1}$ (Z_1-A_1). The absorption attenuation, laser depletion and green upconversion emission profiles are shown in Figure 5.40. Note that the absorption profiles are displayed as transmission plots, where increasing absorption is represented by a decrease in the plotted value.

The results for ground-state excitation show the transmitted laser intensity increasing slowly and leveling offat a constant value. Simultaneously, the green upconversion starts at a high intensity and bleaches down to a constant level with the same time scale. The Z_1-F_4 transmission signal shows an increase, which corresponds to decreasing absorption at that wavelength. These results are consistent with there being a significant depletion of the ground-state population.

For a comparison, the same experiment was performed with the laser resonant with the excited-state absorption at $10417cm^{-1}$ (A_1 - G_3), the results are displayed in Figure 5.41. In this case there is no change to the transmitted laser beam intensity. However the Z_1-F_4 absorption exhibits the same decrease, indicating some depopulation of the ground-state energy level. The characteristic rise and decay lifetimes shown in Figures 5.40 and 5.41 were fit to exponential functions and are given in Table 5.8.

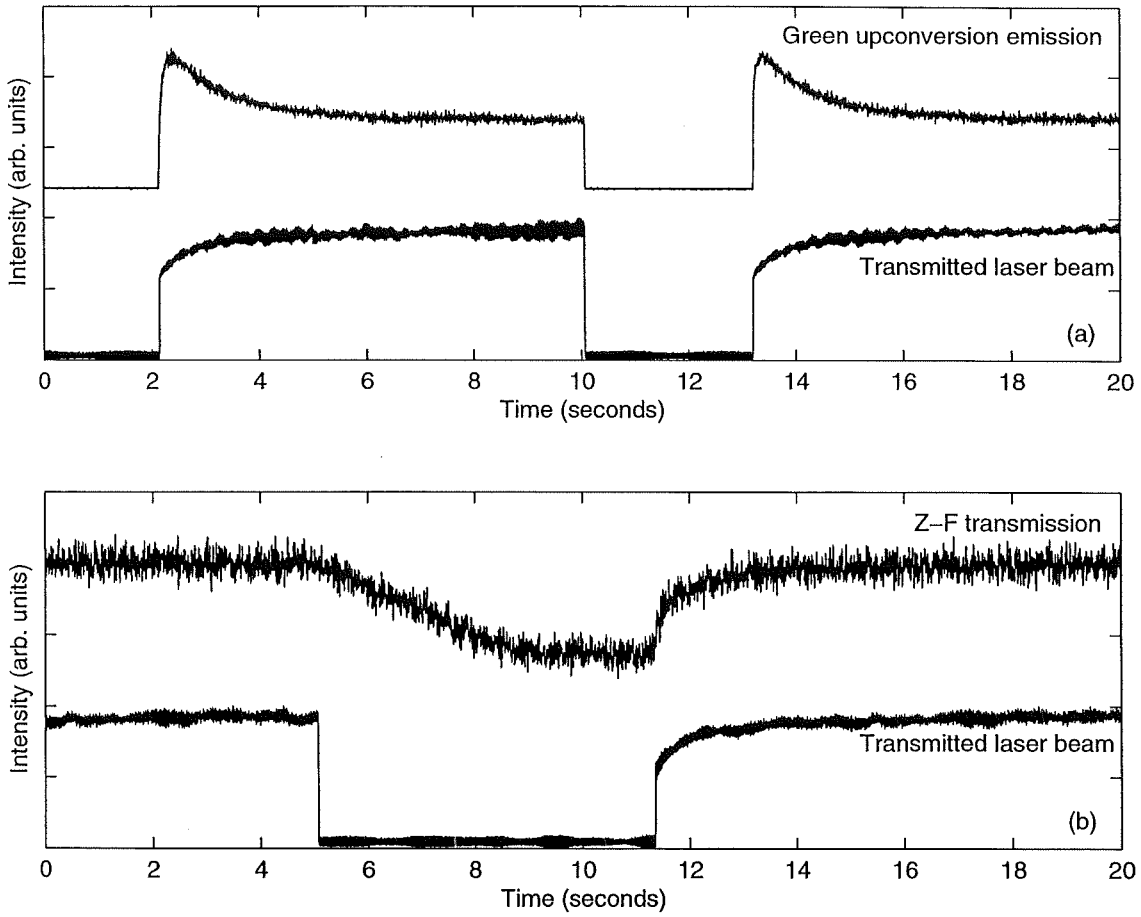

Figure 5.40: Results of depletion experiments for 300mW laser resonant with ground-state absorption Z_1 - A_1 at 10233cm^{-1} and a sample temperature of 12K. (a) Measurement of the green $^4S_{3/2} \rightarrow ^4I_{15/2}$ emissions (top) and the consequent depletion of the laser beam (bottom). (b) Depletion of ground-state population as measured through Z_1 - F_4 transmission profile (top) and simultaneous laser beam depletion (bottom).

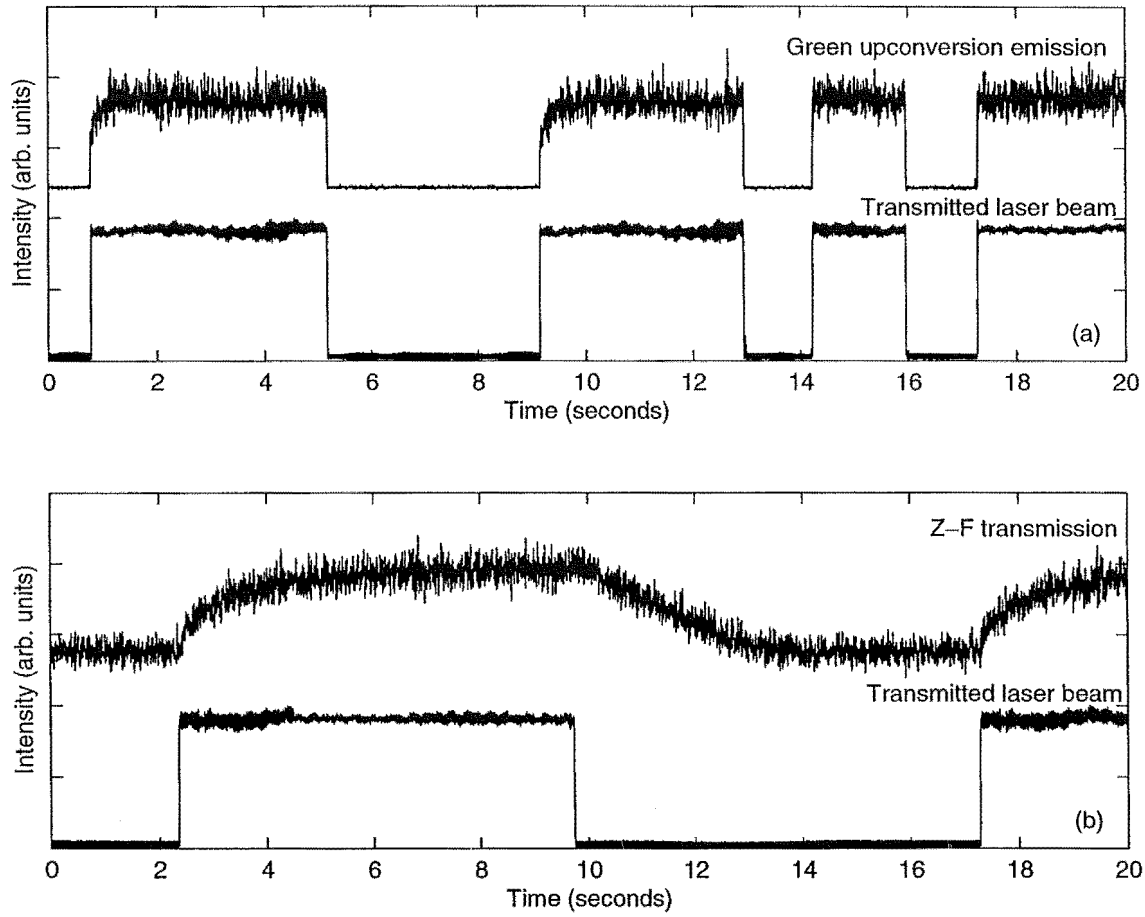

Figure 5.41: Results of depletion experiments for 300mW laser resonant with excited-state absorption A_1- G_3 at 10417cm^{-1} and a sample temperature of 12K. (a) Measurement of the green $^4S_{3/2} \rightarrow ^4I_{15/2}$ emissions (top) and the consequent depletion of the laser beam (bottom). (b) Depletion of ground-state population as measured through Z_1 - F_4 transmission profile (top) and simultaneous laser beam depletion (bottom).

Discussion

Excitation	Quantity		Measured lifetimes (s)
Pumping GSA Z_1-A_1 at $10233cm^{-1}$ (from Fig. 5.40)			
	Green emission decay	τ_{em}	1.1
	Transmitted beam rise	τ_{beam}	1.2
	Ground-state depletion	τ_{gr}	0.6
	Ground-state recovery	τ'_{gr}	3
Pumping ESA A_1-G_3 at $10417cm^{-1}$ (from Fig. 5.41)			
	Green emission rise	τ'_{em}	0.1
	Ground-state depletion	τ_{gr}	1.1
	Ground-state recovery	τ'_{gr}	3

Table 5.8: Measured rise and decay times for beam and ground-state depletion experiment. Rise and decay times are ±0.1s.

Clearly in both cases presented above (Z_1-A_1 GSA and A_1-G_3 ESA excitations) there is evidence that the ground-state is significantly depopulated by the laser excitation. The slower rate τ_{gr} in the case of ESA is most likely due to the fact that the initial $^4I_{15/2}$ $\rightarrow{}^4I_{11/2}$ in that case is non-resonant, with an energy 'mismatch' of $\sim 20cm^{-1}$. The pump rate for the laser excitation from the $^4I_{15/2}$ ground state to $^4I_{11/2}$ will be considerably reduced in that case.

In the last few years several authors have reported similar long characteristic times for upconversion emissions from various rare-earth doped hosts. These effects have been attributed to the photon-avalanche effect, as modelled by Joubert *et al* [18]. These avalanche-pumped systems utilise cross-relaxation from the upconverted ions, to provide a non-linear increase in the population of the first-excited level. Numerical solutions of the non-analytical rate-equation systems that can be used to describe this process have well reproduced experimental data [19],[20],[21].

The results obtained earlier for an ESA excitation A_1-G_3 are similar in some respects to those obtained in those studies. If the $K_2YF_5:Er^{3+}$ forms centres that allow energy transfer between ions at the low concentrations used in this study, then several cross-relaxation pathways become possible. One strong possibility is the decay $^4S_{3/2}$ + $^4I_{15/2}$ $\rightarrow{}^4I_{11/2}$ + $^4I_{11/2}$, where the two transitions are very nearly in resonance. Also possible are such relaxations as $^2H_{11/2}$ + $^4I_{15/2}$ $\rightarrow{}^4I_{13/2}$ + $^4I_{9/2}$, which would, given a suitably

long $^4I_{13/2}$ fluorescence lifetime, not replenish the $^4I_{15/2}$ ground-state whilst exciting an ion into $^4I_{11/2}$.

A combination of cross-relaxation effects such as those described above could be used to model the behaviour displayed in $K_2YF_5:Er^{3+}$. For excitations resonant with a ground-state absorption, the initial laser excitation removes ions from the ground state to the $^4I_{11/2}$ multiplet (see Figure 5.40), but not from the beam excitation as they are now subject to an ESA transition. As the upconverted populations increase though, cross-relaxation processes become stronger, removing ions from both the ground-state *and* the first-excited state. Thus the green upconversion emissions will gradually decay.

The success of such a model would require some further work, both to gauge the extent of energy transfer processes in the material $K_2YF_5:Er^{3+}$, and to measure some quantities related to the rate-equations of the systems, such as branching ratios and remaining intrinsic multiplet lifetimes. The former could be accomplished by a program of mixed-doping in new samples. Energy transfer between mixed-doped systems is often easier to describe and interpret. Some indication could also be obtained, if ions of a similar size are used, as to the various rare-earth centres that are formed in the growth stage.

Chapter 6

Conclusion

Visible upconversion fluorescence has been observed for laser excitation into the $^4I_{11/2}$, $^4I_{9/2}$ and $^4F_{9/2}$ multiplets of K_2YF_5:(0.6% Er^{3+}). The predominant emission was from the $^4S_{3/2}$ multiplet of Er^{3+}. The mechanisms responsible for this emission for each excitation have been shown by power dependence and laser excitation spectra to be two-step Sequential Absorption Upconversion (SAU) processes.

In the case of $^4I_{11/2}$ excitation, the SAU process consisted of a ground-state absorption $^4I_{15/2} \rightarrow ^4I_{11/2}$, followed by an excited state absorption $^4I_{11/2} \rightarrow ^4F_{7/2}$. In this case the two absorptions are very nearly doubly-resonant. For near-infrared $^4I_{9/2}$ excitation, the dominant mechanism involves an initial ground-state absorption $^4I_{15/2} \rightarrow ^4I_{9/2}$, followed by decay to the $^4I_{13/2}$ multiplet. The long-lived $^4I_{13/2}$ multiplet acts as a metastable state to allow the excited-state absorption transition, $^4I_{13/2} \rightarrow ^2H_{11/2}$. Further, the $^4I_{9/2}$ multiplet is also long-lived, and can provide for an ESA into the $^2H_{9/2}$ multiplet.

The upconversion emission for $^4F_{9/2}$ excitation was the result of a further SAU process. The ground-state absorption transition was in this case $^4I_{15/2} \rightarrow ^4F_{9/2}$, with the $^4I_{13/2}$ multiplet again acting as a metastable state for the excited-state absorption $^4I_{13/2} \rightarrow ^4F_{5/2}$.

Significant blue and ultra-violet upconverted emission was also observed from the $^2H_{9/2}$, $^4G_{11/2}$ and $^2P_{3/2}$ multiplets for each excitation scheme. This fluorescence was several orders of magnitude weaker than the $^4S_{3/2}$ emissions. The promotion of an ion into the $^2P_{3/2}$ multiplet from excitation into the $^4I_{11/2}$ and $^4I_{9/2}$ multiplets is a process of at least third order. Narrow-band excitation spectra showed no evidence of further excited-state absorptions. It is thus suggested that this fluorescence is the result of energy-transfer upconversion through either direct ion-ion transfer, or energy migration through the host lattice.

Interesting dynamical effects resulting from excitation into the $^4I_{11/2}$ multiplet have also been observed. These include very slow (τ ~0.6s) attenuating fluorescence, and an increase in the laser beam transmittance. These emissions are consistent with a sizable decrease in the ground-state population. The features and power dependence of this

effect resemble those of photon avalanche upconversion processes described by several authors. It is believed that similar cross-relaxation processes are responsible for the observed results.

A pulsed dye-laser system was used to measure the lifetimes of the $^4S_{3/2}$, $^4F_{9/2}$ and $^4I_{9/2}$ multiplets. All were found to be an order of magnitude larger than those reported by Peale *et al*, confirming those workers suggestion of concentration quenching of the multiplet lifetimes. The $^4I_{9/2}$ and $^4F_{9/2}$ multiplets were observed to be relatively long-lived, and therefore suitable for acting as metastable states for the above upconversion processes.

Optical absorption spectroscopy was performed in the visible region 10000cm^{-1} - 30000cm^{-1} on K_2YF_5:Er^{3+} . Absorption features were unambiguously assigned for transitions to the $^4I_{11/2}$, $^4I_{9/2}$, $^4F_{9/2}$, $^4S_{3/2}$, $^2H_{11/2}$, $^4F_{7/2}$, $^4F_{5/2}$, $^4F_{3/2}$, $^2H_{9/2}$, $^4G_{11/2}$, and $^2K_{15/2}$ multiplets of the Er^{3+} ion. The assignments for the $^4I_{11/2}$ to $^4F_{7/2}$ multiplets are in agreement with the previous work of Peale *et al.* Weak absorption lines that are assigned to the $^2G_{7/2}$ multiplet were also recorded.

Laser Selective Excitation techniques have revealed evidence of a second symmetry centre. This energies of this centre have been shown to differ only slightly from the primary centre. It is believed that this centre represents only a slight perturbation of the environment surrounding the Er^{3+} ion, perhaps due to formation of a pair centre or clustering. The excitation features of this weak centre were not visible in the upconversion studies.

A trigonal C_{3V} symmetry Hamiltonian was fitted to the experimental crystal-field energy levels from the optical absorption work. The standard deviation of the fitted energy-level scheme (with respect to those experimentally observed) improved significantly on previous work, even though more experimental levels were included.

6.1 Suggestions for further work

One of the unresolved issues in this thesis, is the extent of energy-transfer processes in this material. Several of the suggested upconversion mechanisms for the higher energy blue and ultraviolet emissions utilised energy-transfer, although none could demonstrate this conclusively. A study of the concentration dependence of the upconversion emissions might provide a more definite result on this issue.

For the study of such processes as cross-relaxation, mixed-doping studies are often

useful. In these experiments, energy-transfer can be demonstrated by the excitation of one ion, and subsequent emission from another. This would also provide better information on the positioning of the Er^{3+} dopants in the K_2YF_5 chain, and whether clusters such as dimers are preferentially formed in sample growth.

Given the promising crystal-field fit obtained, the approximation of a C_{3V} Er^{3+} centre could provide more extensive information. Preliminary results have shown the emissions of this system to be polarised with respect to both emission and excitation. However, the orientation of the samples used were unknown and no further information could be obtained. Suitable single crystal samples with known crystallographic axes should be grown. The study of such samples can yield valuable information on the irreducible representations that represent each of the crystal-field energy levels. These irreps could then be used to assign the crystal-field energy-levels to specific wavefunctions, which should drastically improve the quality of the crystal-field fit.

References

[1] H M Crosswhite W T Carnall, Hannah Crosswhite. Energy level structure and transition probabilities of the trivalent lanthanides in LaF_3 . Technical report, Argonne National Laboratory, Chemistry Division, 1977.

[2] Y A Gorbunov Y A Kharitanov and B A Maksimov. Crystal structure of potassium yttrofluoride K_2YF_5 . *Sov. Phys. Crystallogr.*, 28(5):610–1, Sept.-Oct. 1983.

[3] F G Anderson R E Peale, H Weidner and N M Khaidukov. Spectroscopy of Er^{3+} in K_2YF_5 . In Clifford R Pollock and Walter R Bosenberg, editors, *OSA TOPS*, volume 10. Optical Society of America, 1997.

[4] M Fournier J Cousseins R Mahiou, J Metin and B Jacquier. Luminescence and energy transfer in a one-dimensional compund: K_2GdF_5 . *J. Lumin.*, 43:51–58, 1989.

[5] D R Lide, editor. *Handbook of Chemistry and Physics.* CRC Press, Boston, 71 edition, 1991.

[6] T Mahiou P Boutinard and J C Coussiens. Effect of one-dimensional structure on Tb^{3+} $^5D_3$-$^5D_4$ cross-relaxation in K_2YF_5 . *J. Lumin.*, 72-74:318–320, 1997.

[7] EÁ Kuz'min R I Bochkova, Y N Saf'yanov and N V Belov. Interpretation of the crystal structure of K_2SmF_5 by the peak rhomb method. *Sov. Phys. Dokl.*, 18(9):575–576, March 1974.

[8] B G Wybourne. *Spectroscopic properties of Rare Earths.* Interscience Publishers, 1965.

[9] Nicholas M Strickland. *Laser excitation and infra-red absorption spectroscopy of rare-earth ion centres in fluorite crystals.* PhD thesis, University of Canterbury, 1996.

[10] R G Wheeler G F Koster, J O Dimmock and H Statz. *Properties of the thirty-two point groups.* M.I.T. Press, Cambridge, Mass, USA, 1963.

[11] D R Tallant and J C Wright. Selective laser excitation of charge compensated sites in CaF_2:Er^{3+} . *J. Chem. Phys.*, 63(5):2074–2085, September 1975.

[12] A A Clifford. *Multivariate error analysis.* Wiley, N.Y., 1973.

[13] Mike Reid. f-shell empirical programs.

[14] Jon-Paul Renee Wells. *Laser Spectroscopy of Alkaline Earth Fluoride Crystals doped with trivalent Samarium and Europium ions.* PhD thesis, University of Canterbury, 1996.

[15] C W Nielson and G F Koster. *Spectroscopic Coefficients for the p^n, d^n and f^n Configurations.* MIT press, USA, 1963.

[16] R Bivens M Rotenberg N Metropolis and J K Wooten Jr. *the 3-j and 6-j symbols.* The technolology press, MIT, 1959.

[17] J C Wright. Up-conversion and excited state energy transfer in rare-earth doped materials. In F K Fong, editor, *Topics in applied physics*, volume 15. Berlin-Springer-Verlag.

[18] M F Joubert S Guy and B Jacquier. Model of the photon-avalanche effect. *Phys. Rev. B*, 48(14):10031–10037, October 1993.

[19] Y Chen F Auzel and D Meichenin. Room temperature photon avalanche up-conversion in Er-doped ZBLAN glass. *J. Lumin.*, 61:692–694, 1994.

[20] M F Joubert S Guy, D P Shepherd and B Jacquier. Blue avalanche upconversion in Tm:ZBLAN fiber. *J. Opt. Soc. Am. B*, 14(4):926–934, April 1997.

[21] M F Joubert S Guy and B Jacquier. Blue upconverted fluorescence via photon-avalanche pumping in YAG:Tm. *Phys. Stat. Sol. (b)*, 183:K33–K36, March 1994.